SPIN-TORQUE-DRIVEN MICROWAVE FREQUENCY DYNAMICS IN MAGNETIC NANOPILLAR DEVICES

A Dissertation

Presented to the Faculty of the Graduate School

of Cornell University

in Partial Fulfillment of the Requirements for the Degree of

Doctor of Philosophy

by

Kiran Vijay Thadani

August 2009

© 2009 Kiran Vijay Thadani
ALL RIGHTS RESERVED

SPIN-TORQUE-DRIVEN MICROWAVE FREQUENCY DYNAMICS IN MAGNETIC NANOPILLAR DEVICES

Kiran Vijay Thadani, Ph.D.

Cornell University 2009

In a magnetic multilayer, spin-transfer torque from a spin-polarized current can excite magnetic layers into steady-state precessional oscillations. In this dissertation, the main theme of our work has been the study of microwave signals produced by spin-torque-driven magnetization dynamics excited by direct or radio-frequency currents in magnetic multilayer spin-valve devices with a nanopillar geometry.

In the first part of our work, we have studied the frequency linewidths of the precessional oscillations excited by direct currents in the magnetic layers as a function of the in-plane magnetic field angle and temperature. The motivation of this work was to understand the important mechanisms contributing to the linewidths with a view to optimizing the coherence of the oscillations. We have found strong variations in the frequency linewidth of the signals, with a decrease by more than a factor of 20 as the field is rotated away from the magnetic easy axis to the in-plane hard axis. Based on micromagnetic simulations, we have identified these variations as due to a transition from spatially incoherent to coherent precession.

As a function of temperature, our experimental linewidths can be explained by a combination of amplitude and phase fluctuations and thermally-activated hopping between different dynamical modes. At lower temperatures, the linewidths are affected more strongly by amplitude and phase fluctuations. At

higher temperatures, the linewidths increase more rapidly due to thermally-activated hopping between different dynamical modes.

In the second part of our work, we have studied spin-torque effects on the exchange-bias of antiferromagnet / ferromagnet bilayers by studying the amplitude of the spin-torque-driven resonant motion of an exchange-biased magnetic layer in response to a radio-frequency current. The motivation of this work was to investigate spin-torque effects in antiferromagnets. We have fabricated magnetic nanopillar devices in which the free magnetic layer is exchange-biased to an antiferromagnet, and which allow a direct measurement of the magnitude of the exchange bias and its current dependence. Using spin-torque-driven ferromagnetic resonance (ST-FMR) measurements, we have observed strong variations in the precession frequency as a function of the current, indicating that the exchange-bias is current-dependent. We have also verified that the effective damping of an exchange-biased nanomagnet is higher than for an unpinned nanomagnet.

BIOGRAPHICAL SKETCH

Kiran Vijay Thadani is the daughter of Renuka (nee Chablani) and Vijay Thadani, and the elder sister of Leher and Nihar. She was born in Bombay, India on September 21, 1981. Kiran is proud to belong to an Indian Sindhi family. Her ancestors used to live in Hyderabad Sindh, until the Partition of India in 1947 forced them to relocate to Bombay and other parts of India. Her most vivid childhood memories are listening to her grandparents' harrowing stories of survival during the Partition of 1947 and the riots that ensued, which displaced them from their homes and tore the family apart. Her grandparents' stories of sacrifice and hardship left a lasting imprint on her as she was growing up.

Kiran grew up in Bombay and New Delhi, and studied in Delhi Public School (DPS) until she finished high school. Kiran was among the top-ranked students in academics throughout her school years, and she was awarded a Gold Medal for academic excellence near the conclusion of high school. Besides academics, Kiran was also passionate about learning languages and playing sports. In 1997, she was awarded a prestigious Sanskrit scholarship by the Government of India after a competitive public exam. She learnt martial arts for almost 4 years and won Gold and Bronze medals in Karate at many zonal-level tournaments. She also competed in many tennis tournaments. In ninth grade, she dislocated her shoulder while flinging a shot-put ball and thereafter, decided to retire her Wimbledon dreams for good.

In 1999, Kiran was accepted into the undergraduate engineering program at the University of Pennsylvania and she moved to the United States. She credits her freshman physics professor, Prof. Charlie Johnson, for helping her realize her love for physics and mathematics and for encouraging her to pursue scien-

tific research. Kiran's most enjoyable months as an undergraduate were spent in Prof. Johnson's lab working on nanotube electronics. She also had a very rewarding internship at the IBM-Almaden Research Center working with Dr. Stuart Parkin on magnetic tunnel junctions, which eventually led her to realize that she wanted to study magnets full-time in graduate school as well. Kiran graduated from Penn in 2003, *Summa Cum Laude*, with two degrees: Bachelor of Science in Engineering (B.S.E) in Systems Engineering and Bachelor of Arts (B.A.) with Distinction in Physics. While at Penn, she was a University Scholar and she was on the Dean's List for both degrees all four years of college. In her senior year, she was awarded the Williams E. Stephens Memorial Prize in Physics and the Victor W. Ku Memorial Award in Systems Engineering.

Kiran came to Cornell University for graduate school in 2003. She just barely survived her first Ithaca winter and came very close to quitting graduate school at the end of her first semester. Fortunately, Prof. Dan Ralph gave her a once-in-a-lifetime opportunity to join his research group and she has not looked back ever since. She joined the Ralph group in the summer of 2004 and spent her first weekend in the Ralph group at The Home Depot, scanning the hardware aisles and taking voracious notes on all possible types of screw-drivers, pliers and small electronics appliances in order to hastily learn all the hardware jargon that is crucial for any experimentalist's career. She obtained an M.S. in Physics from Cornell in 2007 and will receive her Ph.D. in Physics in August 2009. After her Ph.D., Kiran will be moving to the sunny west coast to work in Silicon Valley.

"Sri Vakratunda Mahakaaya

Koti Surya Samaprabha

Nirvighnam Kuru Me Deva

Sarvakaryeshu Sarvada"

***

In loving memory of

my great-grandmother - "Ami" Devi M. Advani,

Nani & Nana - Pritwanti & Tharumal Chablani,

Dadi & Dada - Jasoti & Hiranand Thadani

***

For Mama and Papa,

who taught me never to say "I cannot"

ACKNOWLEDGEMENTS

My path to the Ph.D. has been anything but that of ballistic transport. The path was fraught with research challenges, frustrating days and personal crises that caused a lot of momentum-scattering and occassionally, enough back-scattering to make me almost quit at certain points. In retrospect, I am glad I did not quit. I read a beautiful quote once, "your willingness to know the unknown is faith." I would like to acknowledge here the people who imparted positive momentum to my journey and are responsible for helping me reach the end of this degree.

First and foremost, I would like to express my gratitude to my advisor and teacher, Prof. Dan Ralph. I couldn't have asked for a more brilliant, patient and kind advisor than Dan to teach me the ropes of the scientific research process. Dan gave me the independence to chart my own graduate career, as well as the space to learn everything we deemed necessary for my overall education (including the terrifying machine shop course that needed to be rapidly followed up by some meditation and tennis classes). Dan taught me that every mistake is a learning opportunity, and I am grateful to him for his patience and encouragement as I made my way slowly up the learning curve in the lab. I admire Dan for treating every student in his research group as an individual and allowing every student a chance to bring their own personality (and sleep schedule) to the research problem, thereby allowing everyone to work creatively without feeling stifled or judged. Thank you, Dan, for giving me the privilege to work in your research lab, a place where I learnt to appreciate two important words: data and paranoia.

I would like to thank Prof. Bob Buhrman for his questions and insights about subtle aspects of my data that I hadn't thought about, thereby forcing me to think deeper about my scientific arguments. I have often felt uplifted by the

thought that if my data and arguments could stand the tests of Profs. Dan Ralph and Bob Buhrman, I could take on any power, experimental or theoretical, in the world.

I am also grateful to Prof. Bruce van Dover and Prof. Tomas Arias for serving on my committee. Everything I know about magnetics, I learnt from Prof. van Dover's "MSE 545: Magnetic Materials" course. It was one of the best and most relevant courses I took in graduate school. Prof. van Dover's enthusiasm for magnetism always made me feel that this was the best field (pun not intended) that any scientist or engineer could ever possibly work in. Prof. Tomas Arias posed an insightful A-exam question to me about finite-element simulations that gave me much-needed confidence to run computational simulations later on in my Ph.D.

The Ralph group has been my local family and comedy club in Ithaca. Jack Sankey was my big brother in the lab when I joined the group and looked out for me in the early days. Jack taught me how to solder, chase noise and optimize the human lifetime by running fast Perl scripts. He also put up with my myriad questions about spin-transfer and life, not to mention my cranky hair-pulling outbursts on the seemingly different definitions of the demagnetizing field in different papers and the dichotomy between mks and cgs units.

Ilya Krivorotov is the epitome of brilliance and kindness, and he is one of my biggest role-models. Ilya's amazing intuition and lucid explanations were instrumental in my initial analysis and interpretations of the linewidth results.

Zhipan Li, Yongtao Cui and Chen Wang are responsible for turning my Ph.D. around for the better when they joined the group. Zhipan gave me encouragement and moral support during one of my lowest points in graduate school, and I credit him for helping me structure a story to write my first paper. Zhipan

also proved to me that television soap operas can be effective stress-busters. I have enjoyed all forms of discussions with Yongtao and Chen, ranging from ST-FMR to Citibank's rewards program (because of which, I was able to get at least 2 free round-trip tickets to California). I also thank them for their time to willingly help me debug some stubborn electronics and simulation problems.

Sufei Shi has been one of my closest and funniest friends in the lab, who has often cheered me up with his furcoats and memorable dinners at Chinese restaurants. I admire Sufei's dedication to nanoparticles, his favorite line "Kiran, I am so close to getting data" that I had to hear for one full year, as well as his penchant for the stock market and questionably-acquired electronic gadgets and software.

Joshua Parks has been the loudest cheerleader in all my complaints about machine shop and Ithaca, and has sportingly maintained our self-established tradition of calling each other every time there is a differential change in the weather. Suffice to say, Josh and I have called each other a lot.

Ferdinand Kuemmeth and Kirill Bolotin were two of my favorite people in the Ralph group. Their impeccable yet contrasting experimental styles, along with their good-natured bickering and arguments about missing vacuum pumps and multimeters provided for a lot of entertainment.

Thanks to Lin Xue for his entertaining speeches on hopes and dreams and Obama. If someone gives me honorary Chinese citizenship, I will be sure to vote for you when you run for political office some day. Thanks also to Wan Li for being one of the sweetest members of the Ralph group, and also for accompanying me at many fun dinners in Sangam and workout sessions at the gym.

I was fortunate to work with two talented and hard-working undergraduate students: Lin Kittiwatanakul and Kristin Jekielek. We had a lot of fun designing and building a new electromagnet to do MFM imaging of our nanopillars.

I would also like to thank the following members of the Ralph group for their contributions, both intellectual and fun, to my Ph.D.: Saikat Ghosh, Takahiro Moriyama, Eugenia Tam, Colin Heikes, Ted Gudmundsen, Jacob Grose, Marie Rinkoski, Alex Champagne, and Janice Guikema.

I was very lucky to collaborate with the Buhrman group, where I met some of the smartest and nicest people in the spin-torque world. Ozhan Ozatay patiently taught me the entire nanopillar fabrication process, and I am indebted to him for his excellent instruction. Our debate about the validity of certain "Indian" dishes is still ongoing. Praveen Gowtham has been a great friend and has often lent a compassionate ear to my ramblings over many coffee-breaks and dinners. Nathan Emley sportingly endorsed my efforts to find a universal solution to happiness, which we promptly abandoned after realizing it was impossible. Patrick Braganca and John Read offered kind words of advice and encouragement to keep me from becoming entirely cynical, and they also hosted some memorable barbeque parties (with veggie burger options) at their lakeside house. I would also like to acknowledge the following members of the Buhrman group for their experimental help and friendly chats: Oukjae Lee, Luqiao Liu, Vlad Pribiag, Eric Ryan, Greg Fuchs, Andrei Garcia, Hsin-Wei Tseng and Yun Li.

Giovanni Finocchio from the University of Messina (Italy) deserves special thanks for doing the micromagnetic simulations for my linewidth paper. Bob McMichael and Mike Donahue at NIST also helped me debug some OOMMF code when I was trying to implement micromagnetics simulations in the lab.

I would like to thank Dr. Vasil Tiberkevich and Prof. Andrei Slavin at Oakland University for many useful discussions about their non-linear oscillator model.

I collaborated on a magnetic semiconductors project with Prof. Nitin Samarth's group at Pennsylvania State University. I enjoyed working with Partha Mitra on these devices and learnt a lot about these systems during the course of the project.

I would also like to thank the following staff members in Clark Hall for helping me with my experiments: Dr. Jonathan Shu, for ensuring all probe stations and electronics were in order in D-10, where I did the majority of my experiments; John Sinnott, for helping with the ribbon-bonder; Dr. Eric Smith, for help with low-temperature cryostats and vacuum systems; Mick Thomas, for training and help on the Clark SEM; Ronald Kemp and Stan Carpenter, for their input on designing and building some pieces in lab. Bob "Sned" Snedeker deserves special mention for teaching me how to use the tools in machine shop. I credit Sned's lessons, as terrifying as they were, for helping me face my fears of big machines, take risks and be a better experimentalist overall.

Thanks are also in order for the administrative staff in physics and CNS, especially Deb Hatfield, Lisa Margosian (who has since left), Cathy Wetterer, Judy Wilson and Cheryl Lewkowicz, who made sure all paper-work flowed smoothly and efficiently. These wonderful ladies always had a smile on their face, something that I have learnt to appreciate and not take for granted.

I also want to thank the staff members at CNF for their training and trouble-shooting help inside the clean room. In particular, I want to thank Alan Bleier and John Treichler for help with e-beam lithography; Jerry Drumheller, for help with the Veeco Ion Mill and the sputtering system; Meredith Metzler, for help

with etching; Karlis Musa, for help with CAD and computing. Working at CNF was one of the highlights of my graduate career. To me, the best part about working in the clean room was coming in contact with people from different disciplines, all using the same tools for different ends. During pump-down wait times, I made many good friends, to whom I turned to for consulting or trouble-shooting help and also commiserated with about broken equipment. Thanks to Abhishek Ramkumar, Sasikanth Manipatruni, Jahan Dawlaty, Faisal Ahmad, Nelson Felix, Jing Sha, Sara Barron, Shahyaan Desai, Hassan Raza, Quentin Diduck and Hengky Chandrahalim, for their part in making the clean room a sociable place.

The basement of Clark Hall was my home for five years and I encountered some of the most brilliant minds in science in these corridors. Friends like Andre Mkhoyan, Andrew Fefferman, Ethan Bernard, Vladimir Khmlenko, Tchefor Ndukum, Jared Hertzberg, Benjamin Cipriany, Amar Bhagwat, Sourish Basu, Judy Cha, Alex Kwan, Lena Fitting, Vikram Gadagkar, Michael Durst, Ethan Pratt, Valerie Anderson, Elaine Farkas and Joern Kupferschmidt, made the basement experience bearable and fun. I especially thank the guys in H-corridor for their strong shoulders that helped lift my cryostats and heavy equipment when I was doing low-temperature experiments.

I would like to acknowledge my Cornell friends outside of the lab who provided great social company to help me overcome the Ithaca blues and made me realize I was not alone during some dark days in graduate school: Sara Maccagnano-Zacher, Ruxandra Bondarescu, Baran Han, Christine Tan, Sharvari Nadkarni, Jui Bhagwat, Amit Bhojwani, Ajay Sadarangani, Sunitha Bandla, Asma Hatoum, Anuja de Silva, Sudhamsu Jawahar, Amy Richter, Sandeep Kishore, Krishnaprasad Vikram, Sattu Ayyalasomayajula, Liesl Folks, and Anita

Govindjee. I would like to say a special thank you to Shailey Motial and Madhukar Varshney for getting me through a tough crisis last year and for their hospitality on many evenings of Bollywood movies, delicious exotic dinners and cups of tea. My good friends, Mitali Singh and Aman Kohli, kept me amused all the time with their "handy" household items and their sarcasm about Ithacan winters. Vrinda Aunty is one of my biggest mentors at Cornell, and I enjoyed our intellectual discussions and outpourings about life over veggies-and-pesto-pita lunches at Alladin's.

In the summer of 2007, I had to undergo a painful shoulder surgery that took me an unusually long time to recover from. I am grateful to my surgeon, Dr. Matt Scuderi at SUNY-Upstate Medical Hospital and my physio-therapists, Susan Geisler and Karen Brigham at Cornell, for their excellent care and rehabilitation assistance. I am most indebted to Mrs. Motial for her alternative medicine treatment that worked wonders on my shoulder.

I want to say thank you to my best friend, Srikant, for laughter during the happiest months of my life and for prayers during the most painful ones. Thank you for sharing with me your greatest gift - faith.

I would like to thank my friends from school and college, who have stood by me, regardless of distance and time. In particular, I want to thank Kinnari Chandriani, Devjani Saha, Paayal Desai, Sarah Chu, Sohini Raychaudhuri, Deepa Venkatachalam, Udai Pawar, Venkat Srinivasan, Gayathri Subramanian, Arpita Chatterjee, Debraj Ghosh, Lavanya Sharan, Vidya Ramachandran, Geetika Srivastava, Kriti Mittal, Priyanka Reddy, Punita Anand, Priyanka Gandhi, Ritesh Kapur, and Neeraj Trehon.

I bow to the elder members of my family for their continued blessings: Paisa Nani, Gursoran Uncle, Dattu and Mohna Advani, Rani Gidwani, Sheela Ad-

vani, Bua, Vinod and Ruby Chablani, Vineeta Kuzma, Ravina Malkani, Vimla and Hema Chablani.

Finally, I want to acknowledge my family. Mama and Papa, to whom this thesis is dedicated, have been my rock and they steadfastly believed in me throughout this journey even when I was hesitant. Being the daughter of two perfectionist workaholics, I learnt as a child that the first step in solving a problem is to make a list and second, to remember that hard-work never killed anybody. My mother stayed up with me on the phone countless nights and heard me ramble about my days, just as she has from the time I was in kindergarten. My father patiently put up with my "I don't know" replies for 6 years, every time he asked me how my PhD was going and when I expected to finish. My little sisters, Leher and Nihar, have proved to me that the same genes can often lead to dramatically different personalities. They have always succeeded in lightening up my mood with some goofy story or song or better yet, their latest ambitions to solve the world's problems. I am proud to be your daughter and sister.

TABLE OF CONTENTS

Biographical Sketch . . . iii
Dedication . . . v
Acknowledgements . . . vi
Table of Contents . . . xiv
List of Figures . . . xvii

1 Introduction **1**
1.1 Background and Review of Spin-Torque . . . 1
1.1.1 Giant Magneto-Resistance (GMR) . . . 1
1.1.2 Spin-Transfer Effect . . . 2
1.1.3 Technological Applications of Spin-Transfer . . . 7
1.2 Overview of this Dissertation . . . 12
REFERENCES . . . 14

REFERENCES **14**

2 Methods: Nano-Fabrication, Measurements & Modeling **16**
2.1 Nano-Fabrication . . . 16
2.2 Measurements . . . 30
2.2.1 dV/dI Measurement . . . 30
2.2.2 High Frequency DC-Spectra Measurements . . . 32
2.2.3 Spin-Torque-Driven Ferromagnetic Resonance (ST-FMR) Measurements . . . 42
2.2.4 Projected Field Probe Station . . . 49
2.2.5 3-D Vector Magnet . . . 50
2.3 Modeling: Numerical Simulations . . . 58
2.3.1 Macrospin Simulations . . . 58
2.3.2 Micromagnetic Simulations . . . 61
REFERENCES . . . 67

REFERENCES **67**

3 Linewidths of Spin-Torque-Driven Oscillations as a Function of In-Plane Magnetic Field Angle & Temperature **69**
3.1 Previous Studies of Spin-Torque Oscillator Linewidths . . . 69
3.1.1 Putting Our Work in Perspective . . . 69
3.2 What do Linewidths Mean? . . . 70
3.3 Important Mechanisms and Mathematical Models for Linewidths 71
3.3.1 Amplitude and Phase Fluctuations in a Non-Linear Auto-Oscillator . . . 71
3.3.2 Thermally-Activated Hopping between Dynamical Modes 81
3.4 Linewidths as a Function of In-Plane Magnetic Field Angle . . . 82
3.4.1 Devices: Structure & Fabrication . . . 82

3.4.2 DC-Characterization . . . 83
3.4.3 High-Frequency DC-Driven Spectra . . . 86
3.4.4 Analysis as a Function of Magnetic Field Angle . . . 89
3.4.5 Analysis as a Function of Current: Qualitative Correlation between Linewidth and df/dI . . . 94
3.4.6 Spin-Torque-Driven Ferromagnetic Resonance Measurements (ST-FMR) . . . 97
3.4.7 Macrospin Simulations . . . 101
3.4.8 Micromagnetic Simulations . . . 107
3.5 Linewidths as a Function of Temperature . . . 111
3.5.1 DC-Characterization . . . 112
3.5.2 Analysis as a Function of Temperature . . . 112
3.5.3 Modeling of Linewidths . . . 113
3.5.4 Macrospin Simulations as a Function of Temperature . . . 120
3.5.5 Conclusions for Temperature Dependence of Linewidths . 122
3.6 Comparing Our Minimum Linewidths to Previous Spin Torque Oscillator Studies . . . 122
3.7 Conclusions . . . 123
REFERENCES . . . 125

REFERENCES 125

4 Spin-Torque Effects on the Exchange-Bias of Antiferromagnet/Ferromagnet Bilayers 130
4.1 Review of Antiferromagnets & Exchange-Bias . . . 130
4.2 Spin-Torque Effects in Antiferromagnets . . . 131
4.2.1 Theoretical Predictions of Spin-Torque Effects in Antiferromagnets . . . 132
4.2.2 Previous Experiments of Spin-Torque Effects in Antiferromagnets . . . 134
4.2.3 Putting Our Experiments in Perspective . . . 137
4.3 Design & Structure of Devices . . . 138
4.4 Fabrication of Devices . . . 141
4.5 DC-Characterization . . . 141
4.6 ST-FMR Measurements . . . 145
4.7 Analysis as a Function of Magnetic Field Angle . . . 146
4.8 Analysis as a Function of I_{DC} . . . 148
4.9 Effective Damping . . . 152
4.10 Dependence on I_{RF} . . . 153
4.11 Variations among different samples . . . 154
4.12 Comparison to Previous Studies of Spin-Torque Effects on Exchange-Bias . . . 157
4.13 Conclusions . . . 159
REFERENCES . . . 160

REFERENCES **160**

5 Conclusions **163**
REFERENCES 166

REFERENCES **166**

LIST OF FIGURES

1.1 Cartoon of the spin-torque effect. 4
1.2 Vector diagram of all the torques acting on the free layer. 5
1.3 Different regimes of spin-transfer. 7
1.4 MRAM cross-point architecture and ST-MRAM architecture. . . . 8

2.1 Sputtered multilayer stack for nanopillar fabrication. 17
2.2 Scanning Electron Microscope (SEM) images of an elliptical device and a circular device after electron-beam lithography. 19
2.3 Optical image and profilometry scan after isolating devices (Photolithography-1 + Ion Mill-1). 21
2.4 Alignment marks defined during e-beam and photolithography. 22
2.5 Optical image and profilometry scan after defining bottom leads (Photolithography-2 + Ion Mill-2). 23
2.6 Test-array of devices to be analyzed by AFM after planarization (Ion Mill-3). 24
2.7 AFM height measurements of the test-array of devices before and after planarization (Ion Mill-3). 25
2.8 AFM surface-plot measurements of the test-array of devices before and after planarization (Ion Mill-3). 26
2.9 Profilometry scans of the oxide height after (Photolithography-3 + BOE etch) and (Photolithography-4 + 100-200 nm of oxide evaporation above top leads). 28
2.10 Profilometry scans of the oxide height after (Photolithography-4 + 100-200 nm of oxide evaporation above top leads) and (Photolithography-5 + Ion Mill-4). 29
2.11 Optical images of the completed devices, electrodes and leads after Photolithography-6 + Ion Mill-5 and Ion Mill-6. 30
2.12 Schematic of home-made current-source to bias the devices. . . . 31
2.13 Schematic of circuit and heterodyne mixing technique to measure DC-driven microwave frequency dynamics. 33
2.14 Examples of DC-driven microwave-frequency spectra, calibrated power spectral density and Lorentzian fit. 35
2.15 Calibration for frequency-dependent Johnson noise: sources of reflections and losses in the line. 37
2.16 Cartoon of the misalignment angle between the layers, θ_{mis} and the precession angle of the free layer, θ_{max}, as well a s an intuitive picture of the first and second harmonic peaks in the spectra. . . 41
2.17 Schematic of Spin-Torque-Driven Ferromagnetic Resonance (ST-FMR) measurement circuit. 44
2.18 Flatness procedure for ST-FMR measurements. 45
2.19 Peak-shapes of the ST-FMR signal. 48
2.20 Photograph of the projected-field probe station 50

2.21 Photograph of the 3-axis vector magnet cryostat. 51
2.22 Photograph of the dipstick and sample-carrier for the 3-axis vector magnet cryostat. 56
2.23 Schematic of all the torques in the Landau-Lifshitz-Gilbert equation for magnetization dynamics. 59

3.1 Illustration of Amplitude Fluctuations. 72
3.2 Illustration of Phase Fluctuations. 74
3.3 Temperature dependence of the linewidth of a non-linear auto-oscillator. 80
3.4 Power spectra for magnetization telegraphing between static and meta-stable or dynamical states. 82
3.5 Layer structure of the two types of nanopillar spin-valve devices that we studied with an exchange-biased fixed layer and a thick fixed layer. 84
3.6 Differential resistance as a function of current and magnetic field for the exchange-biased-fixed-layer device and the thick-fixed-layer device 85
3.7 Stoner-Wohlfarth macrospin calculations of the orientation of the fixed and free magnetic layers and the relative angle between them as a function of the in-plane magnetic field angle, θ_H. 87
3.8 Power spectral density and linewidths as a function of the magnetic field angle for the exchange-biased-fixed layer device and the thick-fixed-layer device. 88
3.9 Analysis of the spin-torque-driven microwave signals as a function of θ_H for the sample with the exchange-biased fixed layer as a function of current and field angle at room temperature and H = 1000 Oe. 91
3.10 Analysis of the spin-torque-driven microwave signals as a function of θ_H for the sample with the thick fixed layer at room temperature and H = 800 Oe. 93
3.11 Examples of the differences in symmetry about $\theta_H = 90^\circ$ between the two kinds of devices. 94
3.12 Analysis of the spin-torque-driven microwave signals as a function of current for the sample with the exchange-biased fixed layer at room temperature and H = 1000 Oe. 95
3.13 Analysis of the spin-torque-driven microwave signals as a function of current for the sample with the thick fixed layer at room temperature and H = 800 Oe. 97
3.14 Comparison of DC-driven spectra and ST-FMR spectra for the exchange-biased-fixed-layer device at H = 1000 Oe 99
3.15 ST-FMR spectra at different I_{DC} at $\theta_H = 90^\circ$ and H = 1000 Oe for the exchange-biased-fixed-layer device. 100

3.16 Simulated free-layer magnetization response and trajectory at $I = 0$ mA and $H = 800$ Oe, applied along $\theta_H = 10°$. 103
3.17 Simulated free-layer magnetization response and trajectory at $I/I_C = 1$ and $H = 800$ Oe, applied along $\theta_H = 10°$. 104
3.18 Simulated free-layer magnetization response and trajectory at $I/I_C = 2.3$, $I/I_C = 2.7$ and $I/I_C = 3$ at $H = 800$ Oe, applied along $\theta_H = 10°$. 105
3.19 Simulated power spectral density and linewidth variations as a function of θ_H at $I/I_C = 1$ and $H = 800$ Oe. 106
3.20 Calculations of the non-linear frequency shift and linewidth as a function of the in-plane field angle, using the analytical expression of the generation linewidth for a non-linear oscillator. 107
3.21 Micromagnetic simulations of the exchange-biased sample. . . . 109
3.22 Differential resistance as a function of H and I at room temperature for a nanopillar spin valve device with an exchange-biased fixed layer that was cooled down for temperature-dependence measurements. 113
3.23 Analysis of the spin-torque-driven microwave signals as a function of temperature for an exchange-biased fixed layer sample at $H = 1150$ Oe and $\theta_H = 90°$. 114
3.24 Modeling the temperature dependence of the linewidths. 116
3.25 Analyzing the temperature dependence of the linewidths in the (a) lower temperature range (< 160 K) and (b) higher temperature range. 117
3.26 Example of power spectral density indicating hopping between different dynamical modes at $T = 185$ K. 118
3.27 Calculation of effective temperature due to Joule heating 119
3.28 Simulated power spectral density and linewidths as a function of temperature for $\theta_H = 10°$ and $\theta_H = 80°$. 121

4.1 Cartoon of uncompensated and compensated antiferromagnet / ferromagnet interfaces. 131
4.2 Theoretical predictions of the spin-transfer torque in antiferromagnets. 134
4.3 Summary of previous experiments to probe spin-torque effects in antiferromagnets. 136
4.4 Layer structure of the pinned-free-layer nanopillar spin-valve devices that we studied. 139
4.5 SQUID data of the magnetic moment as a function of the applied magnetic field for an unpinned Py layer (6 nm thick) and a pinned Py layer (6 nm) exchange-biased by different thicknesses of antiferromagnet, IrMn (3 nm, 6 nm and 9 nm). 140
4.6 Optical and AFM images of the semi-extended fixed layer. 142

4.7 Differential resistance as a function of magnetic field and magnetic field angle for the pinned-free-layer (FM/AFM) device. . . 144
4.8 Typical ST-FMR spectrum for the FM/AFM pinned-free-layer-device. 146
4.9 Analysis of the ST-FMR spectra for the FM/AFM pinned-free-layer device as a function of θ_H, to identify the pinned-free-layer mode. 147
4.10 Analysis of the ST-FMR spectra for the FM/AFM pinned-free-layer device as a function of I_{DC}, the I_{DC}-dependence of the precession frequency and the corresponding I_{DC}-dependence of the H_{EB}. 150
4.11 Amplitude of the ST-FMR spectral peaks as a function of I_{DC} at (a) small H and (b) large H. 152
4.12 Effective damping of the FM/AFM pinned-free-layer device as a function of I_{DC}. 153
4.13 Analysis of the ST-FMR amplitude and frequency as a function of I_{RF}. 154
4.14 Differential resistance and ST-FMR data for a thinner antiferromagnet (6 nm) device. 156
4.15 Comparison of the current-dependence of the H_{EB} for FeMn/CoFe bilayers and IrMn/CoFe bilayers. 158

CHAPTER 1

INTRODUCTION

1.1 Background and Review of Spin-Torque

The drive towards miniaturization and sophistication of consumer electronic devices has been progressing at a relentless pace. Silicon-based microelectronic devices have played an integral role in steering this revolution during the latter part of the last century. Gordon Moore's prediction [1] in 1965 of doubled computing capacity in every new silicon chip manufactured within two years of the previous one is testimony to the ascendancy of silicon in the microelectronics race. Most conventional electronic devices have exploited the *charge* of electrons in the conduction mechanism but there has also been a significant research effort over the last several years to exploit the intrinsic *spin* of electrons - a field that has come to be known as *spintronics*.

1.1.1 Giant Magneto-Resistance (GMR)

Magnetic materials have an intrinsic magnetization, which makes them superb candidates for nonvolatile memory. Today, almost every modern storage device, from a hard disk drive to an IPod uses magnetic materials in some form for writing, recording and reading data. The research effort in magnetic materials was recognized by the 2007 Nobel Prize awarded to Peter Grunberg and Albert Fert for the discovery of the Giant Magneto-Resistance (GMR) effect [2].

Magnetic materials like iron, unlike normal metals like copper, have an un-

equal density of spin-up and spin-down states at the Fermi level, thereby allowing one spin-channel to be the majority carrier and the other spin-channel to be the minority carrier. This allows magnetic materials to act as spin-polarizers. If a current is passed through two magnetic layers placed next to each other, the incoming unpolarized electrons go through the first magnetic layer and come out polarized in the direction of the magnetization of that layer. When the polarized electrons encounter the second magnetic layer, they encounter a low-resistance if the magnetization of the second layer is parallel to that of the first magnetic layer and a high-resistance if the magnetization of the two layers is anti-parallel. In other words, the resistance through a stack of magnetic layers depends on the *relative* density of states of the majority spin-carriers at the Fermi level in the magnetic layers. This is the basis of the GMR effect. If the magnetic layers are parallel, we measure a low resistance and if they are anti-parallel, we measure a high-resistance. The difference between the low-resistance and high-resistance states can be a few tens of percent for spin-valves (magnetic layers separated by a copper spacer) or several hundreds of percent for magnetic tunnel junctions (magnetic layers separated by an insulating barrier such as MgO or Al_2O_3). Grunberg and Fert were awarded the Nobel Prize for the discovery of GMR in Fe/Cr/Fe trilayers [3] and (Fe/Cr) multilayers [4], respectively.

1.1.2 Spin-Transfer Effect

An analogue of the GMR effect is the spin-transfer effect, which was theoretically predicted by Slonczewski and Berger [5, 6]. We mentioned above that in GMR, an electrical current passing through a magnetic layer becomes spin-polarized. If, however, the electrical current is large enough and the volume

of the magnetic layers is small enough, the electrical current can become spin polarized upon passing through one magnetic layer and can then transfer some of that spin into the second next magnetic layer. As a result, the magnetization of the second layer can either switch parallel or anti-parallel relative to the first magnetic layer [7] or it can be excited into steady-state oscillation of frequencies in the microwave range [8]. A nice review of the spin-transfer torque was published by Ralph and Stiles in [9].

In Figure 1.1, we show a cartoon of how the spin-transfer effect works. There are two magnetic layers separated by a spacer. One of the magnetic layers is made much thicker than the other layer, so that it will be harder to switch. We call this magnetic layer the ”fixed” layer. The second magnetic layer, which is thinner, is called the ”free” layer. Assume that the magnetic layers start out initially with a small relative misalignment angle. If current is passed such that electrons flow from the fixed layer to the free layer (Figure 1.1(a)), they will pass through the fixed layer first and come out polarized in the direction of the fixed layer. When they encounter the free layer, in order to conserve angular momentum, they will transfer the transverse component of their momentum to the free-layer, exerting a torque on it that will push it to align parallel with the fixed layer.

On the other hand, if current is passed such that electrons flow from the free layer to the fixed layer (Figure 1.1(b)), they will pass through the free layer first and come out polarized in the direction of the free layer. When they encounter the fixed layer, however, they exert a torque on the fixed layer but it is not sufficient to move the fixed layer because of its large volume. Consequently, the reflected electrons from the fixed layer go back to the free-layer and now exert a

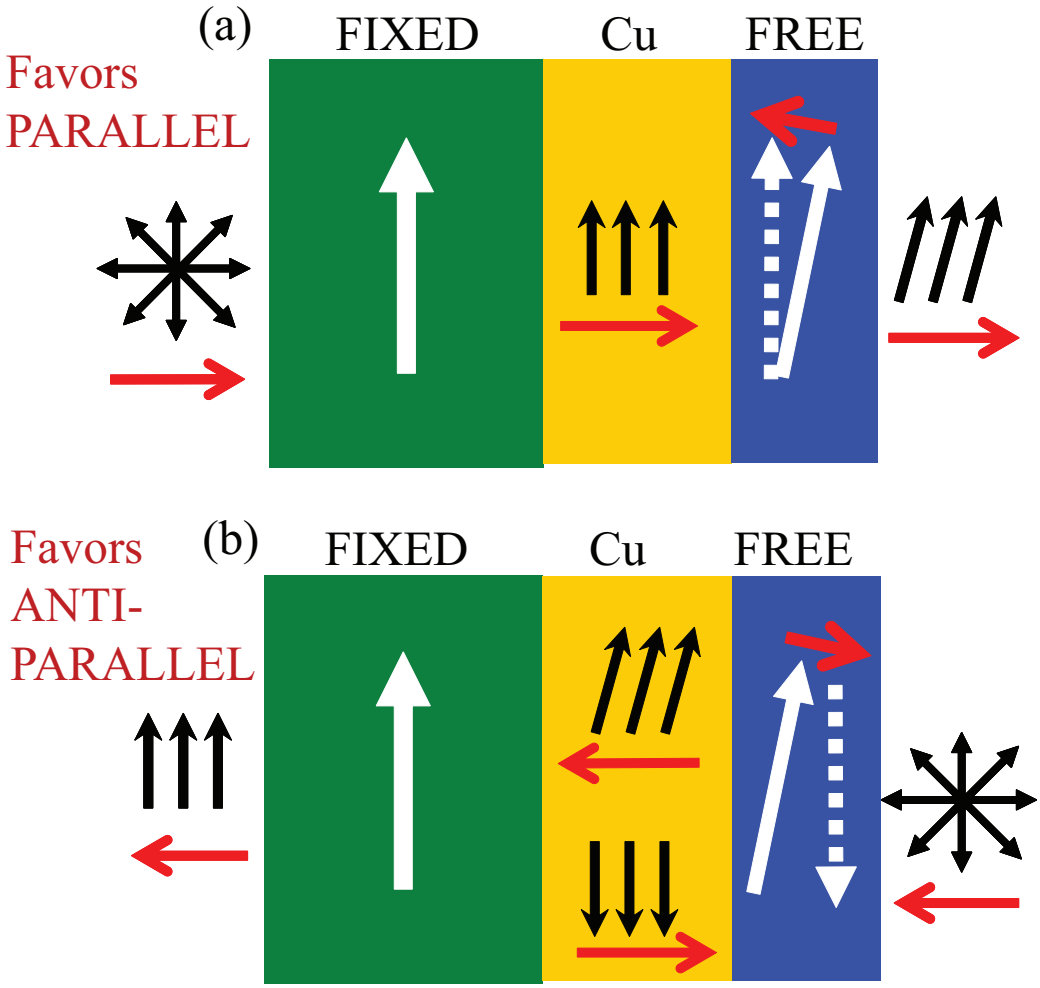


Figure 1.1: Cartoon of the spin-torque effect. (a) Electron flow from the fixed layer to the free layer leads to parallel alignment between the magnetic layers and low-resistance. (b) Electron flow from the free layer to the fixed layer leads to anti-parallel alignment between the magnetic layers and high-resistance.

torque on the free-layer that pushes the free-layer to align anti-parallel with the fixed layer.

So depending on the direction of the current, the spin-transfer can exert a torque on the free layer that can cause it to align either parallel or anti-parallel with respect to the fixed layer, leading to a low-resistance state or a high-resistance state, respectively.

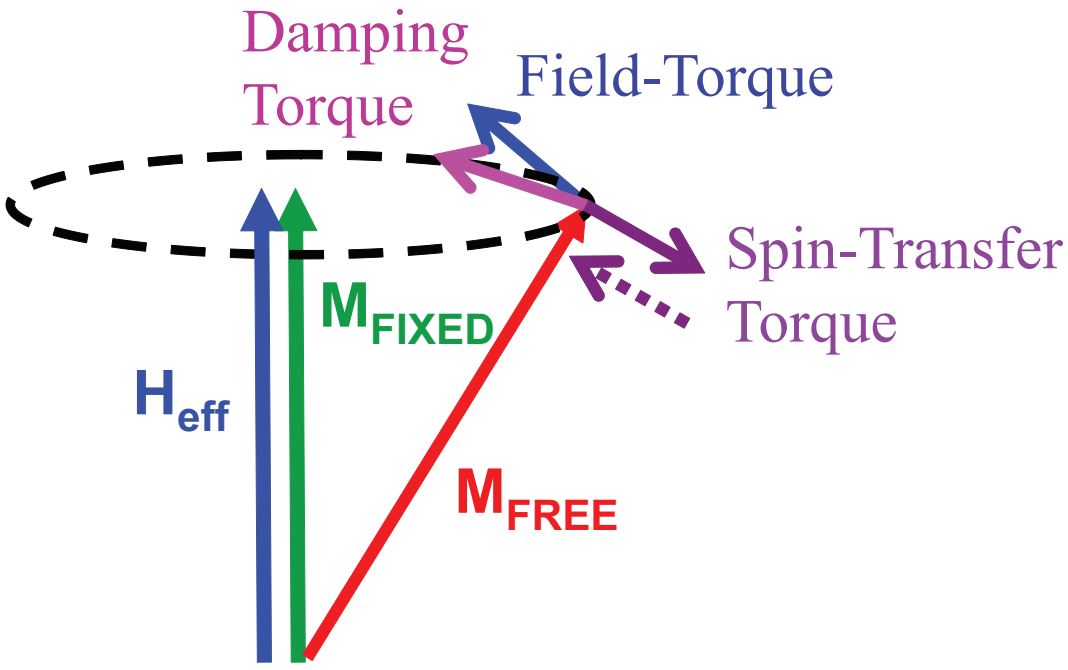


Figure 1.2: Vector diagram of all the torques acting on the free layer: the field-torque, the damping-torque and the spin-transfer torque. The spin-transfer torque supports the damping torque for one sign of current and opposes it for the reverse sign of current.

So far, in the discussion of spin-transfer, we have only talked about the effect of a current. If we now apply a magnetic field as well, the physics becomes even more interesting since there is now a competition between the field torques and the spin-transfer torques. We summarize all the torques on the free-layer in Figure 1.2. Assume that the fixed layer is along the same direction as the external magnetic field. The external magnetic field applies a torque of the form $H \times M_{FR}$ that causes the magnetic free layer to precess about the field. There is also a damping torque, proportional to $M_{FR} \times (H \times M_{FR})$, which applies a torque that pushes the free layer to eventually relax along the external field direction. Finally, the spin-transfer torque has the form of $M_{FR} \times (M_{FR} \times M_{FX})$ and it is proportional to the relative angle between the fixed and free layers. Depending on the sign of the current, the spin-transfer torque can cause the free layer to

align parallel with the fixed layer, in which case the spin-transfer torque and damping torque are in the same direction or the spin-transfer torque can cause the free layer to align anti-parallel with the fixed layer, in which case the spin-transfer torque and damping torque oppose each other.

If we apply a current such that the spin-transfer torque favors the anti-parallel configuration, then depending on the relative magnitude of the damping torque and the spin-transfer torque, we can think of 3 different regimes:
1) Damping torque > Spin-Transfer Torque (for example, if we apply a large magnetic field and a small current): the free layer will eventually just relax along the external field direction (Figure 1.3(a)).
2) Damping torque < Spin-Transfer Torque (for example, if we apply a small magnetic field and a large current): the free layer will switch to the anti-parallel state (Figure 1.3(b)).
3) Damping torque = Spin-Transfer Torque: the free layer will be excited into steady-state oscillations and will emit microwaves (Figure 1.3(c)).

We would like to point out that Figure 1.3 shows a simple case of circular precession in a device with no easy-plane anisotropy. However, typically our magnetic nanopillar devices have a strong easy-plane anisotropy. Therefore, the precession is mostly confined in the easy plane of the device and it follows an elliptical trajectory. We will discuss the elliptical trajectories in more detail in Section 3.4.7.

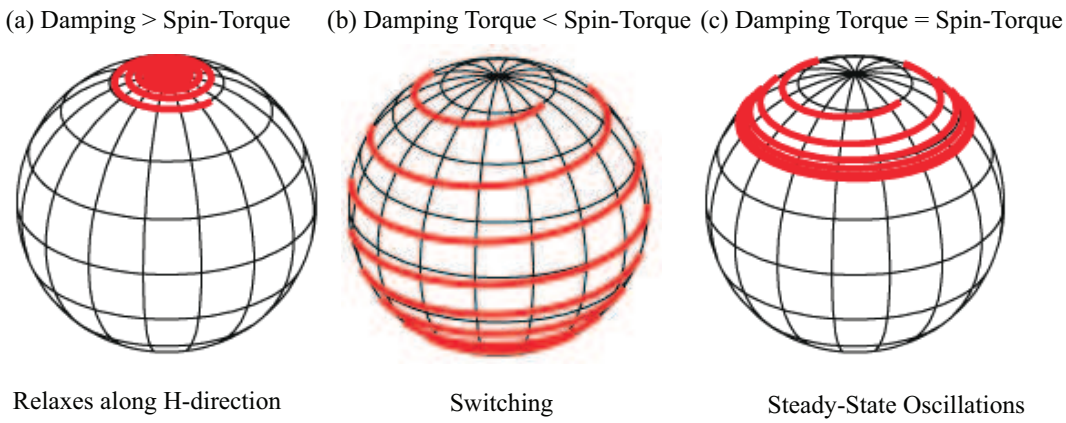


Figure 1.3: Different regimes of spin-transfer. (a) Damping torque > Spin-Transfer torque, the free layer eventually relaxes along the field direction. (b) Damping torque < Spin-Transfer torque, the free layer switches to the anti-parallel configuration. (c) Damping torque = Spin-Transfer torque, the free layer is excited into steady state oscillations. Figure from [9].

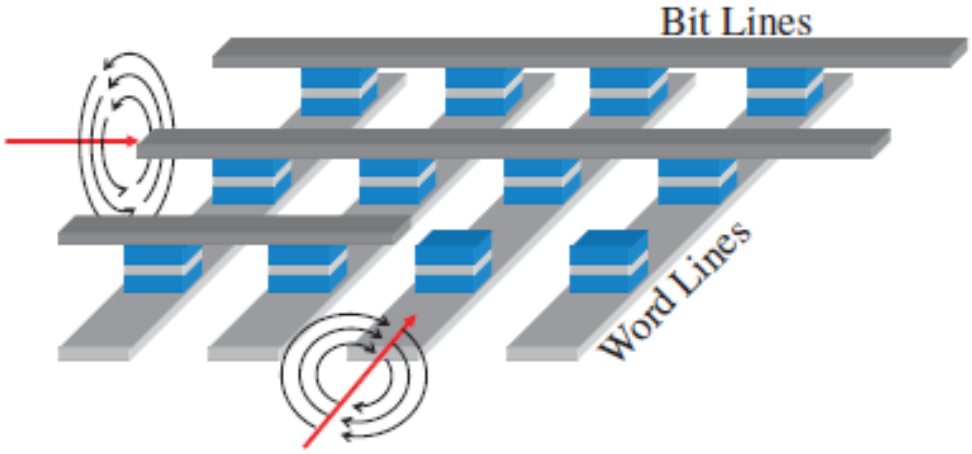
1.1.3 Technological Applications of Spin-Transfer

The spin-transfer torque has promising technological applications. A nice review of the technological outlook for spin-torque has been published by Katine and Fullerton in [10]. The ability of the spin-transfer torque to lead to static parallel and anti-parallel states has applications for writing data and its ability to lead to steady state microwave oscillations has applications for frequency-tunable nanoscale microwave sources. We will discuss these applications briefly below.

Applications of Spin-Torque-Driven Switching

In order to demonstrate the advantage of spin-torque in writing data, we would like to briefly discuss the traditional method for writing data by the cross-point architecture in Magnetic Random Access Memory (MRAM) (Figure 1.4(a)).

(a) MRAM Cross-point architecture



(b) ST-MRAM

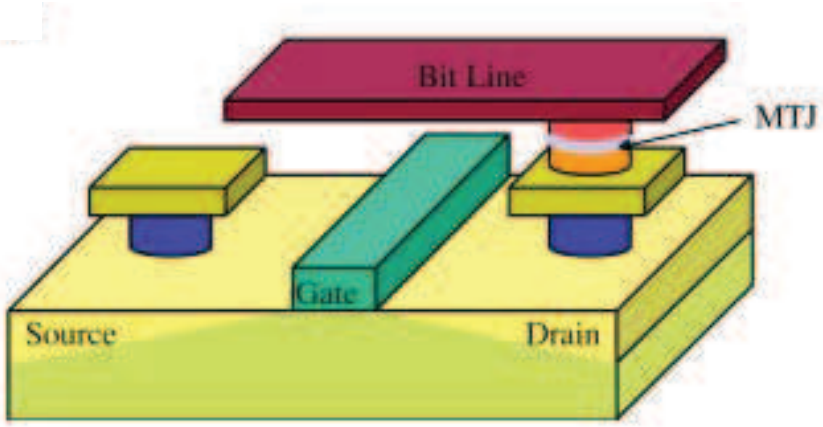


Figure 1.4: (a) MRAM cross-point architecture. (b) ST-MRAM architecture. Figure from [10].

Writing is usually achieved by passing an electrical current through a ”bit line” and a ”write line”. By Ampere’s Law, the current generates a magnetic field and a writes a bit at the cross-point of the bit line and the write line. The bit is a magnetic tunnel junction that is programmed to ”1” or ”0” by aligning the magnetic layers parallel or anti-parallel with the magnetic fields generated by the currents. The advantages of the MRAM cross-point architecture are that it is nonvolatile like FLASH (unlike DRAM and SRAM). Compared to FLASH,

it is fast (20 nanosecond write and read time) and has high endurance (10^{15} cycles). There are some disadvantages to this architecture, however. The biggest problem is that the bits are written by a magnetic field, which is long-range. Because of the wide distribution of switching fields of the neighboring bits, the magnetic field can also write neighboring bits. This is called the "half-select" problem. Freescale developed a prototype of a Toggle MRAM in 2006 [10] that overcame the half-select problem by using synthetic antiferromagnets in the free layer. The writing scheme also has a disadvantage that it is not easily scalable. This is because in addition to scaling down the bits, we also have to scale down the bit lines and the write lines. It also has power consumption issues, since large currents have to be applied across the bit lines and write lines to generate magnetic fields to switch the bits.

In Spin-Torque Magnetic Random Access Memory (ST-MRAM), writing is achieved by passing electrical current through a "bit line" and switching the state of the bit by spin-torque. The advantage of ST-MRAM over traditional MRAM is that it eliminates the half-select problem since each bit is written locally instead of by a long-range magnetic field. In addition, scalability is not as difficult an issue, since there is no need for an external write line. More importantly, switching is determined by the current density rather than by the current. The critical currents for writing depend on the magnetic material's saturation magnetization (M_S), volume (V), damping (α), anisotropy (H_K) and demagnetization fields ($2\pi M_S$).

$$I_C = \frac{2e\ \alpha}{\hbar\eta} M_S V\ (H\ +\ H_K\ +\ 2\,\pi M_S) \tag{1.1}$$

Some of the challenges that still lie ahead for ST-MRAM include reducing the critical currents to make the devices compatible with CMOS as well as to lower

power consumption yet maintain high thermal stability. The energy barrier between the low-resistance and high-resistance states depends on the anisotropy field, the saturation magnetization and the volume.

$$U_A = \frac{H_K \; M_S \; V}{2} \tag{1.2}$$

In Equation 1.1, we can see that to reduce the critical currents, we can engineer materials carefully to reduce their volume, M_S and anisotropies. However, we see in Equation 1.2 that the energy barrier also directly depends on these quantities. So even if these quantities can be made smaller, a balance must be reached so that the activation barrier (U_A) does not also become very small. Another challenge is that the write-current must always be smaller than the read-current to prevent the read-current from changing the state of the bit by spin-torque. On this note, it should also be mentioned that spin-torque can also be a source of noise in read heads if the sensing current starts affecting the bits through spin-transfer effects.

To summarize, the feasibility requirements for ST-MRAM involve lowering the critical current density (J_C) yet maintaining the highest thermal stability (U_A). The desired critical currents, which are limited by CMOS transistors, are about 0.1-0.2 mA ($J_C = 10^6$ A/cm^2). In addition, the data retention time should be 10 years and the threshold for stability should be about 1.3 eV or $\approx$60 k_BT. Several research efforts have been undertaken to reduce the J_C. Some examples are using low M_S materials and high- anisotropy shapes [11], materials with perpendicular anisotropy [12, 13], and reducing damping by engineering sidewall oxides [14].

Another challenge is that spin-valves have high endurance (10^8 A/cm^2) but very small GMR. Magnetic tunnel junctions, on the other hand, have high TMR

but very low endurance (10^7 A/cm^2). Recently, Braganca et al. [15] demonstrated a neat 3-terminal device consisting of both a spin-valve and a magnetic tunnel junction. They wrote data through a spin-valve and read through a magnetic tunnel junction, thereby side-stepping the disadvantages of both systems.

Applications of Spin-Torque-Driven High-Frequency Dynamics

We would now like to briefly discuss the outlook for applications of spin-torque-driven microwave oscillations for making frequency-tunable nanoscale microwave sources for applications in chip-to-chip and wireless communications. For these applications, it is desirable that the oscillations be highly reproducible and periodic, i.e. that they have narrow linewidths in their frequency spectrum. One of the big challenges for spin-torque oscillators is the need for higher output power. Practical GHz communications require microwatts of power. Currently, the maximum power that spin-valves and magnetic tunnel junctions can output are of the order of picoWatts and nanoWatts, respectively.

One promising direction for improving the output power from spin-torque oscillators is to phase-lock an array of several oscillators together. This was demonstrated by Freescale and NIST for 2 oscillators [16, 17]. Kaka et al. [16] used spin-wave interactions to phase-lock two independently connected point-contact oscillators in close proximity and found that the phase-locked state was characterized by a sudden narrowing of the linewidth and increase in power. They demonstrated that the oscillators locked in frequency and the oscillations were phase-coherent so that the combined power was $P_1 + P_2 + 2\sqrt{P_1.P_2}$.

1.2 Overview of this Dissertation

In this dissertation, the main theme of our work has been the study of microwave signals produced by spin-torque-driven magnetization dynamics in magnetic multilayer spin-valve devices with a nanopillar geometry.

In Chapter-2 of this dissertation, we will describe the methods that we employed to fabricate, measure and model our devices. We fabricated all our devices at the Cornell NanoScale Science & Technology Facility (CNF), and we will briefly describe the nano-fabrication procedure in this chapter. We will also discuss in detail the high-frequency techniques that we used to measure the magnetization dynamics. In the first technique, we applied a DC-current and measured an RF-output. In the second technique, we applied a RF-current and measured a DC-output. We used the first technique to study the linewidths of high-frequency dynamics of magnetic nanopillars described in Chapter-3 and the second technique to study the dynamics of antiferromagnet / ferromagnet bilayers in Chapter-4. We will also briefly discuss the macrospin and micromagnetic numerical simulations in Chapter-2.

In Chapter-3, we will discuss our work on the linewidths of precessional oscillations excited by *direct currents* as a function of the in-plane magnetic field angle and temperature. The motivation of this work was to understand the important mechanisms contributing to the linewidths with a view to optimizing the coherence of the oscillations. We will first review the important mechanisms and models for linewidths as well as previous studies of spin-torque oscillator linewidths, and then we will discuss our results and analysis.

In Chapter-4, we will discuss our work on the current-dependence of the

exchange-bias in antiferromagnet / ferromagnet bilayers by exciting them with *radio-frequency (RF) currents*. The motivation of this work was to investigate spin-torque effects in antiferromagnets. We will first review the previous theoretical and experimental work that has been done to investigate spin-torque effects on exchange-bias, and then we will discuss our results and analysis.

In Chapter-5, we will present all our conclusions from the dissertation.

REFERENCES

[1] http://www.intel.com/technology/mooreslaw.

[2] Grunberg P.A., Nobel lecture: From spin waves to giant magnetoresistance and beyond, *Rev. Mod. Phys.* **80**, 1531 (2008).

[3] Binasch G., Grnberg P., Saurenbach F., & Zinn W., Enhanced magnetoresistance in layered magnetic structures with antiferromagnetic interlayer exchange, *Phys. Rev. B* **39**, 4828 LP (1989).

[4] Baibich M.N., Broto J.M., Fert A., Van Dau F.N., Petroff F., Etienne P., Creuzet G., Friederich A., & Chazelas J., Giant magnetoresistance of (001)fe/(001)cr magnetic superlattices, *Phys. Rev. Lett.* **61**, 2472 LP (1988).

[5] Slonczewski J.C., Current-driven excitation of magnetic multilayers, *J. Magn. Magn. Mater.* **159**, L1 (1996).

[6] Berger L., Emission of spin waves by a magnetic multilayer traversed by a current, *Phys. Rev. B* **54**, 9353 LP (1996).

[7] Katine J.A., Albert F.J., Buhrman R.A., Myers E.B., & Ralph D.C., Current-driven magnetization reversal and spin-wave excitations in co/cu/co pillars, *Phys. Rev. Lett.* **84**, 3149 (2000).

[8] Kiselev S.I., Sankey J.C., Krivorotov I.N., Emley N.C., Schoelkopf R.J., Buhrman R.A., & Ralph D.C., Microwave oscillations of a nanomagnet driven by a spin-polarized current, *Nature* **425**, 380 (2003).

[9] Ralph D. & Stiles M., Spin transfer torques, *J. Magn. Magn. Mater.* **320**, 1190 (2008).

[10] Katine J. & Fullerton E.E., Device implications of spin-transfer torques, *J. Magn. Magn. Mater.* **320**, 1217 (2008).

[11] Braganca P.M., Krivorotov I.N., Ozatay O., Garcia A.G.F., Emley N.C., Sankey J.C., Ralph D.C., & Buhrman R.A., Reducing the critical current for short-pulse spin-transfer switching of nanomagnets, *Appl. Phys. Lett.* **87**, 112507 (2005).

[12] Mangin S., Ravelosona D., Katine J.A., Carey M.J., Terris B.D., & Fullerton

E.E., Current-induced magnetization reversal in nanopillars with perpendicular anisotropy, *Nature Materials* **5**, 210 (2006).

[13] Liu L., Moriyama T., Ralph D.C., & Buhrman R.A., Reduction of the spin-torque critical current by partially canceling the free layer demagnetization field, *Appl. Phys. Lett.* **94**, 122508 (2009).

[14] Ozatay O., Gowtham P.G., Tan K.W., Read J.C., Mkhoyan K.A., Thomas M.G., Fuchs G.D., Braganca P.M., Ryan E.M., Thadani K.V., Silcox J., Ralph D.C., & Buhrman R.A., Sidewall oxide effects on spin-torque- and magnetic-field-induced reversal characteristics of thin-film nanomagnets, *Nature Materials* **7**, 567 (2008).

[15] Braganca P.M., Katine J.A., Emley N.C., Mauri D., Childress J.R., Rice P.M., Delenia E., Ralph D.C., & Buhrman R.A., A three-terminal approach to developing spin-torque written magnetic random access memory cells, *IEEE Trans. on Nanotechnology* **8**, 190 (2009).

[16] Kaka S., Pufall M.R., Rippard W.H., Silva T.J., Russek S.E., & Katine J.A., Mutual phase-locking of microwave spin torque nano-oscillators, *Nature* **437**, 389 (2005).

[17] Mancoff F.B., Rizzo N.D., Engel B.N., & Tehrani S., Phase-locking in double-point-contact spin-transfer devices, *Nature* **437**, 393 (2005).

CHAPTER 2

METHODS: NANO-FABRICATION, MEASUREMENTS & MODELING

In this chapter, we will describe the methods that we employed to fabricate, measure and model our magnetic nanopillar devices. We fabricated all our devices at the Cornell NanoScale Science & Technology Facility (CNF) and we will briefly describe the nano-fabrication process in Section 2.1. In Section 2.2, we will describe in detail the DC-characterization and the high-frequency techniques to measure the microwave signals from our devices. We will also describe the operation of the commonly used room-temperature and cryogenic probe-stations. Finally, in Section 2.3, we will describe the numerical simulations (macrospin and micromagnetic) that we undertook to model our devices.

2.1 Nano-Fabrication

In this section, we will briefly discuss the nano-fabrication process that we used to make the magnetic nanopillar devices. The nanopillar fabrication process at Cornell has been well-documented and is described in detail in Reference [1], as well as previous Ph.D. theses [2, 3, 4, 5]. Therefore, we will not delve into too much detail of the process in this thesis. Instead, we will just give a brief overview of the process and also share some personal pointers and tricks that we found useful during the nano-fabrication of our devices.

Sputtering Magnetic Layers

We start with a blank silicon wafer with about 1000 nanometers (nm) of silicon oxide. The first step in the fabrication process is sputtering thin films of all the

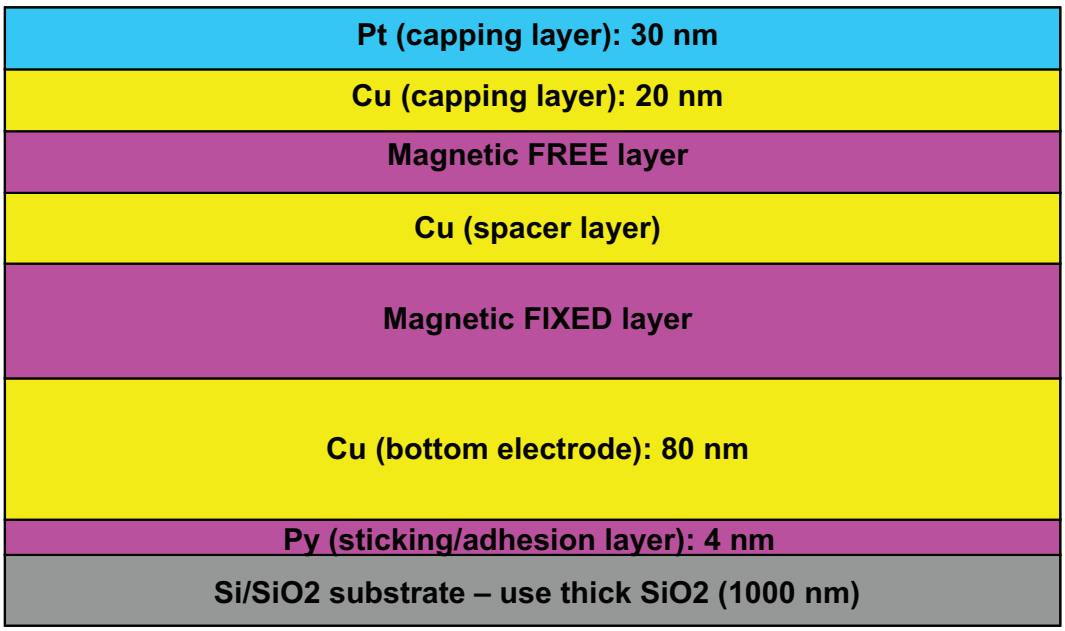


Figure 2.1: Sputtered multilayer stack for nanopillar fabrication.

layers, including the magnetic layers (Figure 2.1). The first layer (Permalloy, $Ni_{81}Fe_{19}$; 4 nm) is usually a "sticking" layer to promote adhesion between the magnetic films stack and the silicon-oxide on the wafer. The next layer is the Copper (Cu) bottom electrode (usually 80 nm), then the magnetic fixed layer, the Cu spacer and the magnetic free layer. Finally, the top capping layers: Cu (20 nm) / Pt (30 nm) are sputtered to prevent the magnetic layers from oxidation.

In order to make the coercivity of the magnetic fixed layer higher than that of the free layer, we either make the fixed layer much thicker than the free layer or we pin its magnetization in a certain direction by exchange-biasing it to an antiferromagnet. We sputter all our films in the AJA sputtering system in the Buhrman group. For layers that require an antiferromagnet to exchange-bias one of the magnetic layers, we use the magnetic stage in the AJA to sputter the layers in a magnetic field (300 Oe). We anneal at 220°C for 85 minutes inside the AJA and then let the layers cool down in the presence of the magnetic field to

pin the exchange-bias along a certain direction.

Evaporating Carbon

After sputtering all the layers, we evaporate 50 nm of Carbon on top of the Pt capping layer in the odd-hours evaporator at the Cornell Nanoscale Facility (CNF). The Carbon acts as a mask for the nanopillar in a later step of the fabrication process. It is important to evaporate Carbon within 24 hours of sputtering, otherwise moisture accumulates on the wafer and the evaporated Carbon does not adhere well and peels off during liftoff at a later stage. The Carbon can be evaporated in the odd-hours or even-hours evaporator at CNF. However, we have found that the even-hours evaporator spits a lot of Carbon during evaporation and makes it very difficult to control the evaporation rate, so we recommend using the odd-hours evaporator whenever possible.

Electron-beam lithography

The next step is to define the nanopillar devices by electron-beam lithography. We first spin a bilayer of PMMA resist to give a good undercut. In case the spun resist film does not look okay, we have found it very risky to strip PMMA resist with acetone and IPA at this stage, because these solvents can attack the carbon underneath the resist and peel it off as well. So we usually just proceed with the spun resist, even if it is non-uniform in some areas of the wafer.

Next, we do e-beam lithography on the Leica VB6 system and develop the PMMA resist. Our devices are usually circular or elliptical-shaped with dimensions of the order of several tens of nanometers. In a typical fabrication run, we try different shapes and sizes of devices. We show Scanning Electron Microscope (SEM) images of some devices in Figure 2.2. It is always good practice to do a dose-test on a test wafer with exactly the same layer-structure as the

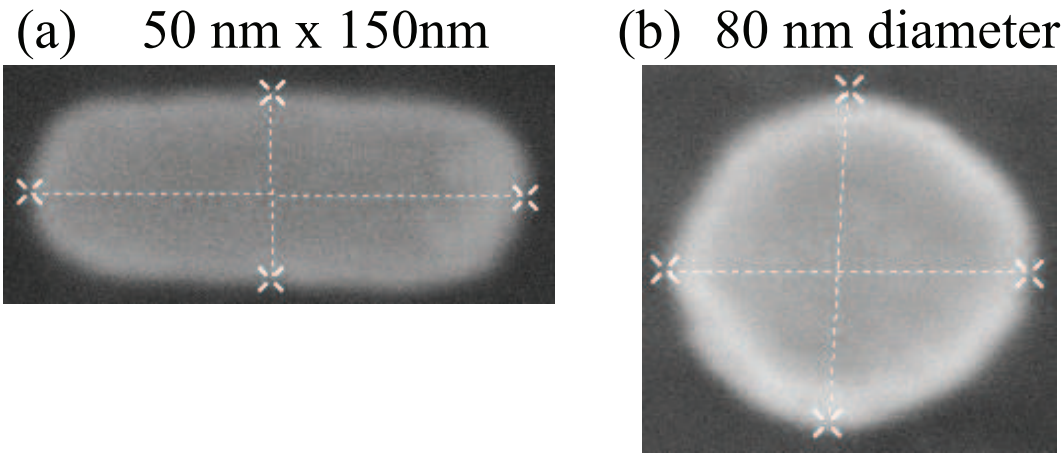


Figure 2.2: Scanning Electron Microscope (SEM) images of (a) an elliptical device and (b) a circular device after electron-beam lithography.

regular wafers, before exposing the latter. The dose-test jobfile was written by Patrick Braganca and is described in detail in his Ph.D. thesis [5].

During the e-beam exposure of the wafers, in addition to the devices, the jobfile also defines several alignment marks. These alignment marks are crucial for the later photolithography steps when we use these to align the top and bottom electrodes with the device.

After developing the e-beam resist, we evaporate Chrome (Cr) on top of the carbon layer in the odd-hours evaporator at CNF. The Cr acts as a mask for the carbon during a later step in the nanofabrication process. Next, we strip the PMMA resist and remove the carbon from everywhere except above the devices by Reactive Ion Etching (RIE) in an oxygen plasma in the PT-72 tool at CNF.

Photolithography-1 + Ion Mill-1: Isolate devices

In the first photolithography step, we pattern the top and bottom electrodes for

each device as well as isolate different devices by etching through the magnetic layers into the silicon-oxide of the wafer (Figure 2.3(a)). The square pads are the bottom electrodes and the spaceship-shaped pads are the top electrodes. The nanopillar device (not visible) is at the center.

The first photolithography step is crucial, because we align the alignment marks of the photolithography mask with the alignment marks that were made during the e-beam step (Figure 2.4). The alignment marks are to the left of the (5, 1) die and to the right of the (5, 9) die, and they are more easily found by locating a triangle defined next to them during e-beam (Figure 2.4(a)). Excellent alignment is very important (Figure 2.4(b)), because this step affects the relative position of the device with respect to the electrodes and hence affects all future processing steps.

After ion-milling into the oxide, a typical profilometry scan of the etch-depth looks as shown in Figure 2.3(b). It is important to make sure that the devices are electrically isolated at this stage; we usually test this by checking the resistance at different points of the wafer with a multimeter and expect it to be very high. Another indication that we have etched into the oxide is the color of the oxide, which should be bluish-purple.

Photolithography-2 + Ion Mill-2: Define bottom leads

Once the devices and electrodes have been electrically isolated from each other as well as other devices on the wafer, next we define the bottom leads. If we want the fixed layer to be patterned, we etch the magnetic layers 50% into the bottom Cu electrode. If we want the fixed layer to be extended, we etch into the fixed layer till about 10% of the fixed layer thickness. The Carbon and Cr masks that were evaporated earlier act as a mask for the nanopillar in this step to pre-

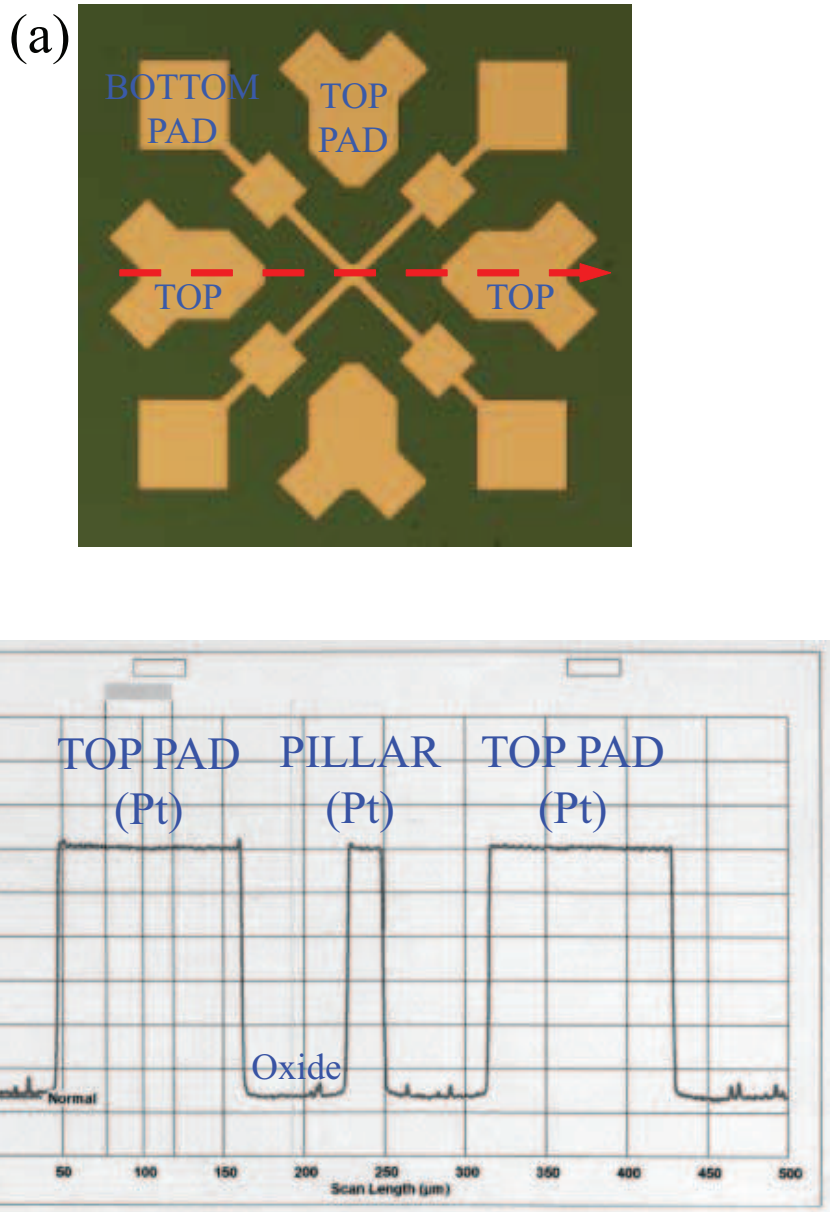


Figure 2.3: Photolithography-1 + Ion Mill-1. (a) Optical image of top pads (spaceship-shaped), bottom pads (square-shaped) and bottom leads. The nanopillar device (not visible) is at the center of the electrodes and leads. The red dashed line is the path of the (b) profilometry scan. We scan between two top pads across the device in the center.

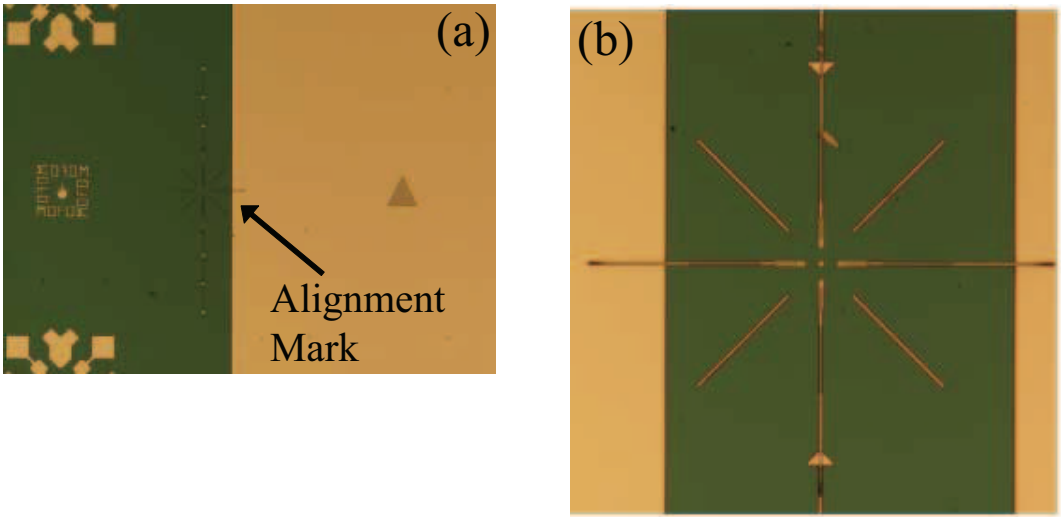


Figure 2.4: Alignment marks defined during e-beam and photolithography. (a) The alignment marks are at the left of the (5,1) die and at the right of the (5,9) die, and can be easily located by triangles next to these two die. (b) Example of good alignment between the alignment marks defined during e-beam and later during photolithography.

vent it from getting milled away as well. Figure 2.5(a) shows an optical image of the bottom leads after ion-milling and Figure 2.5(b) shows a profilometry scan of the etch-depth. For the device in Figure 2.5(b), we etched about 80 nm from the top of the Pt. We can see this is also the difference between the height of the top pad and the bottom lead in the center.

PECVD Oxide + Planarization (Ion Mill-3)

Next, we deposit silicon-oxide by Plasma Enhanced Chemical Vapor Deposition (PECVD) in the IPE-PECVD system at CNF to isolate the devices and electrodes. The typical procedure for the PECVD is: (1) clean the chamber with O_2, (2) condition the chamber with SiO_2, (3) deposit SiO_2 on the wafers, (4) clean the chamber with O_2. We usually use the soft-pumpdown procedure to prevent the wafers from moving around during the pumpdown.

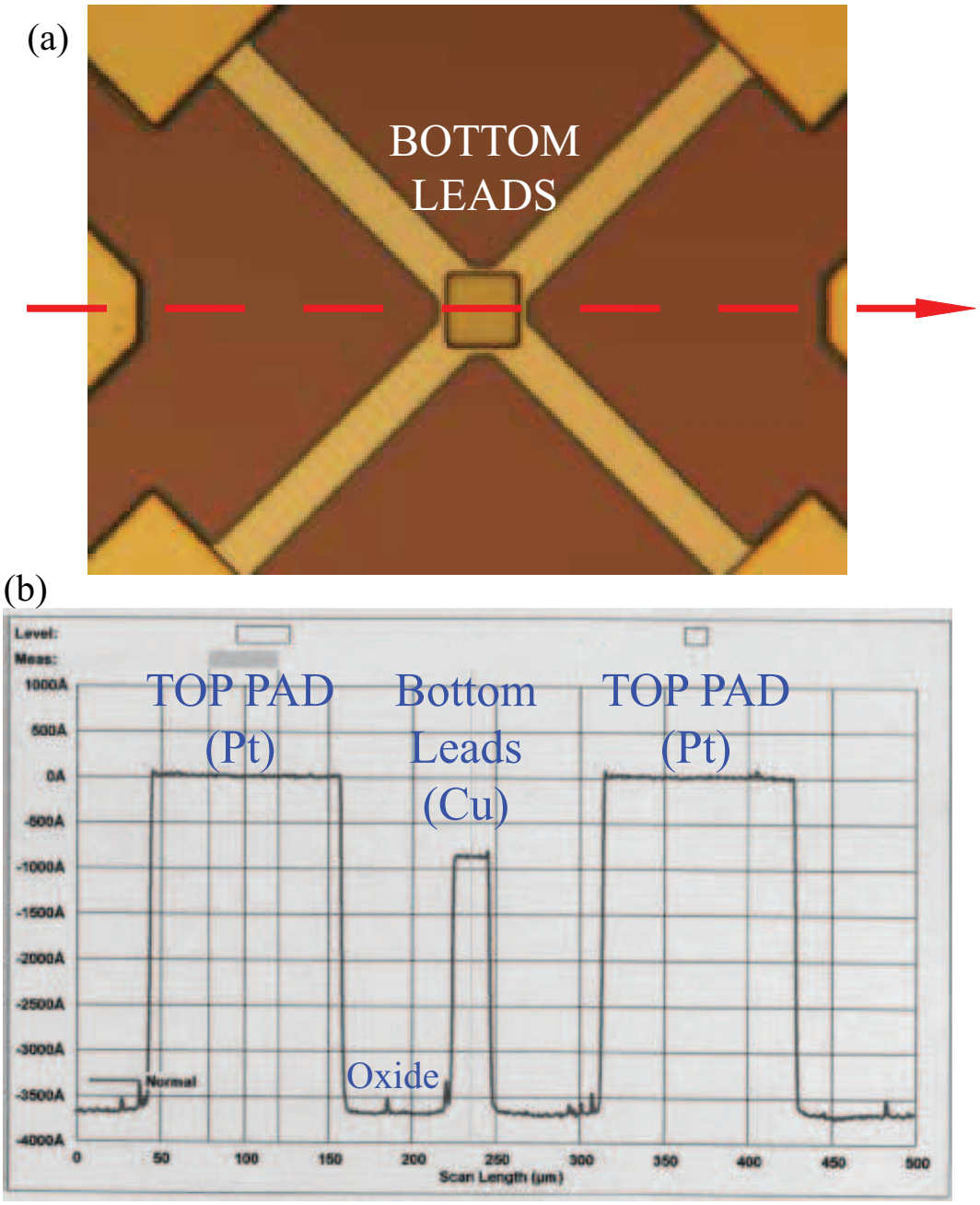


Figure 2.5: Photolithography-2 + Ion Mill-2. (a) Optical image of bottom leads after milling. We can see the color of the bottom leads (diagonal lines) is different from the color of the pads (partial squares near the edges). The bottom leads were milled all the way to the Cu bottom electrode, while the top-layer of the pads is Pt. The red dashed line is the path of the (b) profilometry scan. We scan between two top pads across the device and bottom leads in the center. We etched about 80 nm into the bottom leads, and the profilometry scan shows this as the difference between the top pads (Pt) and the bottom leads (Cu).

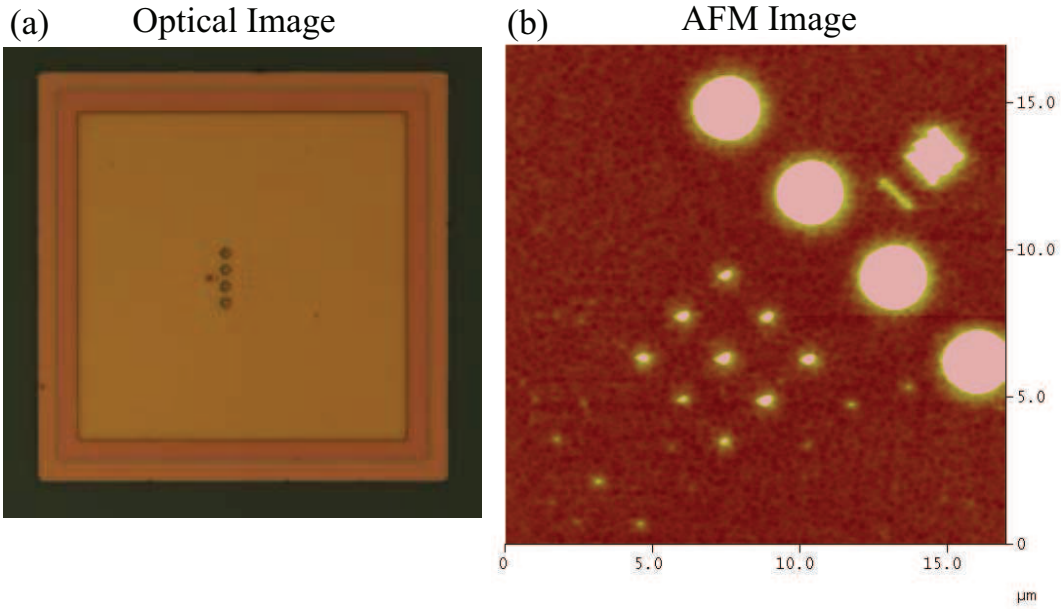


Figure 2.6: (a) Optical image and (b) AFM image (rotated by 45°) of the test-array of devices that we measure with the AFM after planarization (Ion Mill-3). This test-array is defined by e-beam lithography inside a small square near the center of each of the 81 die on the wafer. The array can be located by four big circles (as shown); the array of test devices is on each side of this column of circles.

After depositing about 300-500 nm of silicon-oxide everywhere on the wafer, we planarize the oxide to flatten the bump above the pillar. This is usually done in the ion-mill. In order to check if we planarized the correct amount, we take Atomic Force Microscopy (AFM) images of a test array of devices on a few die of the wafer (Figure 2.6) (this test array of devices was defined in the e-beam step earlier; the test array is inside a small square right above the arrow at the center of every die). If the oxide above the nanopillars is planarized to within 5-20 nm, we proceed to the next step, otherwise we planarize the oxide some more. Figure 2.7 (a) shows an example of the AFM height profile for under-planarized devices, where the bump above the pillar is not flattened and is almost 100 nm in height. Figure 2.7 (b) shows the height profile for the same devices after being planarized some more. Figure 2.8 (a)-(b) show a surface plot of the same

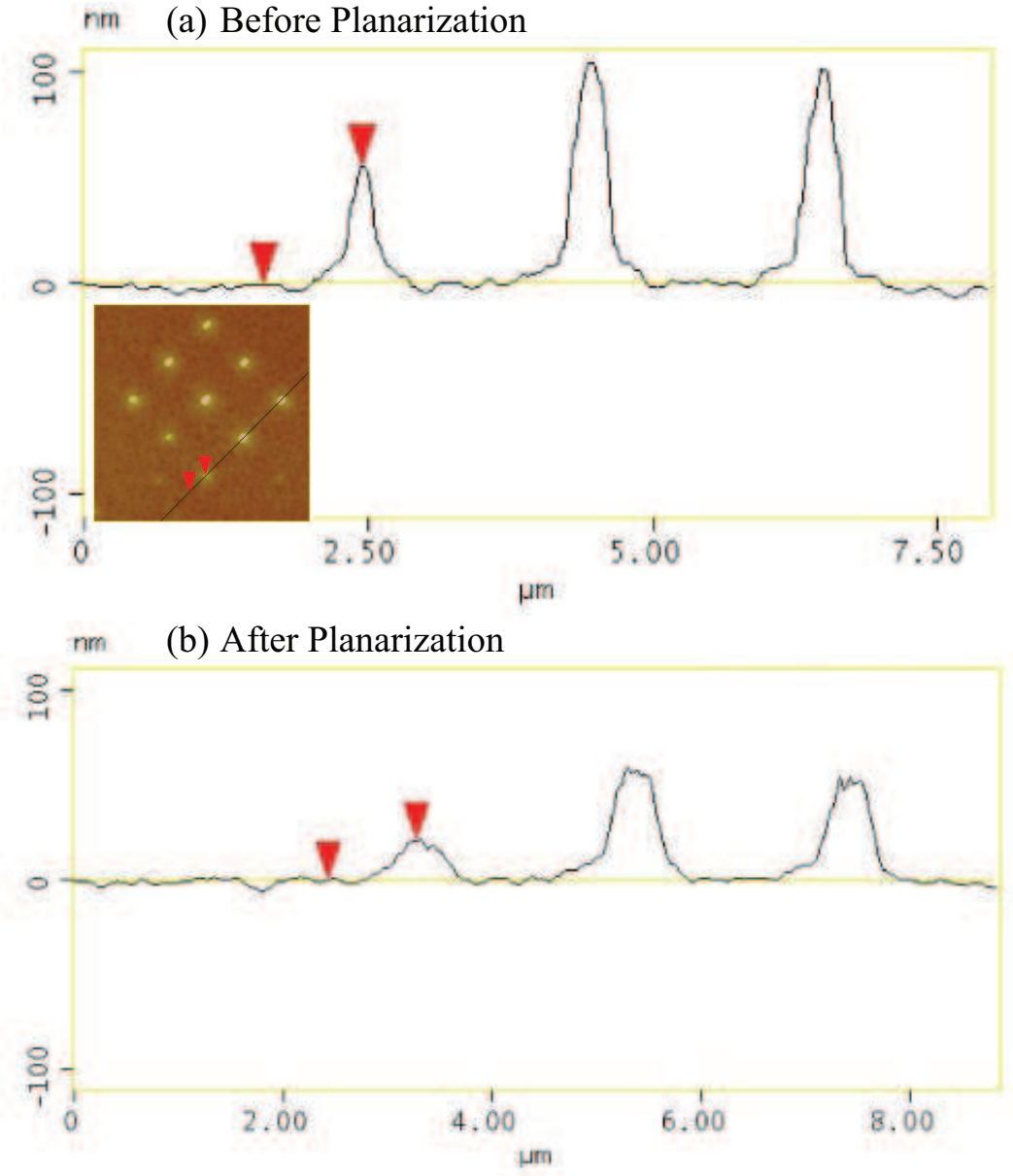


Figure 2.7: AFM height measurements of the test-array of devices (a) before and (b) after planarization. The inset of (a) shows an AFM image of the devices.

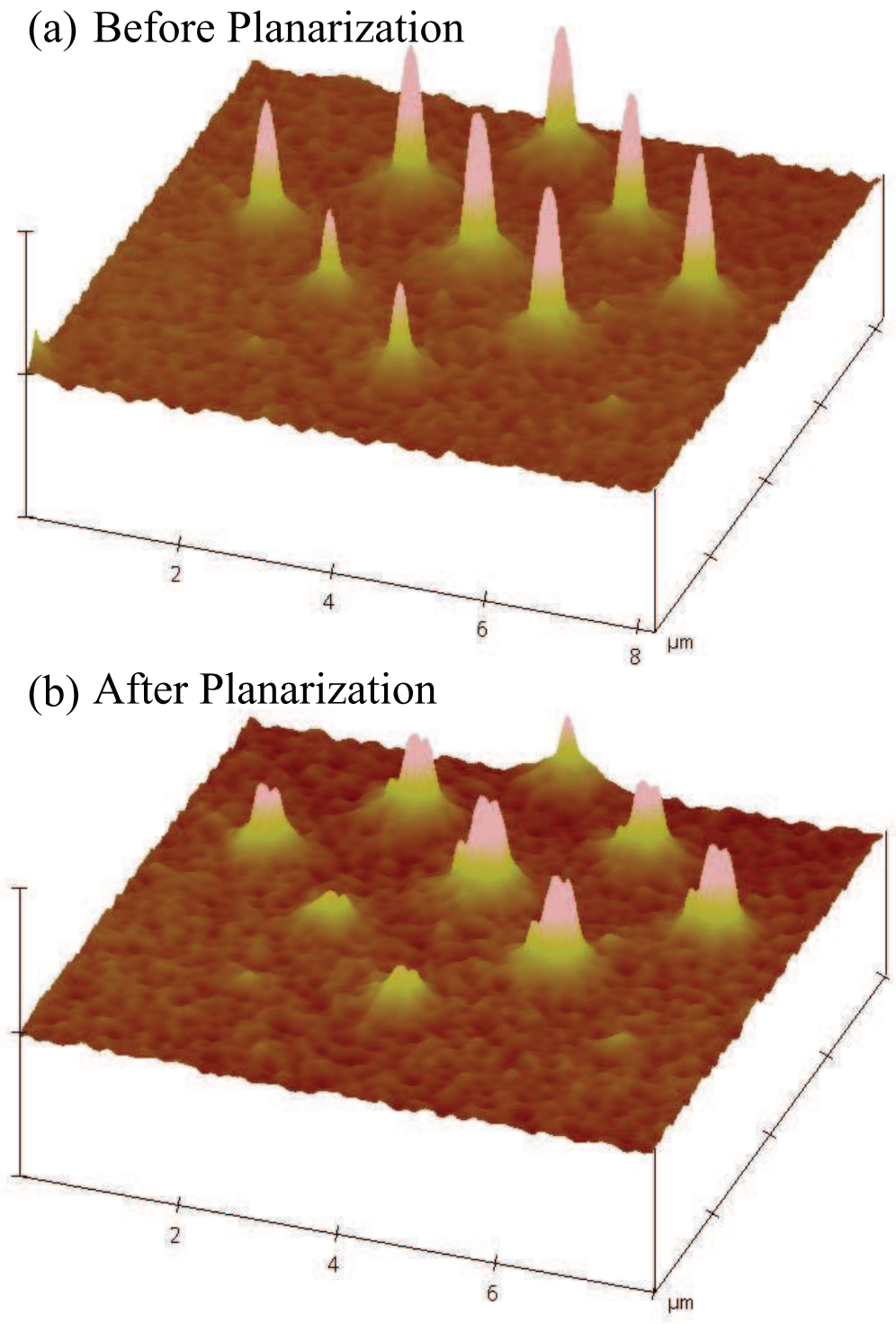


Figure 2.8: AFM surface-plot measurements of the test-array of devices (a) before and (b) after planarization. The scale in (a) and (b) is 100 nm/division.

device array before and after planarization. One note of caution at this step: it is absolutely critical not to over-planarize by over-milling the oxide. This happens when so much oxide is milled away that the oxide above the bottom leads starts approaching the same height as the top of the nanopillar, thereby leading to part of the nanopillar also getting etched away during the planarization. If the top of the pillar gets etched away, there is no way to salvage it and we have to start a new fabrication process all over from scratch.

Photolithography-3 + BOE etch

At this point of the fabrication process, there is oxide above everything on the wafer, including the devices and electrodes. The next few steps involve selectively removing oxide above the devices and electrodes to make electrical contact to them. This is done by selectively protecting different areas in a series of photolithography steps. First, we remove oxide above the top and bottom pads by BOE etch. Figure 2.9(a) shows a profilometry scan after the BOE etch.

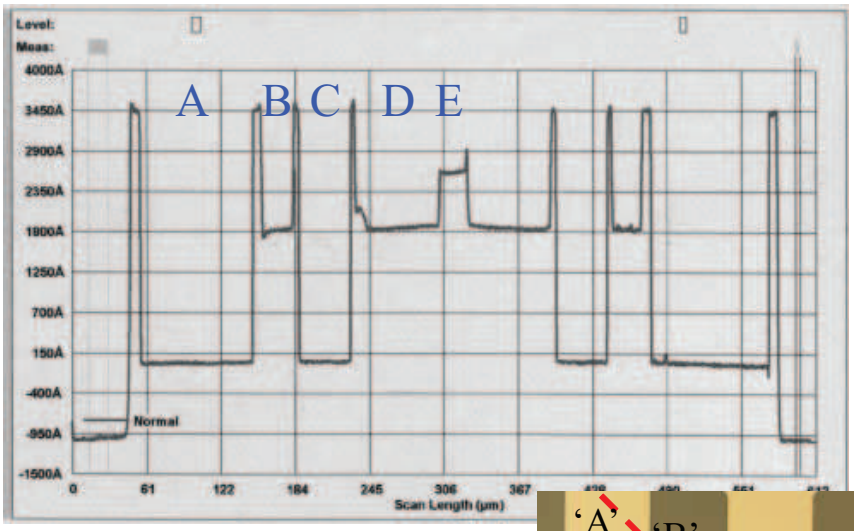
Photolithography-4 + deposit 100 nm of SiO2

Next, we evaporate 100 nm of SiO_2 to protect the top leads from shorting at a later step. The inset of Figure 2.9(b) shows an optical image of the area where SiO_2 is evaporated to protect shorts and Figure 2.9(b) shows the profilometry scan after 100 nm of SiO_2 is deposited over the leads.

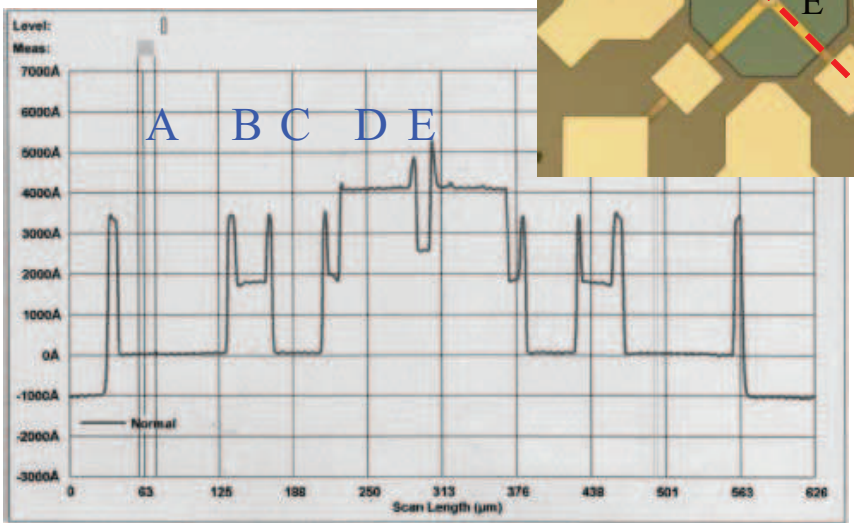
Photolithography-5, Ion Mill-4 + Photolithography-6, Ion Mill-5

The final steps involve carefully removing the oxide above the nanopillar. This is done in two stages. In Photolithography-5 and Ion Mill-4, we mill away part of the oxide and use this step as a calibration for the oxide etch rate. Figure 2.10(a)-(b) shows profilometry scans before and after the etch. In Photolithography-6, we use the oxide etch rate determined in the previous step

(a) After PL-3 + BOE etch



(b) After PL-4 +
100 nm oxide above 'D'



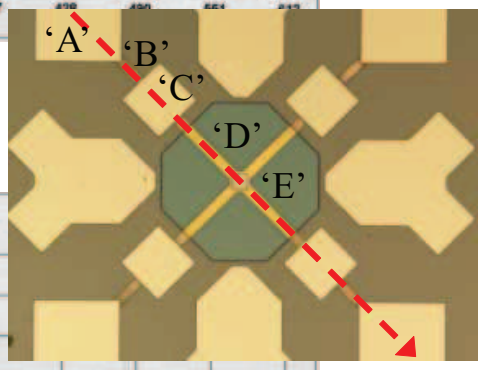
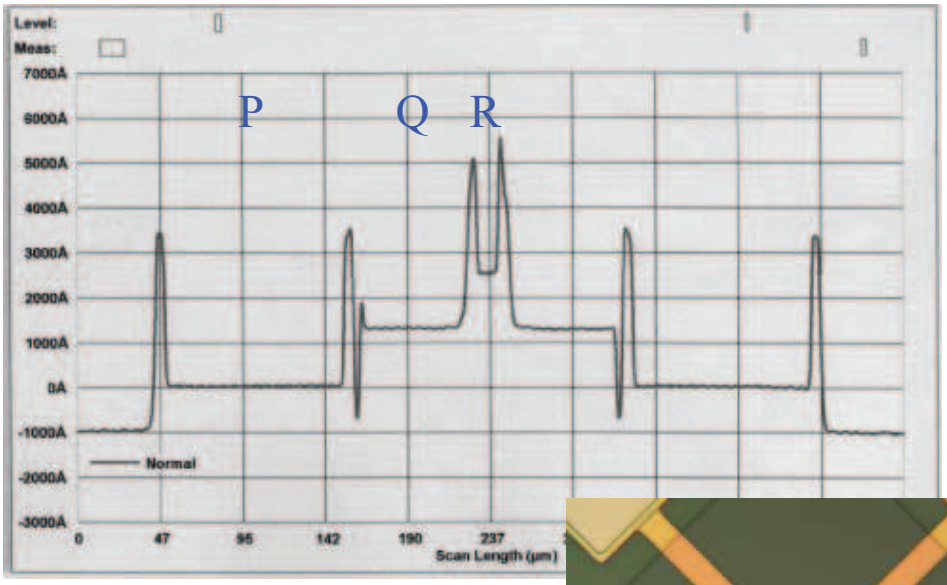
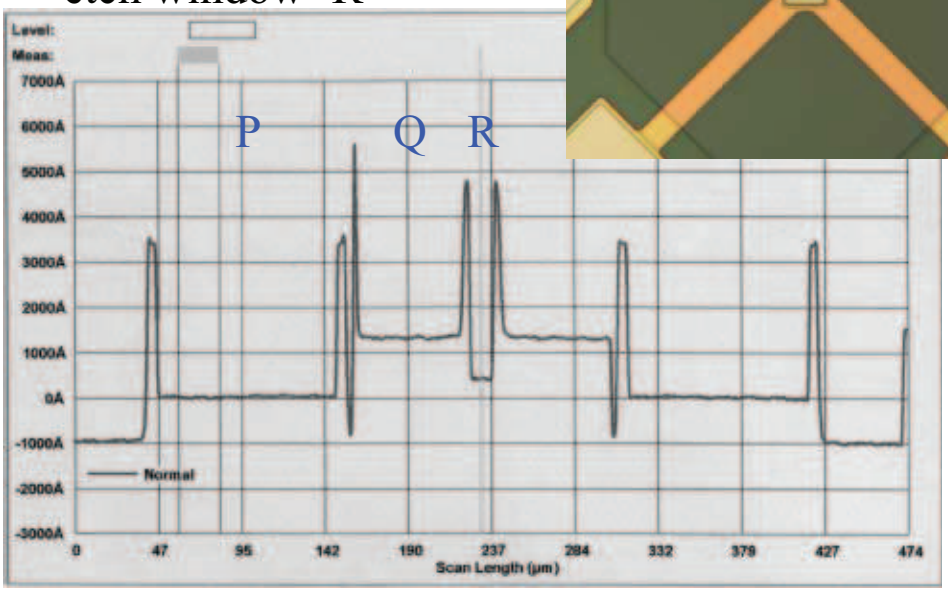


Figure 2.9: Profilometry scans of the oxide height after (a) (PL-3 + BOE etch) and (b) (PL-4 + 100-200 nm of oxide evaporation above top leads). The inset of (b) shows an optical image of the area (green hexagon) above the top leads where 100-200 nm of oxide is evaporated to prevent shorting. The red dashed line is the path of the profilometry scans in (a) and (b). We scan from the bottom pads (″A″) across the bottom leads (″B″), small bottom pads (″C″), bottom leads (″D″) and device area (″E″). ″A″ and ″C″ are the same height (Pt) since they are the top of the bottom pads and the BOE removes the oxide above these pads, ″B″ and ″D″ are the oxide height above the bottom leads. In (b), the height of ″D″ is above the height of ″B″ by about 200 nm after more oxide is evaporated.

(a) After PL-4 + 100 nm oxide



(b) After PL-5 +
etch window 'R'



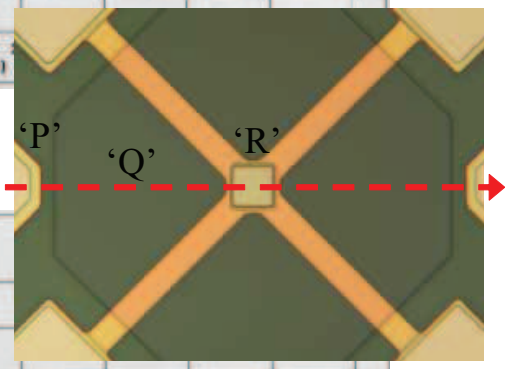


Figure 2.10: Profilometry scans of the oxide height after (a) (PL-4 + 100-200 nm of oxide evaporation above top leads) and (b) (PL-5 + IM-4). The inset of (b) shows an optical image of the small square etch-window around the device. The red dashed line is the path of the profilometry scans in (a) and (b). We scan from the top pads (″P″) across the top-lead area (″Q″) and the device area (″R″). In (a), the height difference between the oxide above the top-lead area (″Q″) and the device area (″R″) is 130 nm. (b) After PL-5 and etching through the small window ″R″, the height difference becomes -70 nm).

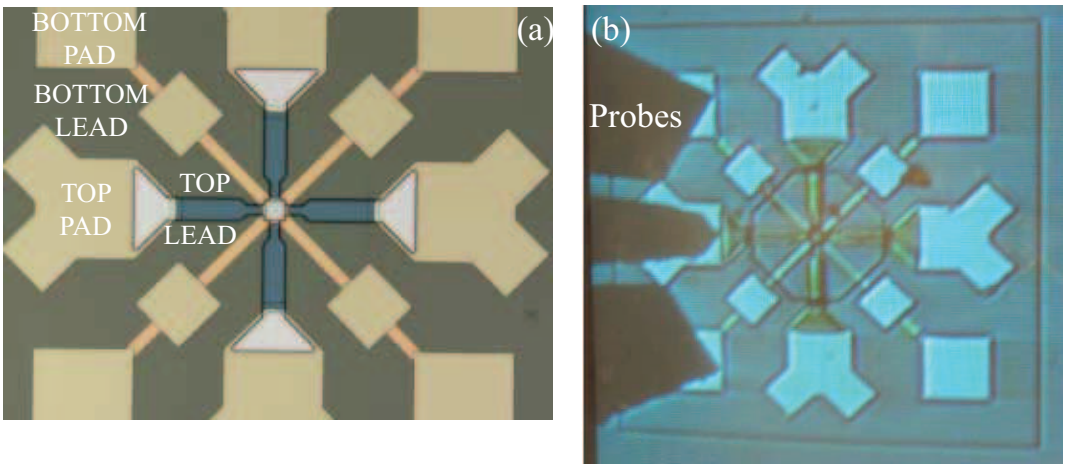


Figure 2.11: (a) Optical image of the completed devices, electrodes and leads after PL-6 + IM-5 and IM-6. We can see the top leads defined after PL-6, just before we deposit Cu above them to make electrical contact. (b) The devices are contacted and electrically characterized by RF-probes.

to mill away all the oxide above the pillar and define the top leads (Figure 2.11 (a)). Finally, we make contact to the top of the nanopillar by depositing Cu over the top-leads. We do all subsequent electrical characterization by contacting the top and bottom pads with probes (Figure 2.11 (b)).

2.2 Measurements

2.2.1 dV/dI Measurement

In order to measure the resistance of our devices, we bias the devices with a current-source and measure the voltage (we current-bias instead of voltage-bias the device, because the resistance of our spin-valve devices is small, of the order of several tens of Ω's). A schematic of our home-made current-source is shown

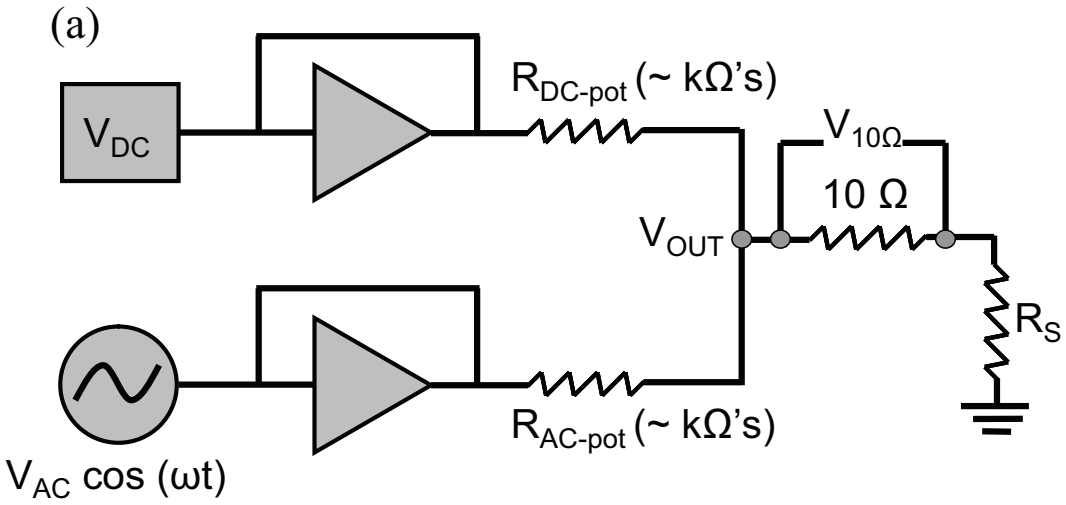


Figure 2.12: Schematic of home-made current-source to bias the devices.

in Figure 2.12. In the current-source, we use two voltage followers for the DC and the AC parts of the current-source. The DC voltage, V_{DC} is supplied from a DAQ card and the AC voltage, V_{AC} is supplied from the reference channel of a lock-in. The DC and AC voltages are put across two variable-resistance potentiometers, R_{DC-pot} and R_{AC-pot}, which are of several kΩ's, thereby acting as a current-source. The resistors are large, so that constant current can be applied to the device despite any changes in the device resistance.

In order to measure the current going through the device, a 10Ω resistor is put in series with the device and the voltage is measured across the 10Ω sensing resistor. Since the device and the sensing 10Ω resistor are in series, the same current passes through both of them. The resistance of the sensing resistor is chosen to be small, so that there is not a large voltage drop across it. The output of the current-source is given by:

$$V_{OUT} = V_{DC}\frac{R_S + 10\Omega}{R_S + 10\Omega + R_{DC-pot}} + V_{AC}\cos(\omega t)\frac{R_S + 10\Omega}{R_S + 10\Omega + R_{AC-pot}} \qquad (2.1)$$

The DC-resistance of the device is determined by dividing the DC-voltage

across the device by the DC-current measured from the 10Ω resistor.

$$R_{S,DC} = \frac{V_{DC-sample}}{I_{10\Omega}} = \frac{V_{DC-sample}}{\frac{V_{10\Omega}}{10\Omega}} \tag{2.2}$$

The AC-resistance of the device is determined by dividing the AC-voltage across the sample (measured with a lock-in amplifier, Equation 2.4) by the AC-current (Equation 2.5). The AC-current is determined from the AC-voltage across the 10Ω and R_{AC-pot}, which is the difference between the total AC-voltage drop across the 10Ω, R_{AC-pot} and R_S and the AC-voltage drop across just R_S.

$$R_{S,AC} = \frac{V_{AC-sample}}{I_{AC}} \tag{2.3}$$

$$V_{AC-sample} = \frac{V_{lock-in} \times Sensitivity}{10} \tag{2.4}$$

$$I_{AC} = \frac{V_{AC-(10\Omega+R_{AC-pot})}}{10\Omega + R_{AC-pot}} = \frac{V_{AC-sample}}{10\Omega + R_{AC-pot}} \frac{R_{S,DC} + 10\Omega + R_{AC-pot}}{R_{S,DC}} - \frac{V_{AC-sample}}{10\Omega + R_{AC-pot}} \tag{2.5}$$

2.2.2 High Frequency DC-Spectra Measurements

As discussed in Chapter 1, the spin-transfer-torque can cause the magnetic layers to switch reversibly between parallel and anti-parallel orientation, or precess in steady-state oscillations in the microwave-frequency regime. The first direct measurements of these high-frequency oscillations were undertaken at Cornell and the measurement technique was developed by Prof. Dan Ralph, Jack Sankey and Sergey Kiselev in their seminal paper [6]. We employed this technique to study the linewidths of the high-frequency oscillations in Chapter 3 and we will describe it briefly in this section.

A schematic of the circuit is shown in Figure 2.13. The oscillations are measured by a heterodyne mixing scheme [6]. A DC current is applied across the

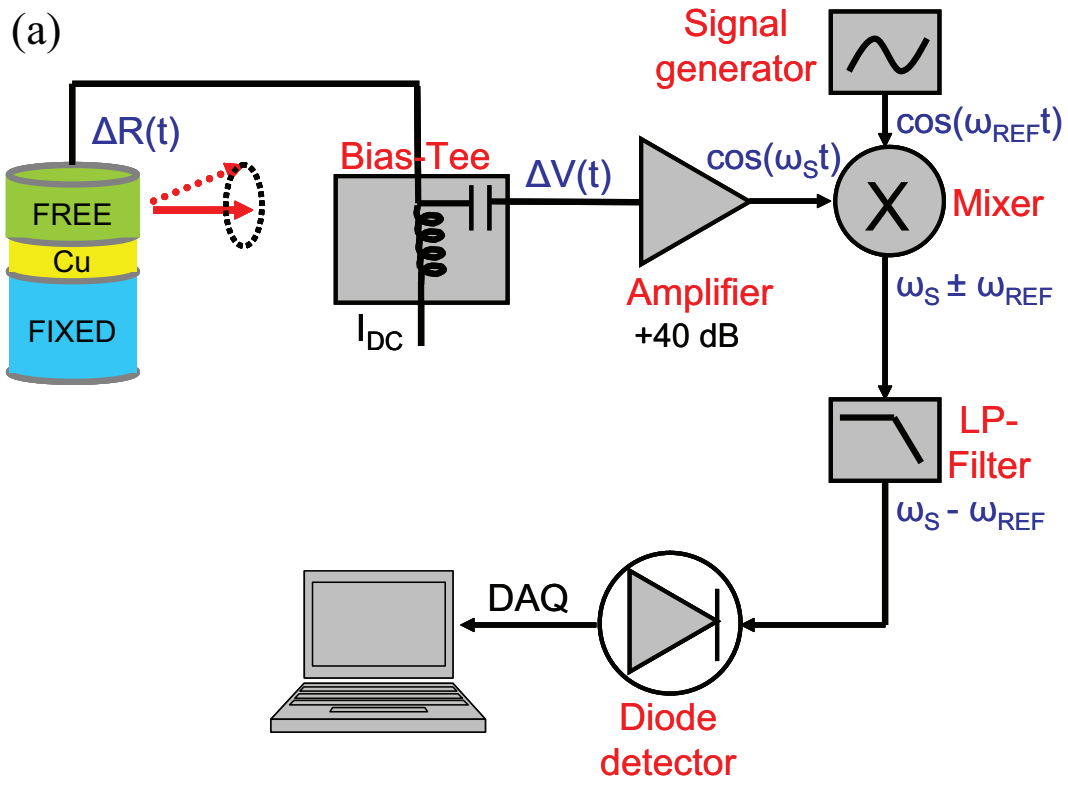


Figure 2.13: Schematic of circuit and heterodyne mixing technique to measure DC-driven microwave frequency dynamics.

sample from the DC-port of a bias-tee; due to spin-transfer-torque, the free layer starts precessing and because of the GMR effect, there is an oscillating change in resistance ΔR(t) and therefore, a time-varying voltage, ΔV(t). The oscillating voltage signal from the sample is fed into a bias-tee. The AC component of the signal at frequency ω_S is amplified and fed into the RF-port of a mixer. An external signal-generator sweeps frequencies between ω_{REF} = 0-20 GHz (RF power = +12 dBm), which are fed into the LO-port of the mixer. The mixer multiplies the two sinusoidal signals at frequencies ω_S and ω_{REF} and outputs signals of two frequencies, $\omega_S + \omega_{REF}$ and $\omega_S - \omega_{REF}$. These are then fed into a low-pass filter that has a bandwidth, BW_{LP} (usually of the order of 10's of MHz), which is close to (but smaller) than the expected linewidth of the spin-torque-driven spectral

peak. The low-pass filter then outputs a signal of frequency $|\omega_S - \omega_{RF}| < BW_{LP}$. Usually, the signal is filtered once more by a DC-block which only allows signals of frequencies >~10 kHz (the DC-block is added to reduce any DC artifacts), and the final signal has a frequency 10 kHz $< \omega_S - \omega_{REF}| < BW_{LP}$. The addition of the DC-block implies that frequencies within a few tens of kHz of the main spectral frequency are lost, but this is usually not a big deal since the linewidth is usually several orders of magnitude bigger, of the order of tens to hundreds of MHz. After filtering, the final signal is fed into a diode-detector which rectifies the signal and outputs the DC-component of the rectified signal into the DAQ card of the measurement-acquisition computer. The frequencies swept by the signal-generator are also recorded for each bin by the DAQ card and a frequency spectrum of the rectified voltage signal can thus be obtained (Figure 2.14).

Note that a low-pass filter of x MHz has a bandwidth BW_{LP} = 2x MHz. The band-width of the low-pass filter sets the resolution limit of the frequency linewidth (in other words, it sets the minimum linewidth that can be measured by the circuit), so it should always be smaller than the linewidth of the spin-torque signal. If the band-width of the low-pass filter is larger than the frequency linewidth of the spin-torque signal, it will smear out the signal and we won't get an accurate measurement of the linewidth. The BW_{LP} should also be equal to the bin-width of the frequency sweep, so the low-pass bandwidth and the number of bins in the frequency sweep should be chosen carefully. For example, at room temperature, where the linewidths are of the order of 100's of MHz, I chose a sweep range of 1-18 GHz, 170 bins, low-pass of 50 MHz (BW_{LP} = 100 MHz), bin-width of 100 MHz and a sweep-time of 20 seconds. At lower temperatures, where the linewidths of the spin-torque-signals are small, I used

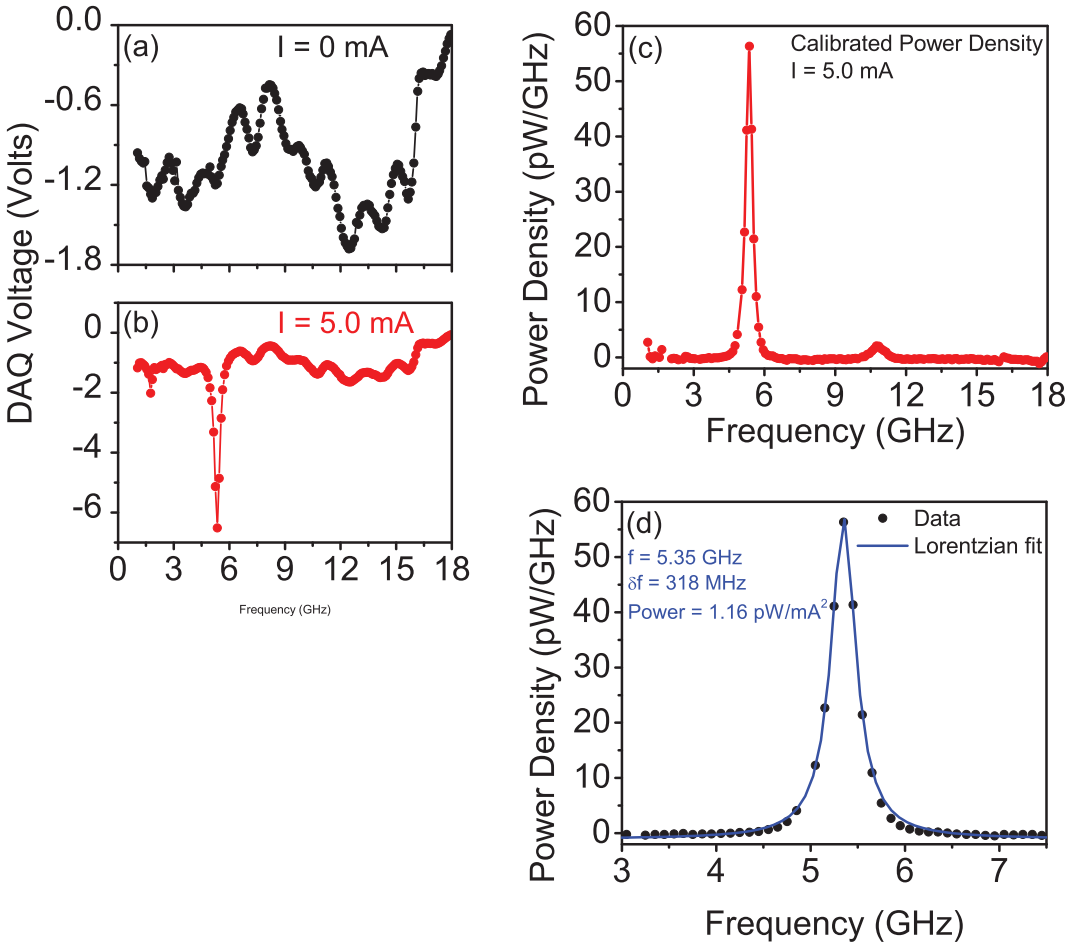


Figure 2.14: Example of (a) measured microwave-frequency spectrum at I_{DC} = 0 mA, (b) measured microwave-frequency spectrum at I_{DC} =5.0 mA showing a dynamical spectral peak, (c) calibrated power spectral density at I_{DC} =5.0 mA, and (d) Lorentzian fit to the spectral data.

a smaller BW_{LP} (1-10 MHz) and increased the number of bins accordingly for the same sweep range. Typically, a spectral peak should have at least 8-10 data points or bins.

In Figures 2.14(a) and (b), the raw frequency spectrum looks complicated with lots of bumps and dips. This is because of frequency-dependent reflections and losses through the mixer and through the line to the sample. In order to analyze the spin-torque-driven spectra at a certain I_{DC} (for example, I_{DC} = 5.0

mA in Figure 2.14(b)), we take a spectrum at 0 mA (Figure 2.14(a)) where there is no spin-transfer signal and subtract and divide it from the spectrum at I_{DC} (Figure 2.14(c)). We will explain the reason behind subtracting and dividing the spectrum by the 0 mA spectrum below. In Figure 2.14(c), we can see two main spectral peaks at $I_{DC} = 5.0$ mA; these are the first and second harmonics. We fit the peaks to a Lorentzian function (Figure 2.14(d)) and obtain the frequency, linewidth and integrated area.

Calibration Procedure

As we mentioned before, the raw frequency spectrum that we measure includes the frequency-dependent Johnson noise in the circuit, reflections due to impedance-mismatch as well as losses in the line. It is important to take these into account in order to determine the pure spin-torque signal from the sample. At I=0 mA, there is no signal due to spin-torque and the the only microwave signals are the Johnson noise from the sample and the amplifier noise. We use this fact to calibrate the frequency-dependent Johnson noise, amplifier noise and gain by taking power spectra at I=0 mA. This calibration procedure was taught to me by Jack Sankey.

In Figure 2.15, we show the important sources of impedance-mismatch and losses in the line. $\Gamma^2 = ((R_S - 50)/(R_S + 50))^2$ is the reflection due to the impedance mismatch by virtue of the sample resistance, R_S not being exactly 50Ω; α is the attenuation in the line. We will model the different sources of loss and reflections by assigning each an effective temperature and converting the temperature to a power, $k_B T \times (Bandwidth)$. Note that everything beyond the amplifiers is impedance-matched to 50Ω.

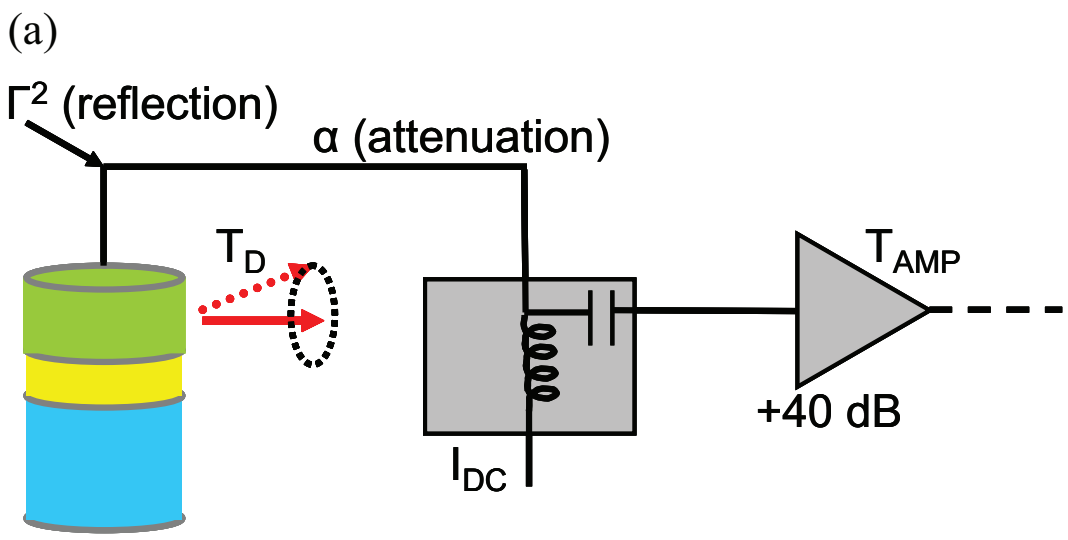


Figure 2.15: Calibration for frequency-dependent Johnson noise: sources of reflections and losses in the line.

The first contribution to the spectral power density comes from reflections in the circuit due to impedance-mismatch because of the sample not being 50Ω. The sample is at temperature T, the transmission from the mismatched load is $(1 - \Gamma^2)$ and transmission through the attenuated line is $(1 - \alpha)$.

$$P_{1-sampleresistance} = (1 - \Gamma^2)(1 - \alpha)k_B T \tag{2.6}$$

The second contribution to the power spectrum comes from the amplifiers and the amplifier noise. Assume the amplifiers are at an effective noise temperature T_{AMP}, the signal that goes from the amplifiers to the sample is proportional to $(1 - \alpha)$, reflected from the sample-mismatch (Γ^2) and travels back across the line $(1 - \alpha)$. We assume only one reflection.

$$P_{2-amplifiernoise} = \Gamma^2(1 - \alpha)^2 k_B T_{AMP} \tag{2.7}$$

The third contribution is due to attenuation of the line, which is proportional

to α and the temperature of the line, T.

$$P_{3-line} = \alpha k_B T \tag{2.8}$$

The final contribution to the power spectrum is the spin-torque-signal from the sample. We model the dynamical signal from the sample as a temperature, T_D. The contribution of this component has the same form as Equation 2.6, except that the temperature is T_D instead of the bath temperature of the sample, T.

$$P_{4-dynamics} = (1 - \Gamma^2)(1 - \alpha)k_B T_D \tag{2.9}$$

The difference between the power terms in the presence of a DC-current and the absence of a DC-current is just the fourth term due to spin-torque (Equation 2.9). The voltage that is measured at the DAQ is proportional to the frequency-dependent gain of all the amplifiers (G) and can be written in generic form as follows:

$$P(I) - P(0) = P_{4-dynamics} = (1 - \Gamma^2)(1 - \alpha)k_B T_D \tag{2.10}$$

$$V(I) - V(0) = G(P_I - P_0) = G(1 - \Gamma^2)(1 - \alpha)k_B T_D \tag{2.11}$$

$V(I)$ is the DAQ voltage spectrum in the presence of current and $V(0)$ is the DAQ voltage spectrum when $I_{DC} = 0$. The dynamical temperature, T_D, can then be written as follows:

$$T_D = \frac{V(I) - V(0)}{k_B G(1 - \alpha)(1 - \Gamma^2)} \tag{2.12}$$

We can measure the $V(I)$ and $V(0)$ spectra, and calculate Γ^2 as described previously. The only unknown frequency-dependent quantity to be determined for the calibration is $k_B G(1 - \alpha)$.

Calculating $k_B G(1-\alpha)$: In order to determine the frequency-dependent quantity, $k_B G(1 - \alpha)$, we remove the sample from the circuit and insert a 50Ω resis-

tor instead to completely impedance-match the circuit. In this case, $\Gamma^2 = 0$ and Equation 2.7 drops out. The calibration is done at $I_{DC} = 0$mA, so there is no spin-torque signal and Equation 2.9 also drops out. The only terms left are Equations 2.6 and 2.8. To determine $k_B G(1-\alpha)$, first take a spectral sweep for the 50Ω resistor at $I_{DC} = 0$mA at room-temperature, $T = T_R = 294$ K. Equation 2.10 then becomes:

$$T = T_R : V_R = G[(1-\alpha)k_B T_R + \alpha k_B T_R] \tag{2.13}$$

Then put the 50 Ohm resistor in liquid nitrogen, so that $T = T_N = 77$ K.

$$T = T_N : V_N = G[(1-\alpha)k_B T_N + \alpha k_B T_R] \tag{2.14}$$

Subtracting Equation 2.14 from Equation 2.13, we get the following:

$$V_R - V_N = k_B G(1-\alpha)(T_R - T_N) \tag{2.15}$$

Thus the frequency dependence of $k_B G(1-\alpha)$ can be determined simply by taking the difference of the voltage spectrum for a 50Ω resistor at $I_{DC} = 0$mA at room temperature and 77K.

$$k_B G(1-\alpha) = \frac{V_R - V_N}{294 - 77} \tag{2.16}$$

Now P/P_{JN} can be calculated as follows:

$$\frac{P}{P_{JN}} = \frac{k_B T_D}{k_B T_{JN}} = \frac{T_D}{294} = \frac{V_I - V_0}{294\ k_B G(1-\alpha)(1-\Gamma^2)} \tag{2.17}$$

Figure 2.14(c) shows the calibrated power density for $I_{DC} = 5.0$ mA, which is obtained from Equation 2.17 multiplied by P_{JN} (~4 pW/GHz).

Calculating Precession & Misalignment Angles

As described previously, the calibrated spectra are fit to a Lorentzian function. From the integrated area under the Lorentzian, the precession angle (θ_{max}) of the oscillating layer and misalignment angle (θ_{mis}) between the magnetic layers can be computed [6]. The derivation of these quantities will be shown below. The angle between the fixed layer magnetization, M_{FIXED}, and free layer magnetization, M_{FREE}, is time-dependent and for small oscillations, can be written as:

$$\theta(t) = \theta_{mis} + \theta_{max}\sin(\omega t) \tag{2.18}$$

Due to GMR, the resistance is also time-dependent and we can thus measure a time-dependent voltage:

$$\Delta R[\theta(t)] = \frac{\Delta R_{max}}{2}(1 - \cos[\theta(t)]) \tag{2.19}$$

$$\Delta V(t) = I\Delta R[\theta(t)] \tag{2.20}$$

Assuming small angle precession,

$$\theta(t) \ll 1 : 1 - \cos(\theta) \approx (\theta)^2/2 \tag{2.21}$$

We can obtain the following form for ΔV(t):

$$\Delta V(t) = \frac{I\ \Delta R_{max}}{4}(\theta_{mis}^2 + \frac{\theta_{max}^2}{2}) - [\frac{I\ \Delta R_{max}\theta_{max}^2}{8}]\cos(2\omega\ t) + [\frac{I\ \Delta R_{max}\theta_{mis}\theta_{max}}{2}]\sin(\omega\ t) \tag{2.22}$$

The first term in the equation is a DC-component which is filtered out. The second term has a second harmonic, 2ω and the third term has a first harmonic, ω. The power from the first and second harmonics can then be written as:

$$P_{1f} = \frac{1}{R}\langle(\frac{\Delta V_\omega}{2})^2\rangle = \frac{I^2\ \Delta R_{max}^2\ \theta_{mis}^2\ \theta_{max}^2}{32\ R} \tag{2.23}$$

$$P_{2f} = \frac{1}{R}\langle(\frac{\Delta V_{2\omega}}{2})^2\rangle = \frac{I^2\ \Delta R_{max}^2\ \theta_{max}^4}{512\ R} \tag{2.24}$$

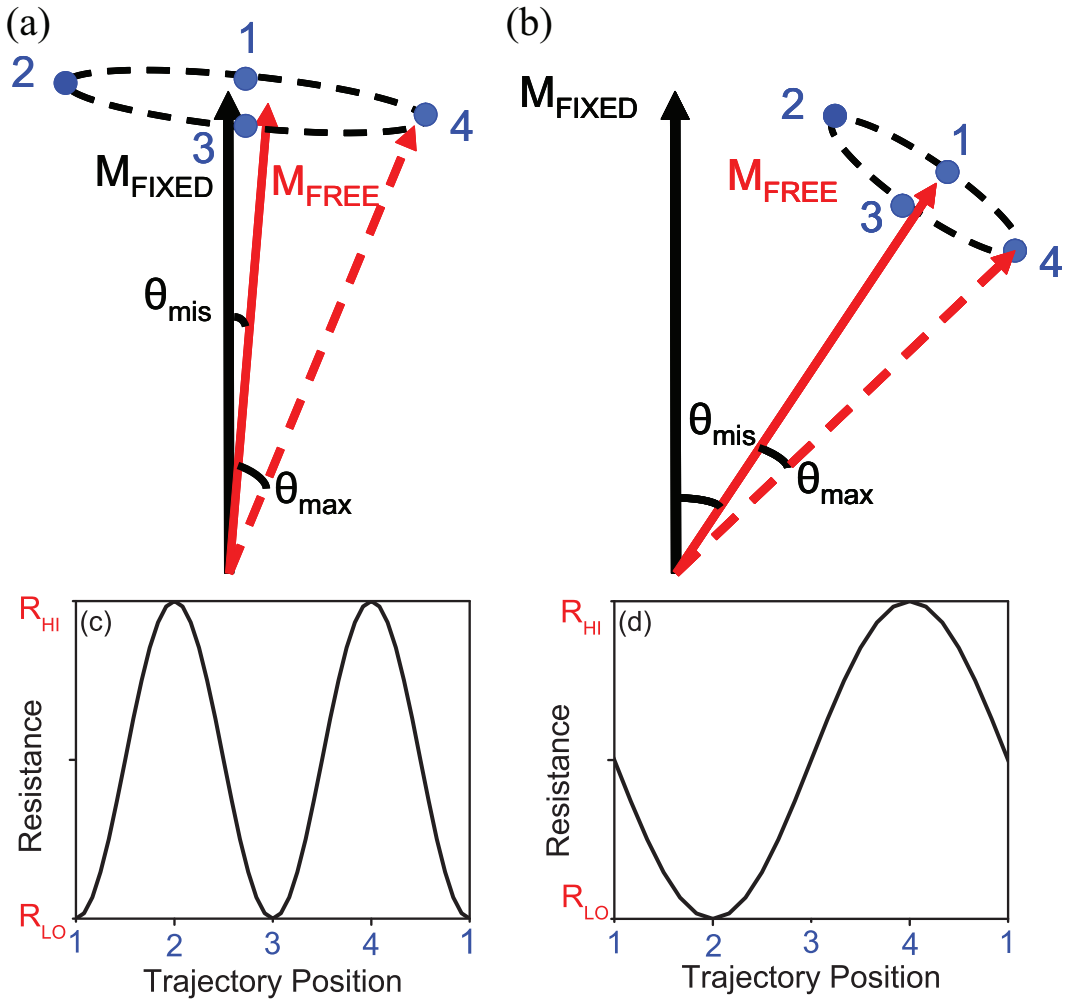


Figure 2.16: Cartoon of the misalignment angle between the layers, θ_{mis} and the precession angle of the free layer, θ_{max}. (a) Case of $\theta_{mis} < \theta_{max}$ and (b) Case of $\theta_{mis} > \theta_{max}$. (c) An intuitive picture of the resistance as a function of the trajectory position for (a), showing that the second harmonic dominates. (d) An intuitive picture of the resistance as a function of the trajectory position for (b), showing that the first harmonic also becomes important.

Thus, we can calculate θ_{max} and θ_{mis} from the integrated power of the second and first harmonics.

Intuitive understanding of 1st and 2nd harmonics

As the last 2 equations suggest, we see that when $\theta_{mis} < \theta_{max}$, the second harmonic is dominant but when θ_{mis} is large, the first harmonic becomes dominant.

We can intuitively understand this from Figure 2.16.

In Figure 2.16(a), when θ_{mis} is small and θ_{max} is large, the free-layer magnetization follows the dotted trajectory. Suppose the free-layer starts at point ”1” in the trajectory, which is the lowest resistance. As it goes to ”2”, the resistance becomes maximum, at ”3” it becomes lowest again and at ”4” it reaches a maximum. So by the time it returns to point ”1” (i.e. completes one cycle), it has gone through two maxima (Figure 2.16(c)) and hence the 2ω peak becomes dominant.

In Figure 2.16(b), when θ_{mis} is large compared to θ_{max}, we can follow the dotted trajectory again. At ”1”, the resistance is intermediate, at ”2” it is the lowest, at ”3” it is intermediate and at ”4” it is the maximum. As Figure 2.16(d) shows, the first harmonic also becomes important in this case.

2.2.3 Spin-Torque-Driven Ferromagnetic Resonance (ST-FMR) Measurements

Unlike the DC-driven dynamics discussed in Section 2.2.2, where we *apply* a DC current and *measure* an RF output, the ST-FMR technique works in the reverse way: we *apply* an RF current and *measure* a DC output [7, 8]. The ST-FMR technique at Cornell was developed by Jack Sankey and is described in References [8, 9]. In this technique, a radio-frequency (RF) current is applied across the device to excite magnetic precession (Equation 2.25) and the amplitude of the resonant motion is detected from the changing resistance of the sample (Equation 2.26). This amplitude is a DC voltage that is proportional to the mixing

signal between the RF current and the oscillating resistance (Equation 2.27).

$$I(t) = I_{DC} + I_{RF}\cos(\omega t) \tag{2.25}$$

$$R(t) = R_0 + \Delta R\cos(\omega t + \delta) \tag{2.26}$$

$$V_{DC} = I_{RF}\,\frac{\Delta R}{2}\cos(\delta) \tag{2.27}$$

A schematic of the circuit is shown in Figure 2.17. We apply the RF current to the sample from a frequency-sweeping signal generator through the AC-port of the bias-tee. The RF current from the signal generator is applied in pulses of frequency, f_{PULSE} ~1 kHz (Figure 2.17). We measure the DC mixing voltage, V_{mix} from the DC-port of the bias-tee, by a lock-in amplifier. The reference signal of the lock-in is at the same frequency as the signal-generator pulse frequency (f_{PULSE} ~1 kHz) (this is accomplished by connecting the VIDEO port of the signal-generator to the REF port of the lock-in). The output of the lock-in is read into the DAQ card to obtain the frequency spectrum of V_{mix}. The frequency-sweep time of the signal-generator should be set to about 5 × (time-constant of the lock-in) × (number of bins). For example, to sweep from 1-9 GHz with a 40 MHz bin-width, I used a time-constant of 50 msecs and a total sweep time of 50 seconds.

In order to decide the pulse-period (duration between each RF pulse) and pulse-width (how long the RF pulse is on in one period), the following procedure is generally followed: we set the signal-generator to ”CW” mode instead of ”sweep” mode, so that the signal-generator just outputs a signal of fixed frequency. We monitor the lock-in output while trying out a few different values of the pulse-period, until the fluctuations of the lock-in output are within 10-20 nVolts. Then we set the pulse-width to half the pulse-period. Then we auto-phase to make the reference pulse signal from the signal-generator in-phase

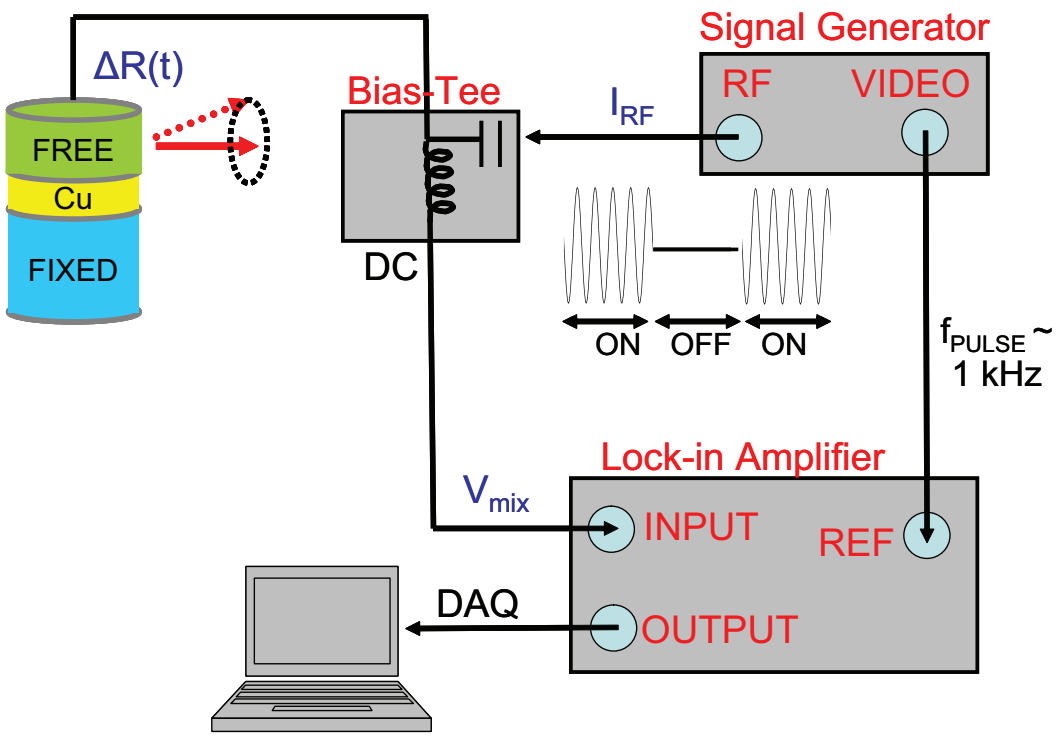


Figure 2.17: Schematic of ST-FMR circuit.

with the RF signal from the sample. Once the pulse-period and pulse-width are set, we revert to the signal generator "sweep" mode for the ST-FMR measurements.

Flatness Procedure

There is a caveat involved when an RF-current is applied from the signal-generator: the RF-power outputted by the signal-generator is not constant and is frequency-dependent (Figure 2.18(a)). In order to ensure that a constant RF-current is applied across the sample, there is a flatness calibration procedure that must be undertaken before the ST-FMR measurements. This flatness calibration should be done in the current and magnetic field regime where there

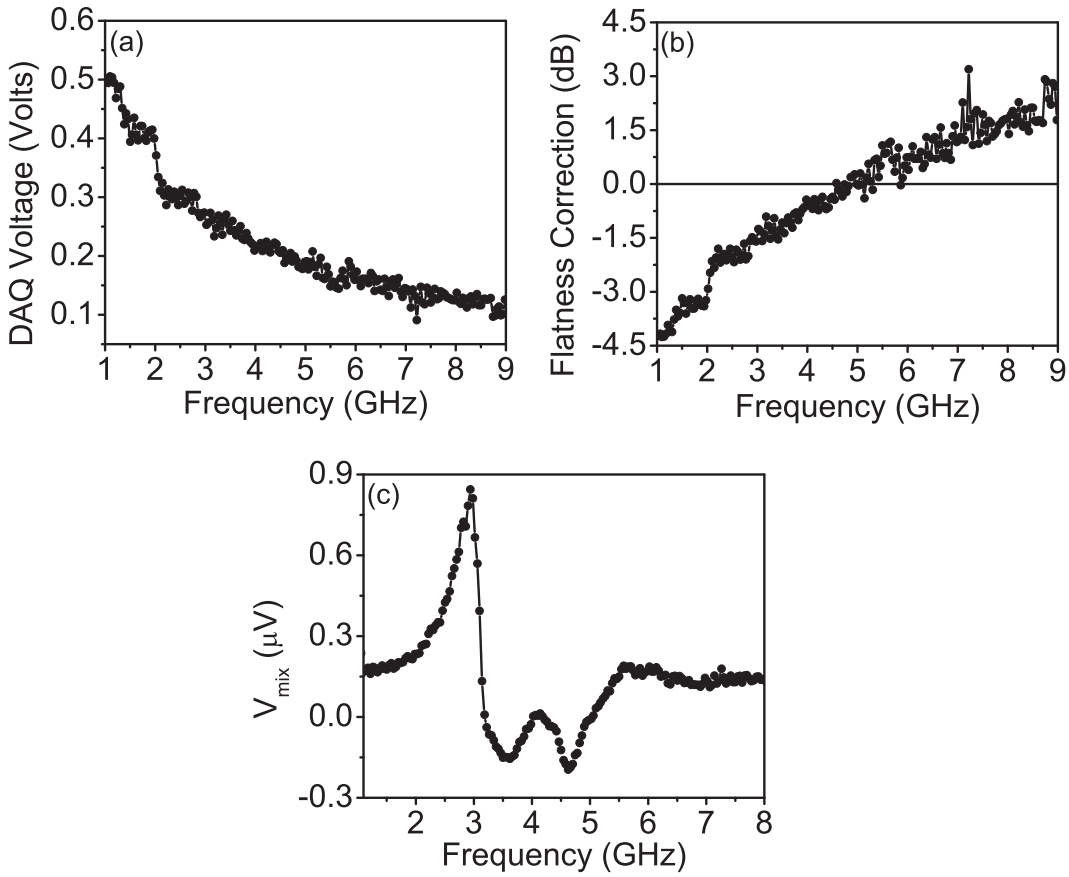


Figure 2.18: Flatness procedure for ST-FMR measurements. (a) Pre-flatness spectrum, showing the non-constant, frequency-dependent RF-power outputted from the signal-generator. (b) Flatness correction that is uploaded to the signal-generator to output a constant RF-current across the sample. (c) Example of a ST-FMR spectrum.

are no spin-torque-driven dynamics. Typically, this regime is at high magnetic fields where the misalignment angle between the magnetic layers is very small. If the layers are almost parallel, the spin-transfer-torque is close to zero and so the only output we measure from the sample is due to the reflections and losses through the line and not attributable to any magnetic signature. To do the flatness calibration, in addition to applying a large magnetic field, we apply an RF-signal (usually a value between -17 and -35 dBm) from the signal generator. We also apply a DC-current that is below the critical current for spin-transfer

but large enough to give a sufficient V_{mix} signal [the V_{mix} signal, as described below in Equation 2.28 has a background, non-frequency-dependent component that is present due to the non-linear V-I behavior of the device (first term in Equation 2.28). The DC-current that is applied for the flatness procedure should have a large slope in the dV/dI to maximize the signal]. We set the pulse-width and pulse-period as discussed previously. The flatness spectrum, V_{mix}, (Figure 2.18(a)) is converted to dB by: -10× log(V_{mix}) and adjusted (Figure 2.18(b)) so that at lower frequencies, the signal-generator *subtracts* dB and at higher frequencies, *adds* dB so that the RF-power to the sample is always constant. This flatness file is then uploaded to the signal-generator. We verify that the flatness correction has been uploaded correctly by taking a V_{mix} spectrum at the same magnetic field and I_{DC} at which the flatness spectrum was taken and check that the V_{mix} is a constant and independent of frequency.

An example of the ST-FMR spectrum is shown in Figure 2.18(c). The linewidth of the ST-FMR peak is proportional to the damping and the amplitude of the peak is roughly proportional to the magnitude of the spin-transfer torque. The amplitude is maximum when the angle between the layers is close to 90°. Usually, we fit the spectra to the sum of symmetric and anti-symmetric Lorentzians and fit for 7 parameters: offset and frequency, linewidth, amplitude of the symmetric and anti-symmetric Lorentzians. The ST-FMR spectra are analyzed by the following equation, which was derived in References [8, 9, 10].

$$\langle V_{mix} \rangle = \frac{1}{4}\frac{\partial^2 V}{\partial I^2} I_{RF}^2 + \frac{1}{2}\frac{\partial^2 V}{\partial \theta \partial I}\frac{\hbar\gamma \sin(\theta)}{4eMsV\sigma} \times I_{RF}^2 \left(\zeta_{\parallel} S(\omega) - \zeta_{\perp} \frac{\gamma(4\pi M_{eff} + H)}{\omega_R} A(\omega)\right) \quad (2.28)$$

The first term is the background DC-term; it leads to a non-zero offset in the spectrum and it arises from the non-linearity of the V-I behavior of the device (discussed above). The second term includes a combination of a symmet-

ric Lorentzian, $S(\omega) = 1/[1 + [(\omega - \omega_R)/\sigma]^2]$ and an anti-symmetric Lorentzian, $A(\omega) = [(\omega - \omega_R)/\sigma]S(\omega)$. In the above equation, $\zeta_{\parallel} = [(2e/\hbar)/\sin\theta]d\tau_{\parallel}/dI$ and $\zeta_{\perp} = [(2e/\hbar)/\sin\theta]d\tau_{\perp}/dI$ are the dimensionless differential in-plane and out-of-plane torques respectively.

The peak-shape can be intuitively understood from Figure 2.19. If the spin-torque is in-plane (as is the case in spin-valves), the symmetric component is large. This is because of the following reason: in Figure 2.19(a)-(b), we show the time-dependence of the applied I_{RF} and the resistance response. When I_{RF} is negative (time "b"), the in-plane spin torque pushes the free layer to align parallel with the fixed layer leading to the low-resistance state. When the I_{RF} is positive (time "d"), the in-plane spin-torque pushes the free layer to align anti-parallel with the fixed layer leading to the high-resistance state. Thus, the resistance response follows I_{RF}, i.e. they are in-phase: when I_{RF} is maximum, the resistance is maximum; when I_{RF} is minimum, the resistance is minimum. Consequently, the resonance curve (Figure 2.19(c)) in the frequency spectrum is a symmetric Lorentzian with a maximum at ω_R, i.e. the resonant frequency.

On the other hand, if the torque is out-of-plane (also called the "field-like" torque), the asymmetric component is large (as is the case in magnetic tunnel junctions). This is because of the following reason: in Figure 2.19(d)-(e), we show the time-dependence of the I_{RF} and the resistance response. When I_{RF} is negative or positive (time "b" and "d"), the out-of-plane spin torque pushes the free layer to go out-of-plane, leading to an intermediate resistance state. Note that the out-of-plane torque can only lead to an intermediate resistance state and not a high-resistance or low-resistance state. This is because of the strong demagnetization fields that cause the precession to be confined mostly in-plane

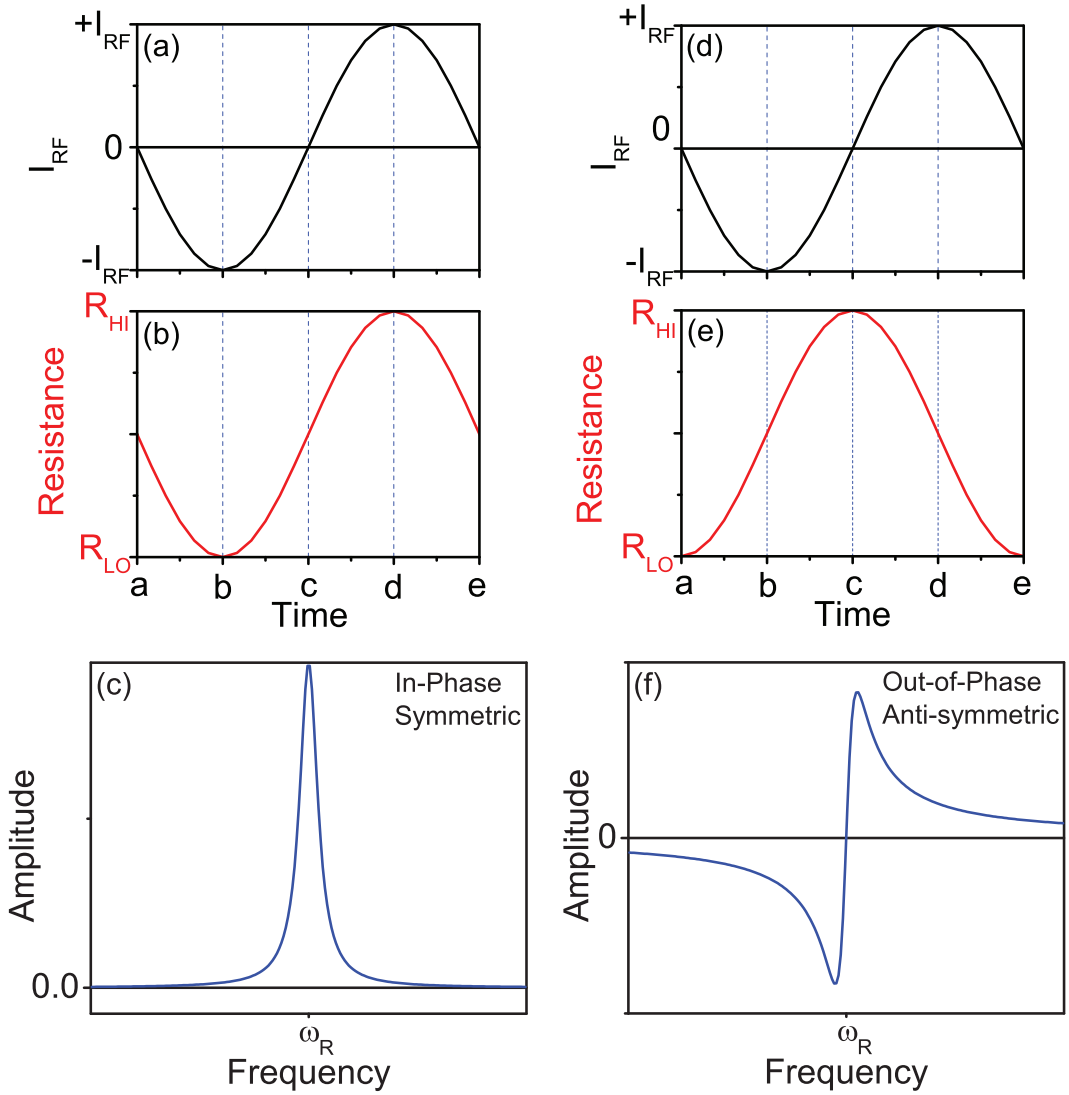


Figure 2.19: Peak shapes of the ST-FMR signal. When the (a) I_{RF} and (b) resistance are in-phase (case of in-plane torque), the peak-shape of the resonance curve is a symmetric Lorentzian with a maximum at the resonant frequency, ω_R. When the (a) I_{RF} and (b) resistance are 90° out-of-phase (case of out-of-plane torque), the peak-shape of the resonance curve is an anti-symmetric Lorentzian with a minimum at the resonant frequency, ω_R.

despite an out-of-plane torque. Therefore, when the I_{RF} is a positive or negative maximum, the resistance is intermediate and hence is 90° out-of-phase. Consequently, the resonance curve (Figure 2.19(f)) in the frequency spectrum is an anti-symmetric Lorentzian with a minimum at ω_R, i.e. the resonant frequency.

Sign of peak

In our current convention, a positive current causes the free layer amplitude to increase and the fixed layer amplitude to decrease; a negative current causes the reverse. So for a free-layer response, the sign of the ST-FMR peak is expected to be positive and for a fixed-layer response, the sign of the ST-FMR peak is expected to be negative.

Conversion from sinusoidal output to square-wave amplitude

We also need to take into account that the lock-in reference signal is sinusoidal whereas the RF output from the sample is a square-wave. This is because the signal-generator applies the RF-current to the sample in square pulses (Figure 2.17). Consequently, the lock-in mixes a square-wave signal (from the sample) with a sinusoidal signal (from the lock-in reference) and the output is hence, a sinusoidal signal. In order to obtain the correct V_{mix}, we must multiply the output of the lock-in (measured by the DAQ card) by the following conversion factor: (Lock-in sensitivity)$/10 \times \pi/\sqrt{2}$.

2.2.4 Projected Field Probe Station

We used a GMW projected field probe station (Figure 2.20) to apply magnetic fields at variable angles at room-temperature. The magnetic field is applied by coils inside the cubical black box (marker "A" in Figure 2.20). The direction of

the applied field is varied by rotating the cubical box with a motor (marker "B" in Figure 2.20). The electromagnet can apply magnetic fields as high as H = 3000 Oe.

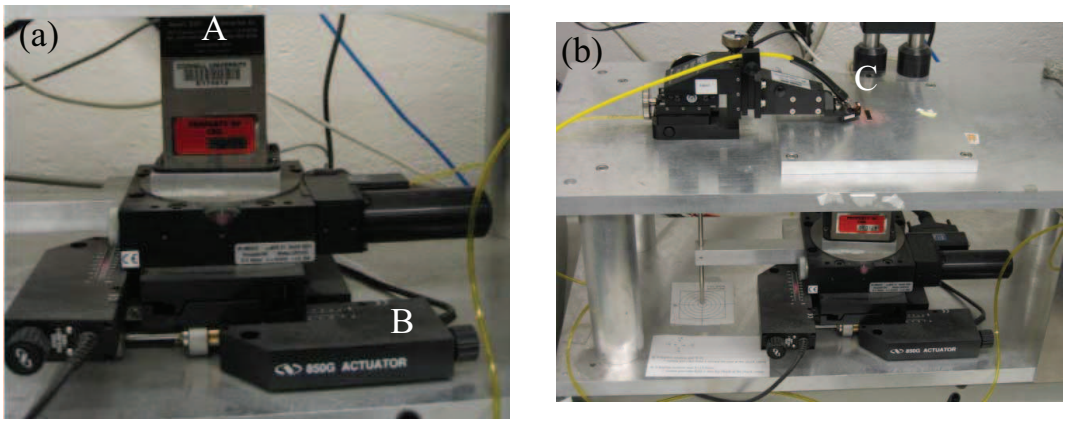


Figure 2.20: Photograph of the projected-field probe station, which can apply magnetic fields at variable field angles at room-temperature. (a) "A" is source of the magnetic field, "B" is the motor that rotates the cubical black box, thereby changing the direction of the magnetic field. (b) "C" is the probes and the sample placed near the center of the magnetic field.

2.2.5 3-D Vector Magnet

In order to do high-frequency measurements at variable magnetic field angles at low temperatures, we used the American Magnetics 3-axis vector magnet system (Figure 2.21). This system has 3 pairs of super-conducting coils, which can produce magnetic fields of upto H = 1 Tesla in-plane and H = 7 Tesla out-of-plane. In this section, we will briefly describe the operation of the system, in particular how to cool down the magnets and how to use the high-frequency dipstick for measurements.

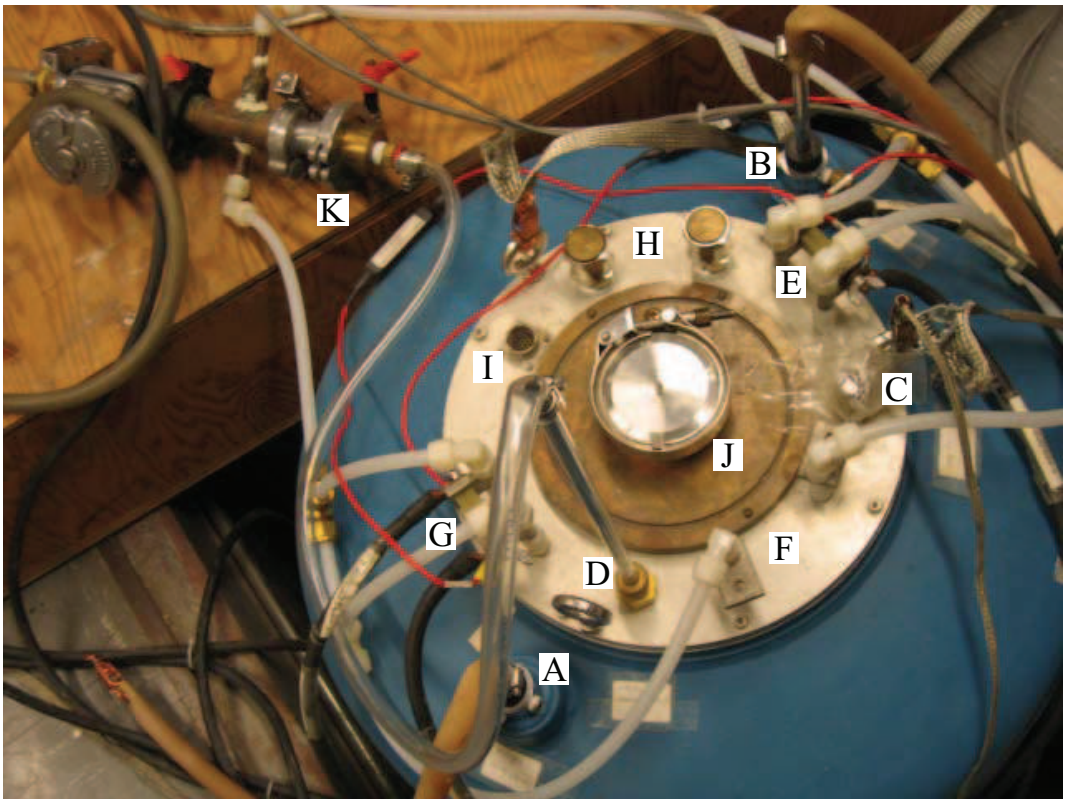


Figure 2.21: Photograph of the top-view of the 3-axis vector magnet cryostat. The blue area is the outer chamber and the silver area is the inner chamber where the 3 super-conducting coils are located.”A” is the nitrogen-release port for the outer-chamber, ”B” is the nitrogen-fill port for the outer chamber, ”C” is the helium-fill port for the inner chamber, ”D” is the helium recovery port for the inner chamber; ”E”, ”F” and ”G” are the magnet leads for the 3 pairs of coils; ”H” is the over-pressure valves, ”I” is the port for the helium level-meter, ”J” is the point through which the dipstick and sample are loaded into the system, ”K” is the helium-recovery valves that connect to the building recovery system.

Cooling down the system

Since the magnets are super-conducting, we need to cool them down to 4.2 K before we can apply any current through the coils. The system has an inner chamber and an outer chamber. The super-conducting coils are inside the inner chamber. During operation, the inner chamber is filled with helium and the outer chamber is filled with liquid nitrogen to prevent heat loss. In Figure 2.21,

the blue area is the outer chamber and the silver area near the center is the inner chamber. Marker ”B” is the nitrogen-fill port for the outer chamber and marker ”A” is the nitrogen-release port. Marker ”C” is the helium-fill port for the inner chamber and marker ”D” is the helium-recovery port for the inner chamber.

Since helium is very expensive, we usually do not transfer helium into the inner chamber right away since there would be significant boil-off in that case. Instead, we follow a pre-cooling procedure. We first cool the inner chamber with liquid nitrogen to bring the magnets from room-temperature down to 77K and then transfer helium to bring the temperature down further to 4.2 K. This procedure will be described below.

Before the pre-cooling procedure, ensure that the lid on the cryostat (marker ”J”) is firmly intact and screwed in. Also, turn off all 3 magnet power supplies (these are on a separate electronics rack, not shown in Figure 2.21).

1) *Fill inner chamber with liquid nitrogen (pre-cool inner chamber to 77K)*: We first pre-cool the inner chamber with liquid nitrogen. This is done by connecting the port designated by marker ”C” (Figure 2.21) to a nitrogen dewar and leaving the port designated by marker ”D” open to air to act as a pressure-release port. It is absolutely critical that there always be a port for pressure-release while any transfer is taking place, to prevent over-pressure that can have dire consequences. While we are transferring nitrogen, we monitor the temperature of the magnets. This is done by monitoring the resistance of the magnet leads by connecting the two leads of one of the magnets to a Keithley multimeter (markers ”E”, ”F” and ”G” show the lead-pairs of the three magnets). At room-temperature, the resistance of the magnets is about 1400Ω. As the magnets start getting colder, the resistance decreases and at 77 K, the resistance of the magnets

is about 175Ω. When the magnets are at 77K, we stop the nitrogen transfer and leave the system cold overnight.

2) *Transfer nitrogen from inner chamber to outer chamber*: Next, we need to transfer nitrogen from the inner chamber to the outer chamber so that we can then fill the inner chamber with helium. In order to push out the nitrogen from the inner chamber into the outer chamber, we connect the port marked by ″B″ to port ″C″. We connect port ″D″ to a helium gas cylinder. The helium gas pushes the liquid nitrogen from the inner chamber through port ″C″ into the outer chamber through port ″B″. We leave port ″A″ open to air and it acts as the pressure-release port during the transfer of nitrogen from the inner chamber to the outer chamber.

It is very important to ensure that all the liquid nitrogen has been removed from the inner chamber before transferring any liquid helium for the next step of the cool-down. To check if nitrogen is still being transferred from the inner chamber to the outer chamber, periodically touch the pipe connecting ports ″B″ and ″C″. If nitrogen is still flowing, the pipe will be cold. Also monitor the pipe from nitrogen release port ″A″. If nitrogen is still flowing, there will be a steady stream of pressure-release from this port.

When all the nitrogen has been transferred from the inner chamber, disconnect ports ″B″ and ″C″ from each other. Leave ports ″B″ and ″A″ open to air. Put a stopper-knob on port ″C″. Connect port ″D″ to the helium recovery system (marker ″K″) to prepare for the next step of the liquid helium transfer.

3) *Fill helium in the inner chamber (cool inner chamber to 4.2 K)*: Once all the nitrogen is transferred from the inner chamber to the outer chamber, we can

transfer liquid helium into the inner chamber to complete the cool-down to 4.2 K. In order to do this, ensure port ”D” is connected to the helium recovery line (marker ”K”) of the building. This is crucial. Next, bring the liquid helium dewar and use a transfer-tube to transfer helium from the dewar into port ”C”. While transferring helium, keep an eye on the over-pressure valves (shown by marker ”H” in Figure 2.21). If the valves pop up, decrease the transfer pressure from the helium dewar. Also, monitor the recovery gauge on the wall and note down the recovery reading. The inner chamber is usually full with helium when the recovery gauge shows an increase by 200-300 units. Also monitor the resistance of the magnet leads. The magnets are at 4.2 K and super-conducting when the lead resistance is close to 0Ω. While the helium is transferring, connect the helium level-meter to port ”I”. When the inner chamber is filled with helium, the level-meter usually shows a ”60%′ reading (it doesn't show 100% for some reason).

Once the helium is filled inside the inner chamber, remove the transfer-tube from port ”C” and plug port ”C” with a stopper-knob.

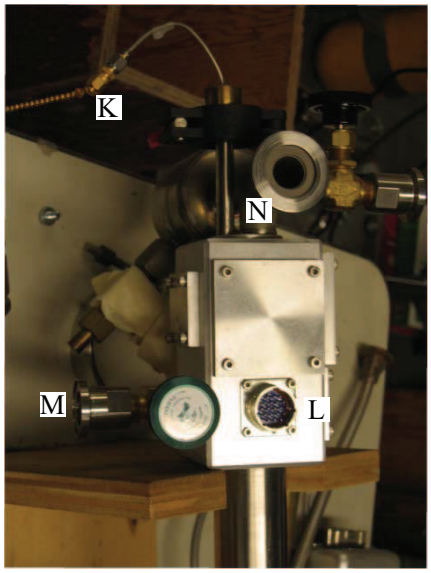
4) *Fill nitrogen in the outer chamber*: Finally, to prevent heat losses from the inner chamber, we fill the outer chamber with more nitrogen. This is done by connecting port ”B” to the nitrogen dewar and keeping port ”A” open to air to act as a pressure release. The outer chamber is filled with nitrogen when we start seeing nitrogen coming out of port ”A”.

Preparing the dipstick and sample for cooldown

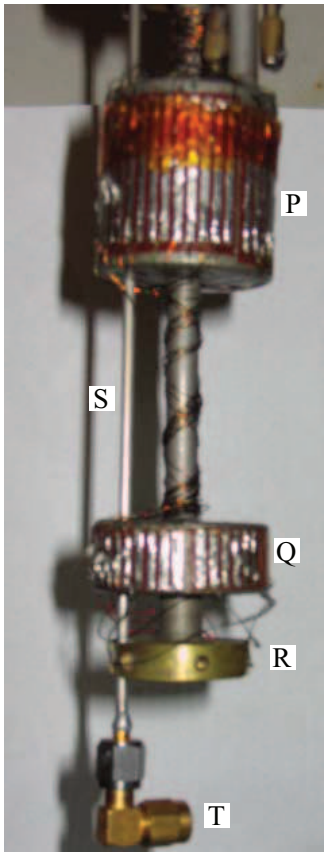
Once the system is cold, we can now prepare the sample and the high-frequency dipstick for measurements (Figure 2.22). The dipstick has a 40 GHz K-cable running from the top to the bottom (top shown by marker ”K” in Figure 2.22(a) and bottom shown by marker ”S” in Figure 2.22(b)). The devices are ribbon-bonded inside a sample-carrier (as described in Nathan Emley's thesis [3]) and the sample carrier is connected to the bottom of the cable (marker ”T” in Figure 2.22(b)). There is also a heater and temperature-sensor at the bottom (marker ”R” in Figure 2.22(b)). These are wired very delicately (markers ”P” and ”Q” in Figure 2.22(b)) to the top of the dipstick (marker ”L” in Figure 2.22(a)). Marker ”L” in Figure 2.22(a) shows the military connector point for the temperature-control of the system.

Before inserting the dipstick into the vector magnet, we have to pump down and pre-cool the sample. This procedure is described below.
1) Ribbon-bond the sample onto a sample carrier and *gently* connect the sample carrier to the bottom of the dipstick (marker ”T”). Do not use a torque-wrench, instead just tighten gently with the fingers to prevent stress to the delicate solder joint of the K-cable.
2) In order to prepare to pump-down the sample, connect ports ”M” and ”N” in Figure 2.22(a)) to a vacuum pump.
3) Put some vacuum grease around the inner circumference of the vacuum can (Figure 2.22(c)) and gently put the vacuum can over the sample at the bottom of the dipstick. Turn on the vacuum pump and wait till the vacuum can is pumped out. It is important to pump-down the vacuum can to ensure it doesn't fall into the chamber of the vector-magnet during insertion and lifting.

(a) Top of dipstick



(b) Bottom of dipstick



(c) Vacuum can



Figure 2.22: Photograph of the dipstick and sample-carrier for the 3-axis vector magnet cryostat. (a) Top of the dipstick. ″K″ is the top of the K-cable that connects the electronic measurement racks to the bottom of the dipstick to the sample. ″L″ is the military-connector port for the temperature controller and sensor. ″M″ and ″N″ are the ports through which the dipstick is pumped out to keep the vacuum can in place. (b) Bottom of the dipstick. ″P″ and ″Q″ are the electrical connections to the heater and temperature controller (″R″), ″S″ is the K-cable running from the top of the dipstick, ″T″ is the point where the sample-carrer with the ribbon-bonded sample is connected. (c) Vacuum can at the bottom of the dipstick, protecting the sample.

4) Next, insert the dipstick in a bucket of liquid nitrogen to pre-cool it to 77K. This is done to prevent helium boil-off in the vector magnet when the relatively warm dipstick is inserted. Monitor the temperature with the temperature-control unit connected to marker ”L”. When the temperature is 100 K or so, the dipstick can be inserted into the vector magnet.
5) Carefully unscrew the lid (marker ”J” in Figure 2.21) of the vector magnet and insert the dipstick into the inner chamber *very* slowly to reduce helium boiloff. Make sure the dipstick is still being pumped down by the vacuum line during insertion to prevent the vacuum can from falling off. Also make sure the sample and dipstick are grounded while inserting the dipstick into the magnet; this is done to prevent static discharge from contact with the walls of the inner chamber that can kill the sample. The sample is usually grounded by putting a grounding cap at the top of the cable (marker ”K” in Figure 2.22). Keep inserting the dipstick lower until the sample is at the center of the magnet (for the high-frequency dipstick, we have to insert the dipstick all the way till the lid touches the top of the dipstick and then we have to lift it up by 2” to make sure the sample is at the center of the magnet).

Once the dipstick is loaded inside the cryostat, disconnect the vacuum pump. Add a little bit of exchange-gas by opening the green valve on the dipstick (port ”M”) quickly for 2-3 seconds. This facilitates a speedy cool-down of the sample to 4.2K. In order to start measurements, first disconnect the helium level-meter connection (marker ”I” in Figure 2.21) BEFORE turning on the magnet power supplies. If the level-meter is still connected to the system when the power supplies are turned on, the system will quench! Also disconnect the Keithley multimeter probes and connect the magnet power supplies to the respective leads. Ensure that the helium recovery line (marker ”K”) is connected

to the recovery port "D". Turn on the magnet power supplies. Connect the dipstick to the electronics racks (marker "K") and start measurements.

2.3 Modeling: Numerical Simulations

2.3.1 Macrospin Simulations

In order to model the response of our magnetic nanopillar devices to a spin-transfer-torque, we conducted numerical simulations of the Landau-Lifshitz-Gilbert equation (LLG) for both the free and fixed layers in the macrospin approximation, where we model the magnetization of each magnetic layer as a single-spin (Equations 2.29 and 2.31).

$$\frac{d\widehat{M}_{FR}}{dt} = \gamma\,(\overrightarrow{H}_{eff,FR} \times \widehat{M}_{FR}) + \gamma\,\alpha_{FR}(\widehat{M}_{FR} \times (\overrightarrow{H}_{eff,FR} \times \widehat{M}_{FR})) \tag{2.29}$$

$$+\frac{g\,\mu_B\,\mu_0\,\eta_{FR}\,I}{2\,e\,M_{sat,FR}\,A_{FR}\,t_{FR}}(\widehat{M}_{FR} \times (\widehat{M}_{FR} \times \widehat{M}_{FX})) \tag{2.30}$$

$$\frac{d\widehat{M}_{FX}}{dt} = \gamma\,(\overrightarrow{H}_{eff,FX} \times \widehat{M}_{FX}) + \gamma\,\alpha_{FX}(\widehat{M}_{FX} \times (\overrightarrow{H}_{eff,FX} \times \widehat{M}_{FX})) \tag{2.31}$$

$$-\frac{g\,\mu_B\,\mu_0\,\eta_{FX}\,I}{2\,e\,M_{sat,FX}\,A_{FX}\,t_{FX}}(\widehat{M}_{FX} \times (\widehat{M}_{FX} \times \widehat{M}_{FR})) \tag{2.32}$$

Equation 2.29 is the LLG equation for the free layer and Equation 2.31 is the LLG equation for the fixed layer. The left-side of Equations 2.29 and 2.31 is the rate of change of magnetization, which is equal to the sum of all the torques on the magnetization. The first term on the right-side of Equations 2.29 and 2.31 is the torque due to the effective field, $\overrightarrow{H}_{eff}$. This torque causes the magnetic layers to precess about $\overrightarrow{H}_{eff}$ (Figure 2.23). The effective field is the vector sum of the applied magnetic field ($\overrightarrow{H}_{applied}$), the dipole field interaction between the

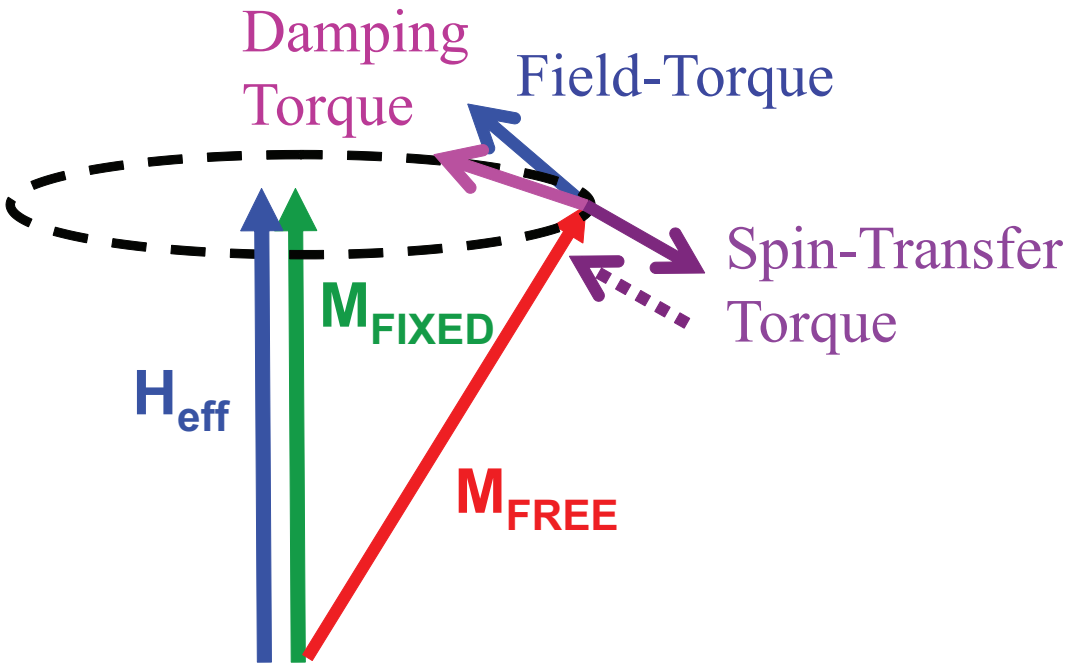


Figure 2.23: Schematic of all the torques in the Landau-Lifshitz-Gilbert equation for magnetization dynamics: Field Torque, Damping Torque and Spin-Transfer Torque. Depending on the sign of the current, the spin-transfer torque can either oppose the damping torque (solid arrow) or act in the same direction as the damping torque (dashed arrow).

layers ($\vec{H}_{dipole}$), the shape-anisotropy field ($\vec{H}_{anisotropy}$) and the exchange-bias field ($\vec{H}_{exchange-bias}$) due to an antiferromagnet.

$$\vec{H}_{eff,FR} = \vec{H}_{applied} + \vec{H}_{dipole,\ FX\ on\ FR} - \vec{H}_{anisotropy,FR} + \vec{H}_{Langevin} \quad (2.33)$$

$$\vec{H}_{eff,FX} = \vec{H}_{applied} + \vec{H}_{exchange-bias} + \vec{H}_{dipole,\ FR\ on\ FX} - \vec{H}_{anisotropy,FX} + \vec{H}_{Langevin} \quad (2.34)$$

The anisotropy field takes into account the shape-anisotropy of the sample and can be written in terms of the demagnetization factors, N_X, N_Y and N_Z.

$$\vec{H}_{anisotropy} = [N_X\ \widehat{M}_X\ M_{sat}, N_Y\ \widehat{M}_Y\ M_{sat}, N_Z\ \widehat{M}_Z\ M_{sat}] \quad (2.35)$$

The effective field also includes a Langevin field ($\vec{H}_{Langevin}$) to take into account thermal effects. Thermal fluctuations are modeled as a randomly fluctuating field with a Gaussian distribution of zero mean and standard deviation

$\sqrt{2.0\ \alpha\ k_B\ \mu_0\ \Delta t\ T/\ \gamma\ M_{sat}\ V}$, where T is the temperature and Δt is the time-step of the simulation.

The second term on the right-side of Equations 2.29 and 2.31 is the torque due to damping. This torque acts along a direction that causes the magnetic layers to eventually relax along $\vec{H}_{eff}$ (Figure 2.23). γ is the gyromagnetic ration and α is the material-dependent damping.

The third term is the torque due to spin-transfer. The magnitude of this torque depends on the misalignment between the fixed and free magnetic layers. For our simulations, we assume the torque is sinusoidal [Slonczewski [11]]. In this term, "g", "μ_B", "μ_0", and "e" are fundamental constants, η is the spin-torque efficiency (we set it to 0.2), M_{sat} is the saturation magnetization, A is the cross-sectional area of the device and 't' is the thickness of the device. Depending on the sign of the current, I, the spin-torque can either act in the same direction as the damping torque or in the opposite direction (Figure 2.23).

In the numerical simulations, we use the Huen or Runga-Kutta algorithms to integrate the LLG equation for both magnetic layers, calculate the magnetization of the fixed and free layers at each time-step and finally compute the Fast Fourier Transform (FFT) of the GMR oscillations. Each simulation usually spans 200 nanoseconds with a time-step, Δt of 1 picosecond.

We will discuss in detail the results of our macrospin simulations of the linewidths of spin-torque-driven dynamics as a function of the in-plane magnetic field angle and temperature in Sections 3.4.7 and 3.5, respectively.

2.3.2 Micromagnetic Simulations

In the previous section, we discussed simulations in the macrospin approximation by treating the magnetization of each magnetic layer as a single-spin. In micromagnetic simulations, however, instead of treating the entire magnetic layer as a single spin, we discretize the device into several smaller cells and solve the LLG equation for each cell. So unlike the macrospin single-domain calculation where the fundamental unit is the *entire* magnetic device or region, in a micromagnetic simulation, the fundamental unit is each small magnetic cell. Consequently, the magnetic behavior of the entire magnetic device is determined by the magnetic behavior of each cell and its magnetic interactions with neighboring cells.

In order to do micromagnetic simulations, we used the the micromagnetics program, OOMMF (Object Oriented Micromagnetic Framework), which was developed at NIST [12]. To illustrate how OOMMF implements the micromagnetic calculation, a sample OOMMF input file is shown below. Before we delve into the specifics of the input file, we would like to give a big picture of how the OOMMF software is organized. There are two broad classes of OOMMF software: 1) magnetic field OOMMF, and 2) current-driven spin transfer OOMMF. The first class can do calculations involving magnetic fields, while the second class can do calculations involving both magnetic field and current.

The input file in both kinds of OOMMF is a "MIF" extension file. This file contains user-written code to define the device dimensions, cell dimensions, relevant energies (such as Zeeman, exchange, demagnetization, etc.), and the desired algorithm (Energy Minimization, or the Euler Evolution of the Landau-Lifshitz-Gilbert (LLG) equation). The output from an OOMMF simulation is

of two kinds: 1) Scalar quantities, such as the average magnetization, energies, torques, etc., which are outputted into a data-table or a graph, and 2) Vector Field display, which displays these quantites at each cell and gives a spatial map of the magnetization.

Sample MIF file

```
# MIF 2.1
set pi [expr 4*atan(1.0)]
set mu0 [expr 4*$ pi*1e-7]
RandomSeed 1
Specify Oxs _ ScriptAtlas:atlas {
xrange { 0 350e-9 }
yrange { 0 160e-9 }
zrange { 0 5e-9 }
regions { ellipse }
script Ellipse
}
proc Ellipse { x y z } {
set xrad [expr 2.*$ x - 1. ]
set yrad [expr 2.*$ y - 1. ]
set test [expr $ xrad*$ xrad+$ yrad*$ yrad]
if { $ test>1.0 } { return 0 }
return 1
}
Specify Oxs_ RectangularMesh:mesh {
cellsize { 5e-9 5e-9 5e-9 }
atlas :atlas
```

```
}
Specify Oxs_ UniformExchange {
A 13e-12
}
Specify Oxs_ Demag { }
Specify Oxs_ UZeeman "
multiplier [expr 0.001/$ mu0]
Hrange {
{ 0 0 1000 0 0 0 5 }
}
"
Specify Oxs_ EulerEvolve {
alpha 0.5
start_ dm 0.01
}
Specify Oxs_ TimeDriver {
basename evolveM
vector_ field_ output_ format { text .17g }
evolver Oxs_ EulerEvolve
stopping_ dm_ dt 0.01
mesh :mesh
stage_ iteration_ limit 0
total_ iteration_ limit 0
Ms { Oxs_ AtlasScalarField {
atlas :atlas
default_ value 0.0
```

```
values {
ellipse 8e5
}
} }
m0 { Oxs_ AtlasVectorField {
atlas :atlas
norm 1
default_ value { 1 0 0 }
values { ellipse { 1 0 0 } }
} } }
```

The above "MIF" can be divided as follows:

The "**Specify Oxs_ ScriptAtlas:atlas**" line defines the dimensions of the magnetic region. The dimensions, for this example, are a $(350 \times 160 \times 5)$ nm^3 rectangle. Since we need the magnetic region to be an ellipse, we wrote a script to consider only those points on this rectangle that satisfied the equation of an ellipse $(2x-1)^2+(2y-1)^2 \leq 1$, for an ellipse centered at $(1/2, 1/2)$ to be considered as the magnetic region.

The "**Specify Oxs_ RectangularMesh:mesh**" defines the dimensions of each magnetic cell. The dimensions, for this example, are a $(5 \times 5 \times 5)$ nm^3 cube. Thus, in this example, there are 2240 cells in the magnetic region.

The "**Specify Oxs_ UniformExchange**" and "**Specify Oxs_ Demag** " define the exchange energy between neighboring cells and the demagnetization energy, respectively.

The "**Specify Oxs_ UZeeman**" defines the magnitude and direction of the external magnetic field. At each specified magnetic field, the program calculates the LLG equation (Equation 2.29) for each cell and determines the magnetic characteristics of the device.

The "**Specify Oxs_ EulerEvolve**" and "**Specify Oxs_ TimeDriver**" define the conditions, such as damping ("alpha") and maximum initial angle of the spins ("start_ dm"), for solving the LLG equation by the Euler algorithm.

The OOMMF program calculates the equilibrium magnetization, M, for each cell, by iteratively solving dM/dt for each cell. It keeps iterating this calculation until a 'stopping criteria' is reached. The stopping criteria can be either the value of the torque (dM/dt), or the amount of simulation time elapsed, or the number of iterations. For studying the steady state magnetization, the stopping criteria is usually specified by "stopping_ dm_ dt=0.000001", which asks the evolver to keep solving for the magnetization, M, until the torque, dM/dt, at all cells is very close to zero. For studying magnetization dynamics, the stopping criteria is usually specified by "stopping_ time=x", where "x" is the desired time until when it should keep solving.

Micromagnetic simulations for Section 3.4.8

The micromagnetic simulations in Section 3.4.8 were done by the same procedure described above, except that they also included a spin-torque term. These simulations were done in collaboration with Giovanni Finocchio at the University of Messina, using the algorithms described in [13].

Calculating Spectral Density from Micromagnetics FFT's

The spectral density from the micromagnetics simulations can be calculated in 2

ways. In these simulations, the magnetization $M(R_i, t_j)$ is recorded for each cell, R_i at every time step t_j.

1) One way to obtain the spectral density is to compute the FFT for the GMR oscillations of each cell, $S[R_i](f)$, then calculate the power for each cell by $|S[R_i)](f)|^2$ and finally compute the total power by summing over the power in all the cells, $P \alpha \sum |S[R_i](f)|^2$.

2) Another way to obtain the spectral density is to compute the FFT for the *average* GMR oscillations of all the cells.

$$P = \frac{I^2 \Delta R_{max}^2 |S(f)|^2 \Delta t}{R N} \tag{2.36}$$

$$S(f) = FFT(gmr(t)) \tag{2.37}$$

$$gmr(t) = \frac{1 - M_{FIXED}.M_{FREE}}{2} \tag{2.38}$$

In Section 3.4.8, I calculated the spectral density by the second method.

REFERENCES

[1] Katine J.A., Albert F.J., Buhrman R.A., Myers E.B., & Ralph D.C., Current-driven magnetization reversal and spin-wave excitations in co/cu/co pillars, *Phys. Rev. Lett.* **84**, 3149 (2000).

[2] Albert F., *The fabrication and measurement of current perpendicular to the plane magnetic nanostructures for the study of the spin-transfer effect*, Ph.d., Cornell University (2003).

[3] Emley N.C., *Magnetic Multilayer Nanopillars for the Study of Current-Induced Reversal of a Thin Magnetic Layer*, Ph.d., Cornell University (2005).

[4] Ozatay O., *Spin dependent transport and spin transfer in nanoconstrictions and current confined nanomagnets*, Ph.d., Cornell University (2007).

[5] Braganca P.M., *Material and Structural Enhancements to Spin-Transfer Phenomena in Nanopillar Spin-Valve Devices*, Ph.d., Cornell University (2008).

[6] Kiselev S.I., Sankey J.C., Krivorotov I.N., Emley N.C., Schoelkopf R.J., Buhrman R.A., & Ralph D.C., Microwave oscillations of a nanomagnet driven by a spin-polarized current, *Nature* **425**, 380 (2003).

[7] Tulapurkar A.A., Suzuki Y., Fukushima A., Kubota H., Maehara H., Tsunekawa K., Djayaprawira D.D., Watanabe N., & Yuasa S., Spin-torque diode effect in magnetic tunnel junctions, *Nature* **438**, 339 (2005).

[8] Sankey J.C., Braganca P.M., Garcia A.G.F., Krivorotov I.N., Buhrman R.A., & Ralph D.C., Spin-transfer-driven ferromagnetic resonance of individual nanomagnets, *Phys. Rev. Lett.* **96**, 227601 (2006).

[9] Sankey J.C., Cui Y.T., Sun J.Z., Slonczewski J.C., Buhrman R.A., & Ralph D.C., Measurement of the spin-transfer-torque vector in magnetic tunnel junctions, *Nature Physics* **4**, 67 (2008).

[10] Wang C., Cui Y.T., Sun J.Z., Katine J.A., Buhrman R.A., & Ralph D.C., Bias and angular dependence of spin-transfer torque in magnetic tunnel junctions, *Phys. Rev. B* **79**, 224416 (2009).

[11] Slonczewski J.C., Currents and torques in metallic magnetic multilayers, *J. Magn. Magn. Mater.* **247**, 324 (2002).

[12] http://math.nist.gov/oommf/doc/userguide12a3/userguide/.

[13] Finocchio G., Krivorotov I.N., Torres L., Buhrman R.A., Ralph D.C., & Azzerboni B., Magnetization reversal driven by spin-polarized current in exchange-biased nanoscale spin valves, *Phys. Rev. B* **76**, 174408 (2007).

CHAPTER 3

LINEWIDTHS OF SPIN-TORQUE-DRIVEN OSCILLATIONS AS A FUNCTION OF IN-PLANE MAGNETIC FIELD ANGLE & TEMPERATURE

3.1 Previous Studies of Spin-Torque Oscillator Linewidths

In a magnetic multilayer device, spin-transfer torque from a spin-polarized direct current can excite steady-state magnetic precession [1, 2], thereby creating a nanoscale frequency-tunable microwave source [3, 4, 5, 6, 7, 8, 9, 10, 11, 12, 13, 14, 15, 16, 17]. Such nano-oscillators have been studied previously in two device geometries: nanopillars in which the precession occurs in a finite disk of magnetic material [3, 5, 6, 8, 9, 12, 13, 14, 16, 17], and point contact devices in which precession is excited within a small region that is part of a larger-area magnetic thin film [4, 7, 10, 11, 15]. For applications, it is desirable that the microwave signal has a frequency spectrum with a narrow linewidth at room temperature. For this reason, understanding what physical processes affect the linewidth has generated considerable interest, both theoretically [18, 19, 20, 21, 22, 23, 24] and experimentally [12, 13, 5, 6, 7, 9, 15, 25, 26, 27, 28, 29]. Experiments have been done to explore the linewidth dependence on temperature [12, 13] and on magnetic fields which rotate the precession axis out of the sample plane [5, 6, 7, 9, 15].

3.1.1 Putting Our Work in Perspective

In this chapter, we will report measurements and simulations of DC-driven precession which show a surprisingly strong dependence of this linewidth on the in-plane angle of applied magnetic field. We find that the most-commonly stud-

ied field orientation, in-plane and parallel to the magnetic easy axis, produces the broadest linewidths. As the field angle is rotated towards the in-plane hard axis, the linewidths decrease dramatically, by more than a factor of 20 in some devices. Comparisons with micromagnetic simulations suggest that this change is due to a crossover from spatially incoherent to coherent dynamics.

3.2 What do Linewidths Mean?

In this chapter, we will discuss the linewidths of the spectra of resistance oscillations excited by a direct (DC) spin-polarized current. It is important to note that the mechanisms governing the linewidth of DC-driven precession differ from the physics of the linewidth in ferromagnetic resonance (FMR) experiments excited by oscillatory drives. While the linewidth in an FMR experiment is determined directly by the magnetic damping coefficient and hence by relaxation mechanisms, the linewidth of DC-driven auto-oscillations is an entirely different physical quantity that is not directly related to relaxation. Instead, the linewidth of DC-driven precession measures any lack of perfect periodicity in the resistance oscillations, which can be caused by thermal fluctuations or chaotic dynamics, but not directly by damping. To illustrate the distinction between the two types of measurements, at zero temperature in the absence of any chaos the linewidth for DC-driven precession should presumably go to zero, while the linewidth of an FMR experiment would still be nonzero and given by the damping coefficient. Both types of linewidth have been measured in the same sample, and they can differ by more than a factor of ten, for instance in [30] the FMR linewidth was 240 MHz and the DC-driven linewidth was 13 MHz for the same values of magnetic field and temperature).

3.3 Important Mechanisms and Mathematical Models for Linewidths

In this section, we will discuss some important mechanisms and models for linewidths. The linewidths of spin-torque-driven oscillations can be affected by amplitude and phase fluctuations, thermally-activated hopping between different dynamical modes, or spatial incoherence.

3.3.1 Amplitude and Phase Fluctuations in a Non-Linear Auto-Oscillator

Before we discuss the contribution of amplitude and phase fluctuations to the linewidth, we will briefly discuss what these fluctuations mean. These fluctuations are caused by thermal effects. Thermal effects can act either *perpendicular* (radial) to the trajectory or *along* (tangential) the trajectory of the oscillation.

Amplitude fluctuations

If thermal effects act *perpendicular* to the trajectory (i.e. radially), they lead to fluctuations of the precession angle or amplitude (Figure 3.1). The amplitude fluctuations can be described by an *amplitude correlation time*. The amplitude correlation time is the time over which the precessing magnetization loses memory of its initial starting trajectory. As time goes on, the magnetization becomes less and less correlated with the state it started out in, i.e. $\langle(\theta(0)-\bar{\theta})(\theta(t)-\bar{\theta})\rangle$ decreases exponentially (θ is the precession angle or amplitude). However, regardless of

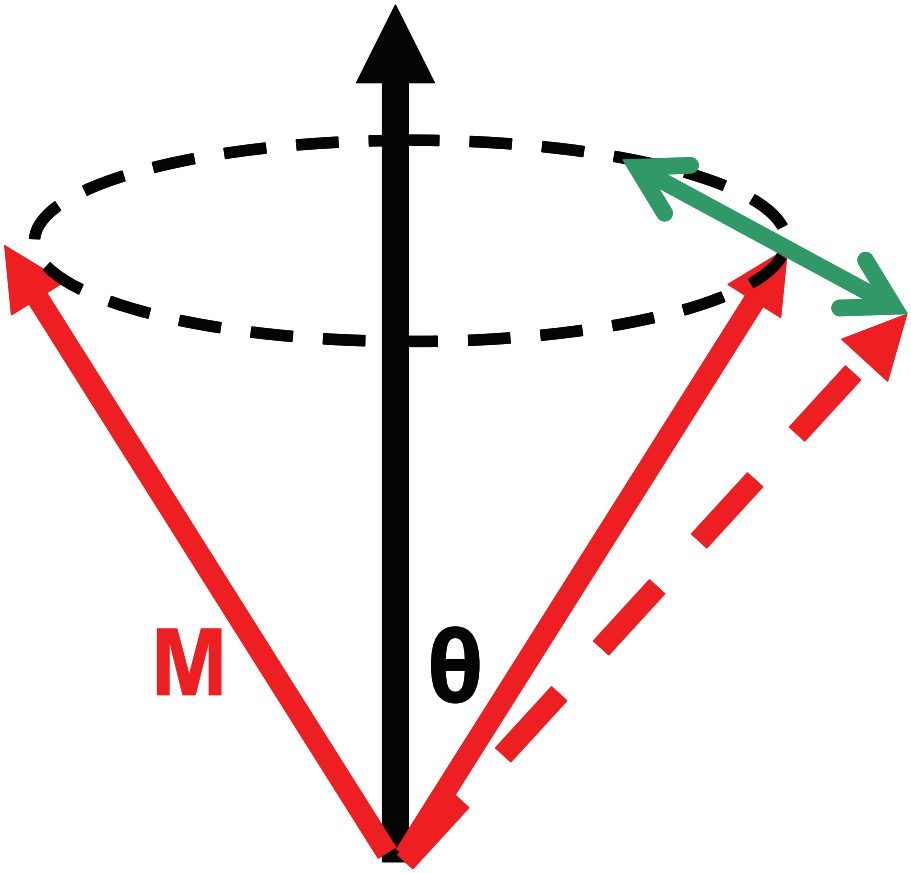


Figure 3.1: Illustration of Amplitude Fluctuations. Thermal effects acting perpendicular to the trajectory cause a spread in the precession angle or amplitude.

the starting point, the magnetization will ultimately tend to settle into some steady-state trajectory (while continuing to fluctuate). At T=0, the amplitude correlation time is also equal to the amount of time it takes the magnetization to return to its equilibrium trajectory. At higher temperatures, the amplitude correlation time is the time after which the fluctuations completely randomize. The amplitude correlation time is inversely proportional to the damping rate (Γ_P): if the amplitude correlation time is large, the damping rate of amplitude fluctuations is small.

Phase Fluctuations

If thermal effects act *along* the trajectory, they will lead to a spread in the time it takes to complete every orbit, by making the magnetization precess faster or slower. In order to understand how phase fluctuations lead to broadening of the linewidth, we consider an example of an ensemble of N different oscillators. We borrowed this example from Reference [31]. Suppose at time t=0, all the oscillators are in phase and they all complete their respective orbits at the same time (Figure 3.2(a)). In this case, the time-domain signal of all the oscillators is identical and the ensemble signal looks identical to the signal of any one oscillator (Figure 3.2(b)). In this case, the probability distribution of the phase P(ϕ,t) is just a delta function at a phase of zero (Figure 3.2(c)), since all the oscillators in the ensemble are at the same phase. As time goes on, the oscillators start going out of phase relative to each other, leading some oscillators to complete the orbit faster than others (Figure 3.2(a)). This leads to a spread in the time-domain signal (Figure 3.2(b)) and a broad phase probability distribution (Figure 3.2(c)). The width of the probability distribution, $\langle \phi^2(t) \rangle$, is proportional to the phase diffusion constant (D), which is a measure of how fast the phase diffusion occurs.

It should be noted that in this example, we tried to elucidate the role of phase fluctuations by considering an ensemble of different oscillators. For a single oscillator, the phase fluctuations will manifest themselves into the linewidth in the same way: instead of thinking of an ensemble of different oscillators with different phases, the analog for a single oscillator would be the different periods of its orbital trajectory due to phase fluctuations.

The phase fluctuations can be described by a *phase coherence* time. The co-

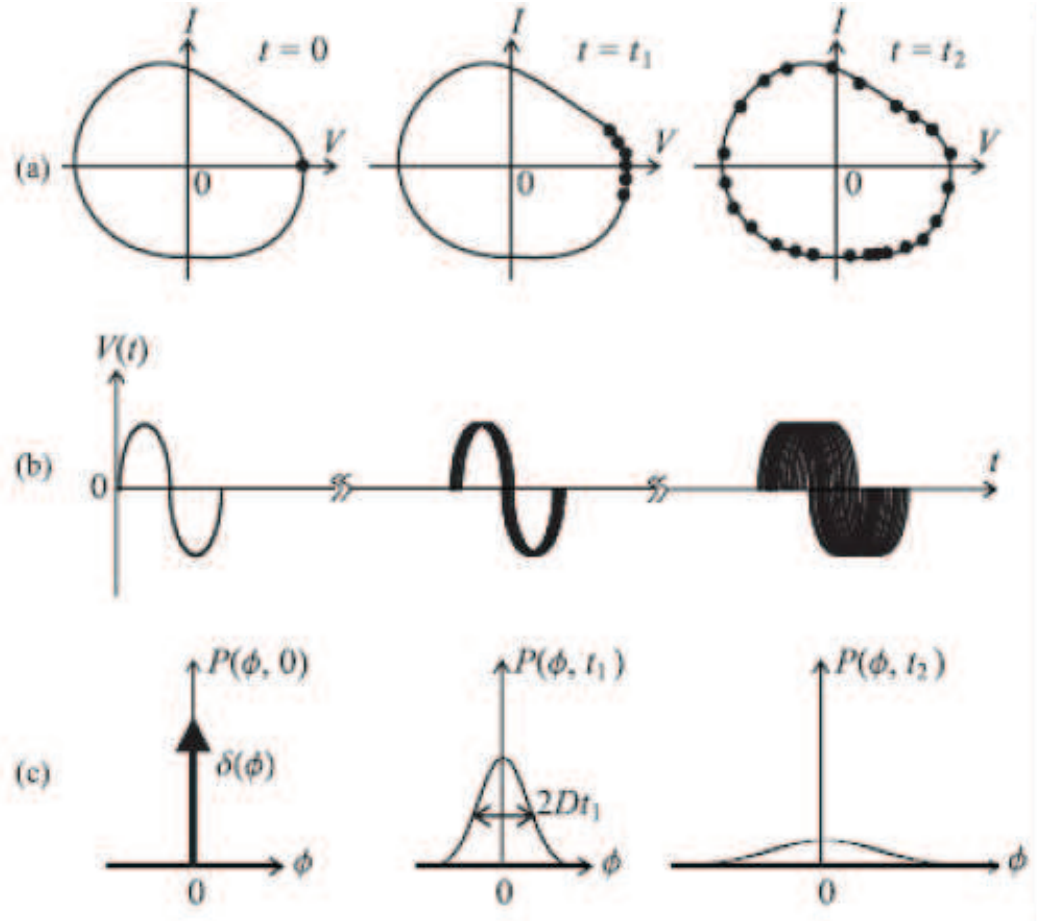


Figure 3.2: Illustration of Phase Fluctuations. Thermal effects acting along the trajectory cause a spread in the time it takes to complete every orbit. Taking the example of an ensemble of N oscillators, at t=0, all the oscillators are in phase and they all complete their orbits in the same time. Thus, the time-domain signal of the ensemble is just the same as the time-domain signal of any one oscillator. This gives rise to a delta function in the probability distribution of the phase. As time goes on, the oscillators go out of phase and there is a spread in the time-domain signal for the ensemble, leading to a finite distribution of the phase probability. The width of the distribution is proportional to the rate of phase diffusion. Figure from [31].

herence time is the time over which the phase is coherent or predictable. It is inversely proportional to the linewidth ($\Delta\omega$).

Distinction between Linear and Non-Linear Auto-Oscillators

In a linear auto-oscillator, the precession frequency does not depend on the amplitude. Thus, amplitude fluctuations do not affect the frequency and therefore, do not affect how long it takes to complete a trajectory (i.e. the phase is unaffected). In other words, in a linear auto-oscillator, the amplitude and phase fluctuations are decoupled from each other and act independently.

Typically, amplitude fluctuations cannot keep increasing boundlessly since the magnetization will ultimately tend to settle down towards its steady-state trajectory. However, phase fluctuations have no restoring force to revert the phase to its original value and so they can keep increasing without any bounds.

On the other hand, in a non-linear auto-oscillator, the precession frequency depends on the amplitude. Thus amplitude fluctuations lead to different precession frequencies, which in turn affect how long it takes to complete a trajectory, thereby leading to phase noise. Thus, in a non-linear oscillator, the amplitude and phase noise fluctuations are coupled.

Linewidths of Linear & Non-linear Auto-Oscillators

The amplitude and phase fluctuations in a non-linear oscillator have been incorporated in a theory developed by Prof. Andrei Slavin's group at Oakland University [19, 20, 32, 33]. They published a nice review of this theory in Refer-

ence [34]. We will briefly discuss it here.

The power spectrum of an auto-oscillator in the presence of thermal noise is given by [32]:

$$S(\Omega) = \int d\tau \kappa(\tau) e^{i\Omega\tau}. \tag{3.1}$$

Here, $\kappa(\tau)$ is the correlation function of the oscillator variable c(t),

$$\kappa(\tau) = \langle c(t+\tau)c^*(t))\rangle, \tag{3.2}$$

where $c = |c|exp(i\phi)$, $|c|$ is the amplitude and ϕ is the phase of the oscillation. The power of the oscillations is $p = |c|^2$. In the regime where phase fluctuations dominate, the autocorrelation function corresponding to the phase noise contributions can be written as [32]:

$$\kappa(\tau) = p_0\langle exp(i[\phi(t) - \phi(0)])\rangle = p_0 e^{i\langle\phi(t)-\phi(0)\rangle}\, exp[-\Delta\phi^2(t)/2] \tag{3.3}$$

The variance of the phase fluctuations, $\Delta\phi^2$ is given by:

$$\Delta\phi^2 = \langle\phi^2(t)\rangle - [\langle\phi(t)\rangle]^2 = \frac{D(p_0)}{p_0}\, t = \frac{\Gamma_+(p_0)\,\eta(p_0)}{p_0}\;\; t \tag{3.4}$$

Here "t" is the time, $D(p_0)$ is the diffusion coefficient that characterizes how fast the phase diffusion occurs. $D(p_0) = \Gamma_+(p_0)\,\eta(p_0)$, where p_0 is the steady-state oscillation power, $\Gamma_+(p) = \Gamma_0(1 + Qp)$. Γ_0 is the linear Gilbert damping constant and Q is the non-linear damping coefficient. $\eta(p_0)$ is the noise power. From Equation 3.4, we see that the variance $\Delta\phi^2$ for an auto-oscillator varies linearly with time. However, as we will discuss below, this is only true for the case of a linear auto-oscillator. The linewidth of a linear auto-oscillator is then given by:

$$2\Delta\omega_0 = \frac{\Delta\phi^2}{t} = \Gamma_+(p_0)\frac{\eta(p_0)}{p_0}, \tag{3.5}$$

The ratio $\eta(p_0)/p_0$ is the ratio of the noise power to the oscillation power, which can also be re-written as a ratio of corresponding energies, $k_BT/E(p_0)$. So the

linewidth of the linear oscillator can be written as:

$$2\Delta\omega_0 = \Gamma_+(p_0)\frac{k_B T}{E(p_0)}, \tag{3.6}$$

where E is the energy of the oscillations that depends on the amplitude, p.

Case of a non-linear auto-oscillator: In a non-linear oscillator, the precession frequency depends on the oscillation amplitude and this gives rise to a non-linear shift in the frequency: $\omega[p(t)] = \omega[p(0)] + N\ \delta p$. This non-linear frequency shift, $N\ \delta p$, leads to a coupling between the amplitude and phase fluctuations (discussed above) and it acts as an additional noise source, leading to a broadening of the oscillator linewidth. Tiberkevich and Slavin calculated the variance $\Delta\phi^2$ after including the extra noise term, i.e. the non-linear frequency shift, $N\ \delta p$:

$$\Delta\phi^2 = 2\ \Delta\omega_0 \left[(1+\nu^2)\ t - \nu^2 \frac{1 - e^{-2\Gamma_P |t|}}{2\Gamma_P} \right], \tag{3.7}$$

where $\Delta\omega_0$ is the generation linewidth of a linear oscillator (Equation 3.6), $\nu = N/\Gamma_{eff}$ is the normalized non-linear frequency shift coefficient, $N = d\omega/dp$ is the rate at which STO frequency changes with STO power and Γ_{eff} is the rate at which the effective damping changes with the STO power. $\Gamma_{eff} = \partial_p(\Gamma_+ - \Gamma_-)$, where Γ_+ is the non-linear effective damping term discussed above. Γ_- is the spin-torque term, proportional to the current.

It should be noted that for the case of a linear oscillator, $\nu = 0$ and Equation 3.7 reduces to Equation 3.4. For the case of a non-linear oscillator, we see that the variance (Equation 3.7) does not vary linearly with time as it did for the linear oscillator case (Equation 3.4). This is due to the additional non-linear noise term $N\ \delta p$. For the non-linear case, the variance grows linearly with time only at time intervals larger than the amplitude correlation time ($1/\Gamma_P$).

From the variance (Equation 3.7), Tiberkevich and Slavin have calculated the linewidth of the non-linear oscillator in two different regimes, depending on whether the coherence time of phase fluctuations is larger (low temperatures) or smaller (high temperatures) than the correlation time of amplitude fluctuations [32]. As the temperature increases, the phase coherence time decreases, i.e. the rate at which it loses phase ($\Delta\omega$, or linewidth) increases.

Low temperature limit

When the phase coherence time ($1/\Delta\omega$) is larger than the amplitude correlation time ($1/\Gamma_P$), i.e. $\Delta\omega \ll \Gamma_P$, the exponential factor in the variance (Equation 3.7) can be neglected and the linewidth becomes:

$$2\Delta\omega_{LOW_TEMP} = 2\Delta\omega_0(1+\nu^2) = \Gamma_+(p_0)\frac{k_B T}{E(p_0)}(1+\nu^2) \tag{3.8}$$

Thus, in the low temperature limit, the linewidth increases by a factor of $(1+\nu^2)$ relative to the linear oscillator (Equation 3.6). In this regime, the linewidth increases linearly with temperature and the power spectrum is a Lorentzian. Tiberkevich and Slavin describe the low-temperature limit by:

$$k_B\, T \ll \left(\frac{\Gamma_P}{\Gamma_+}\right)\frac{E(p_0)}{(1+\nu^2)} \tag{3.9}$$

High temperature limit

When the phase coherence time ($1/\Delta\omega$) is smaller than the amplitude correlation time ($1/\Gamma_P$), i.e. i.e. $\Delta\omega \gg \Gamma_P$, the exponential function in the variance (Equation 3.7) can be expanded into Taylor series and the linewidth becomes:

$$\Delta\omega_{HI_TEMP} = |\nu|\sqrt{\Gamma_+\Gamma_P}\sqrt{\frac{k_B T}{E(p_0)}} \tag{3.10}$$

Thus, in the high temperature limit, the linewidth is proportional to $T^{1/2}$. They also calculated the power spectrum to be a Gaussian in this regime.

In Figure 3.3(a), we show Tiberkevich and Slavin's calculations of the linewidths as a function of temperature. When the non-linearity, ν, is 0 (i.e. linear oscillator), the linewidth is linearly proportional to T at all temperatures. As the non-linearity, ν increases, the temperature range over which the linear temperature dependence occurs decreases. Eventually, at very high non-linearity, the temperature dependence becomes square-root even at low temperatures. Figure 3.3(b)-(c) shows that for small non-linearity, the linewidth varies as T, while for large non-linearity, the linewidth varies as $\sqrt{T}$.

Regarding Sankey's $T^{1/2}$ dependence

In [12], Sankey et al. found that the linewidth varies as $\sqrt{T}$ for linewidths calculated from integrating the Landau-Lifshitz-Gilbert equation. They did not observe a linear temperature dependence, as predicted by Tiberkevich and Slavin. We speculate that this may be for the following reason. Sankey et al.'s $\sqrt{T}$ dependence corresponds to a highly non-linear case of the theory of Tiberkevich and Slavin (Figure 3.3(c)), i.e. a large $\nu = N/\Gamma_{eff}$. Tiberkevich and Slavin assume a large non-linear damping coefficient, Q, in their calculations while Sankey et al. assumed Q = 0 and only took into account a constant Gilbert damping. Thus, the non-linear damping, Γ_p of Tiberkevich and Slavin is higher than for Sankey et al., implying that their relaxation rate toward the equilibrium orbit is higher (or correlation time is smaller), leading to the cross-over temperature from linear-T dependence to $\sqrt{T}$ dependence being higher (because need to go to even higher temperatures before $\Delta\omega$ becomes larger than the large Γ_P) (Equation 3.9).

Sankey et al. assumed that the magnetic dynamics are governed by the

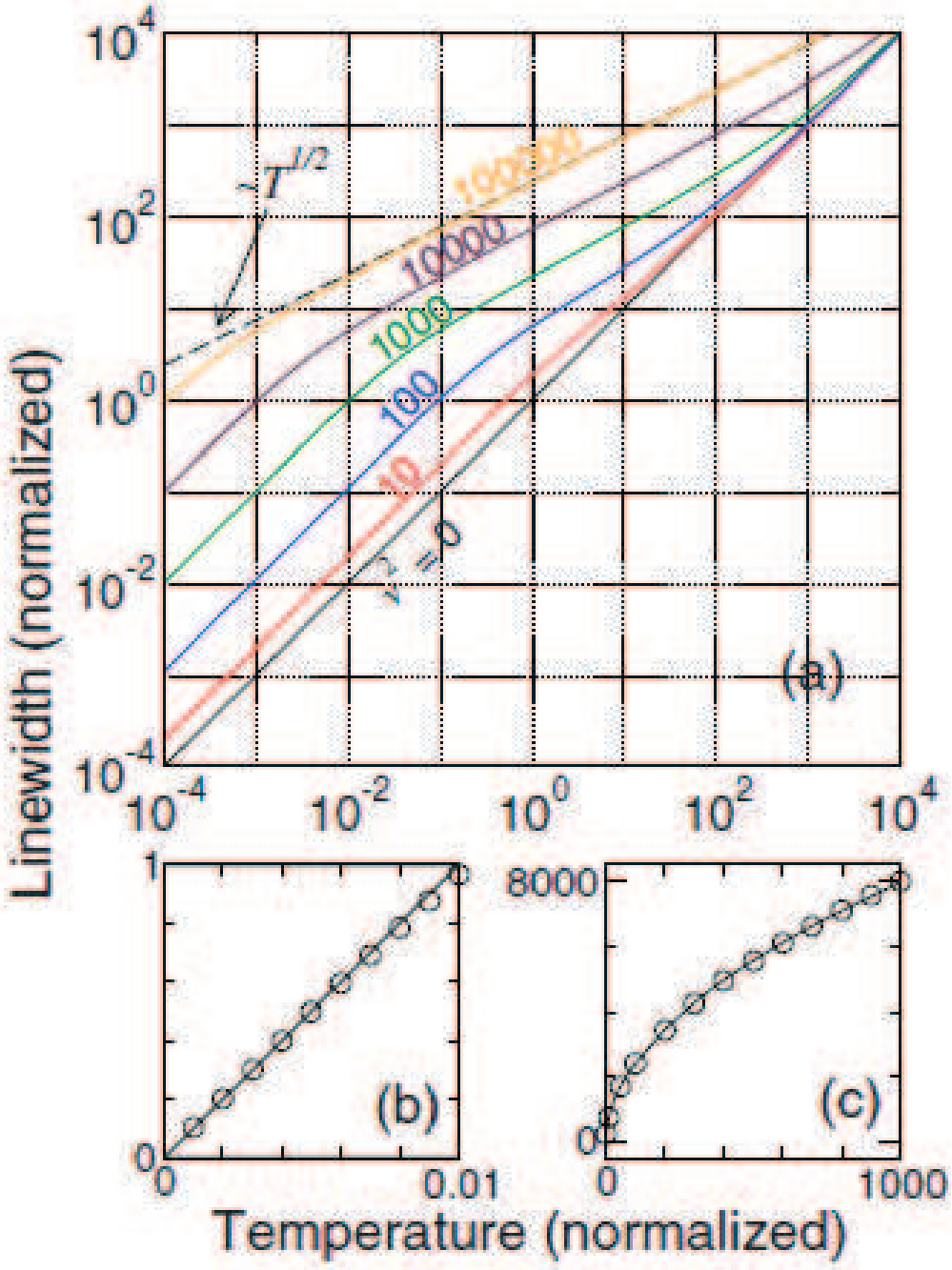


Figure 3.3: (a) Temperature dependence of the linewidth of a non-linear auto-oscillator at different values of non-linearity, ν. When ν =0 (i.e. linear oscillator), the linewidth varies linearly as temperature. As ν increases, the temperature range over which the linewidth varies as T decreases and at very high ν, it varies as $\sqrt{T}$. (b) Low temperature limit for small non-linearity (ν^2 = 100), showing linear T dependence. (c) High temperature limit for large non-linearity (ν^2 = 10^8), showing $\sqrt{T}$ dependence. Figure from [32].

Landau-Lifshitz-Gilbert equation, for which Q=0, so Γ_P is smaller and therefore one needs a smaller temperature for $\Delta\omega$ to cross the smaller Γ_P. Therefore the cross-over from linear-T dependence to $\sqrt{T}$ is smaller than in the case of Tiberkevich et al. That is why Sankey et al. may be seeing $\sqrt{T}$ temperature dependence, because the linear regime of their temperature dependence may be occuring only at extremely small temperatures.

3.3.2 Thermally-Activated Hopping between Dynamical Modes

The linewidths can also be affected by thermally-activated hopping between different dynamical modes. This may happen if there are two dynamical modes of different frequencies but nearly degenerate energies. In this case, the linewidths would depend on the thermal-activation barrier, E_B [12].

$$\Delta f = \frac{1}{\pi \tau} = \frac{f}{\pi} exp\left(\frac{-E_B}{k_B T}\right) \tag{3.11}$$

Previous experiments have shown that the magnetization can telegraph between static and meta-stable or dynamical states [35, 36, 12, 37] (Figure 3.4). In this case, the frequency spectrum has a large low-frequency tail that appears to be centered about zero frequency (Figure 3.4(a)). The magnetization can also telegraph between two different dynamical states. In this case, the frequency spectrum has two closely-spaced spectral peaks of two distinct frequencies [38]. Krivorotov et al. [36] demonstrated this by a very neat experiment in the time-domain. They found that if they did a Fourier Transform over a long time, they saw two closely-spaced spectral peaks of distinct frequencies (Figure 3.4(c)), but if they did a Fourier Transform over shorter time intervals, they saw only one spectral peak at one of the two frequencies (Figure 3.4(d)-(e)).

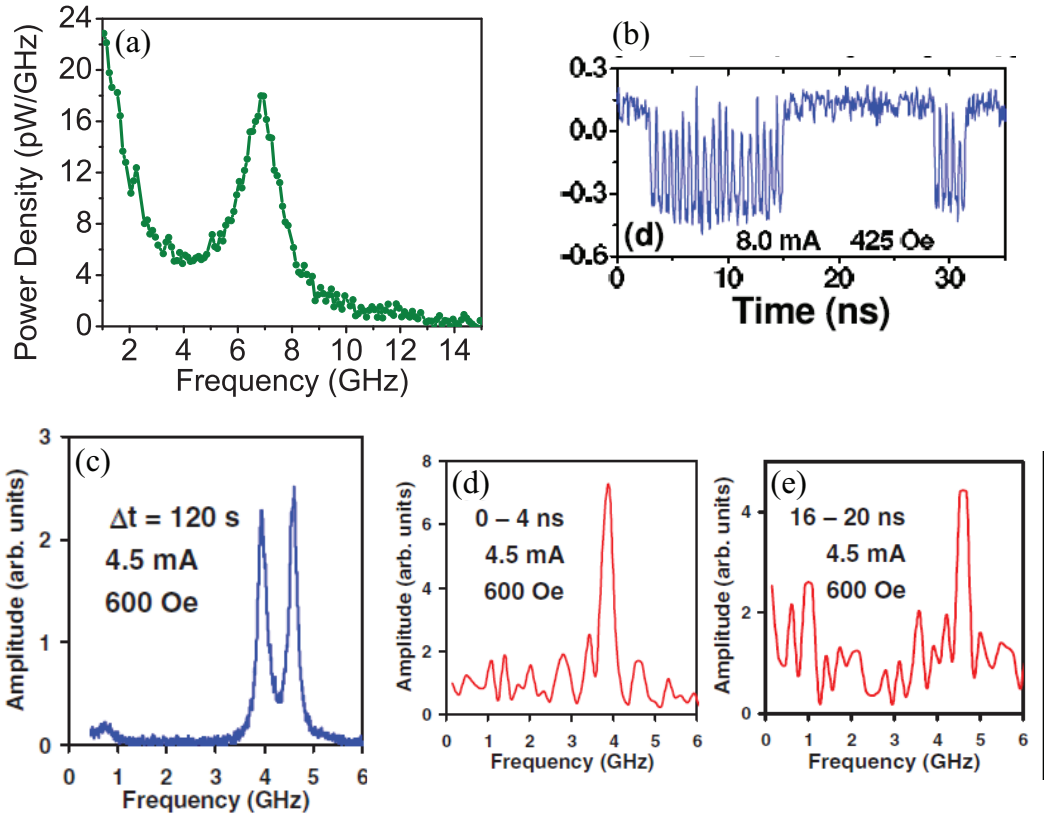


Figure 3.4: Power spectra for magnetization telegraphing between static and meta-stable or dynamical states. (a) Power spectral density showing a large low-frequency tail when the magnetization telegraphs between a static and dynamical state. (b) Example of time-domain measurements of the magnetization when it telegraphs between a static high-resistance state and a large-amplitude dynamical state. (c) Fourier transform of telegraphing between two dynamical states of different frequencies. (d)-(e) Fourier transform over a smaller time-interval shows only one of the two frequencies. Figures (b)-(e) from [36].

3.4 Linewidths as a Function of In-Plane Magnetic Field Angle

3.4.1 Devices: Structure & Fabrication

We will report results from two types of multilayer devices, both with a nanopillar geometry. In both cases the magnetic "free layer" that precesses is 4 nm of permalloy (Py, $Ni_{81}Fe_{19}$). In the first geometry, the magnetic "fixed layer" that

polarizes the current is 4 nm of Py exchange-biased to a layer of antiferromagnetic IrMn. The full layer structure is (with thicknesses in nanometers): 4 Py / 80 Cu / 8 IrMn / 4 Py / 8 Cu / 4 Py / 20 Cu / 30 Pt and a Cu top contact (Figure 3.5(a)). The second type of sample has a thicker Py fixed layer (20 nm) with no exchange bias: 2 Py / 120 Cu / 20 Py / 12 Cu / 4 Py / 12 Cu / 30 Pt with a Cu top contact (Figure 3.5(b)). The samples are fabricated using the procedure described in [39, 40] and Section 2.1. First the layers are deposited by sputtering, and then electron-beam lithography and ion milling are used to etch through both the free and fixed magnetic layers to the bottom Cu contact, giving a device cross section that is approximately elliptical (Figure 3.6(a) inset). The minor diameter of the cross section is 50-70 nm, and we have studied samples with aspect ratios of both 2:1 and 3:1. We use photolithography to pattern bottom leads and to make top contacts. For the exchange-biased samples, we sputter the layers in a magnetic field (300 Oe) and anneal at 220°C for 85 minutes before patterning to pin the fixed layer direction along the long axis of the ellipse. In this chapter, we will show data from one 50×150 nm^2 exchange-biased fixed-layer device and one 70×130 nm^2 thick-fixed-layer device. Similar results were obtained in 17 exchange-biased samples and 5 thick-fixed-layer devices.

3.4.2 DC-Characterization

Figure 3.6 shows the differential resistance (dV/dI) as a function of current (I) and magnetic field (H) for the two devices at room temperature. For the device with the exchange-biased fixed layer, as the current is swept (Figure 3.6(a)), at low magnetic fields we observe hysteretic switching between the parallel and anti-parallel magnetic orientations with a resistance change at zero bias ΔR =

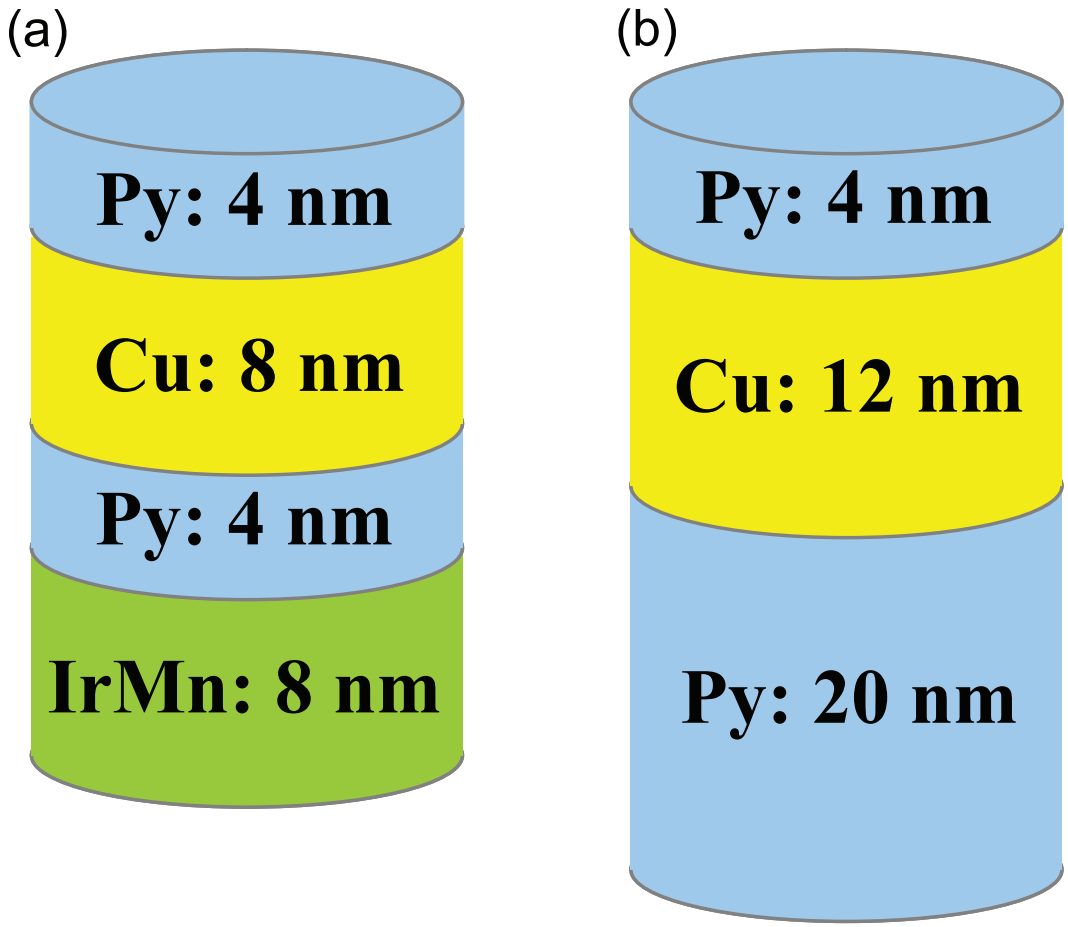


Figure 3.5: Layer structure of the two types of nanopillar spin-valve devices that we studied. (a) Layer structure for the device with an exchange-biased fixed layer. (b) Layer structure for the device with a thick fixed layer.

0.094 Ω, and above H = 450 Oe we find non-hysteretic peaks in dV/dI that are associated with transitions among precessional and static magnetic states. At zero bias, as the magnetic field is swept in the direction of the long axis of the sample cross section (the magnetic easy axis, "0 degrees") (Figure 3.6(b)), we observe switching of the magnetic layers between parallel and anti-parallel alignment. The transitions on the right in Figure 3.6(b) are associated with transitions of the magnetic free layer. From these, we infer that the effective dipole field of the fixed layer acting on the free layer is H_{dipole} = 80 Oe, the coercive field of the

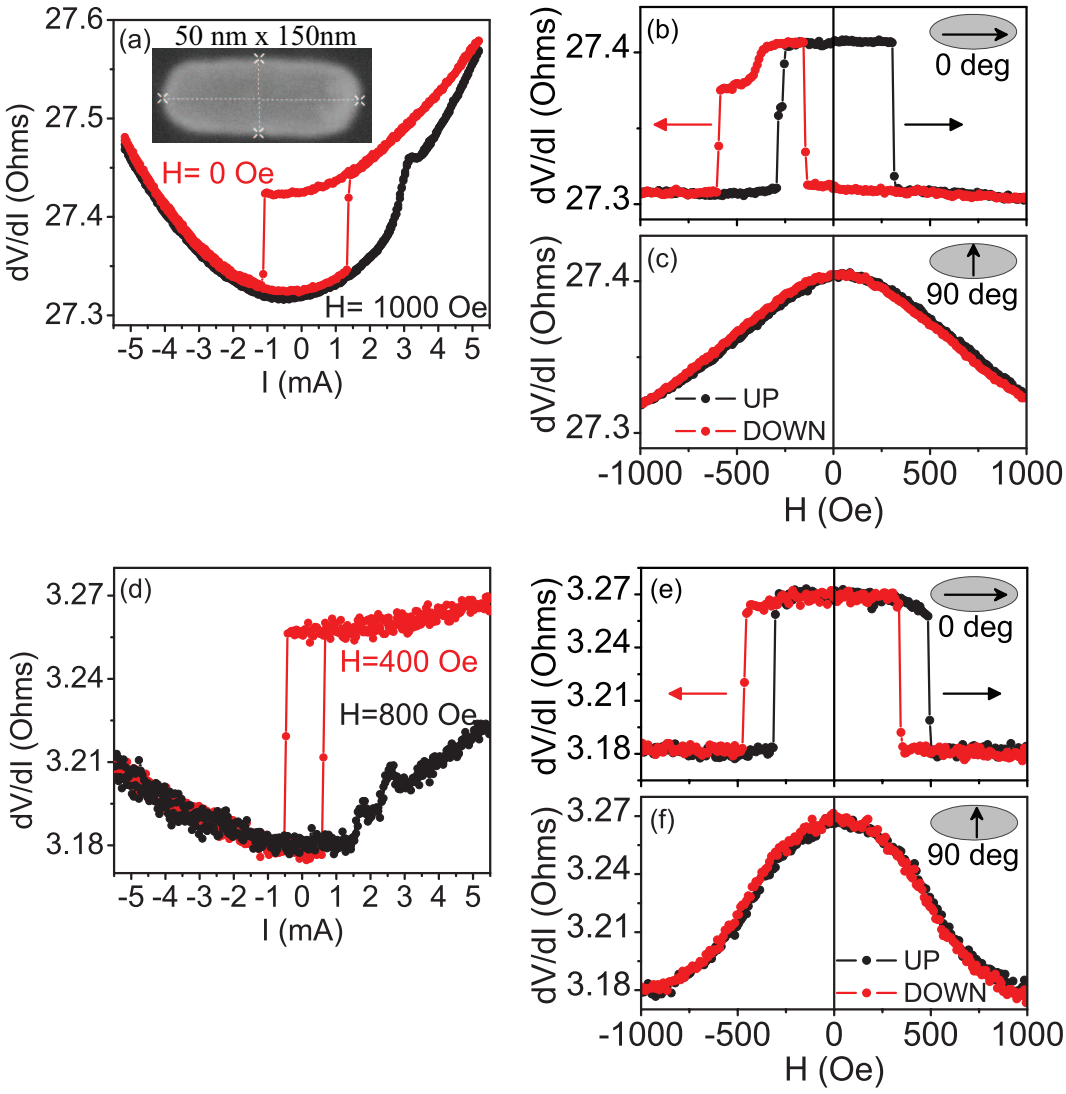


Figure 3.6: (a) Differential resistance as a function of current at room temperature for a nanopillar spin valve device with an exchange-biased fixed layer. Inset: top-view electron micrograph of device shape. (b, c) Resistance as a function of magnetic field for the same device for fields (b) along the easy-axis direction and (c) along the in-plane hard axis. (d-f) Differential resistance of a nanopillar spin valve device with a thick fixed layer as a function of (d) current and (e, f) magnetic field at room temperature.

free layer at room temperature is $H_{an} \approx 200$ Oe. From the transitions on the left, we find that the sum of the exchange bias and effective field on the fixed layer is $H_{EB} = 360$ Oe. As the field is swept in the perpendicular in-plane direction (the in-plane hard axis, "90 degrees") (Figure 3.6(c)), the angle between the layers changes smoothly from the antiparallel orientation to parallel. The device with the thick fixed layer (Figure 3.6(d)-(f)) is similar, except that the 0 degree magnetic-field sweep shows no exchange bias acting on the fixed layer. For this device, from minor loops for the free layer, we determine $H_{dipole} = 400$ Oe and $H_{an} \approx 100$ Oe.

3.4.3 High-Frequency DC-Driven Spectra

Our main focus will be high-frequency voltage oscillations produced by spin-torque-driven magnetic precession driven by a direct current. These oscillations arise because precession of the magnetic moment of the free layer causes microwave-frequency changes in the resistance of the magnetic multilayer due to the giant magnetoresistance (GMR) effect, and in the presence of a DC current bias these produce voltage oscillations according to Ohm's law. We measure the frequency spectrum of the voltage oscillations using a heterodyne mixer circuit, as described in Section 2.2.2. We perform all measurements at room temperature, with a large in-plane magnetic field applied using a projected field electromagnet [41] (Section 2.2.4) that allows us to control the field angle θ_H continuously. For the field values used in our experiment (800-1000 Oe), both the measured resistances and macrospin modeling using the parameters determined above indicate that for the exchange-biased samples the offset angle between the magnetic moments of the two layers grows from 0° to $\sim 35^\circ$ as θ_H is in-

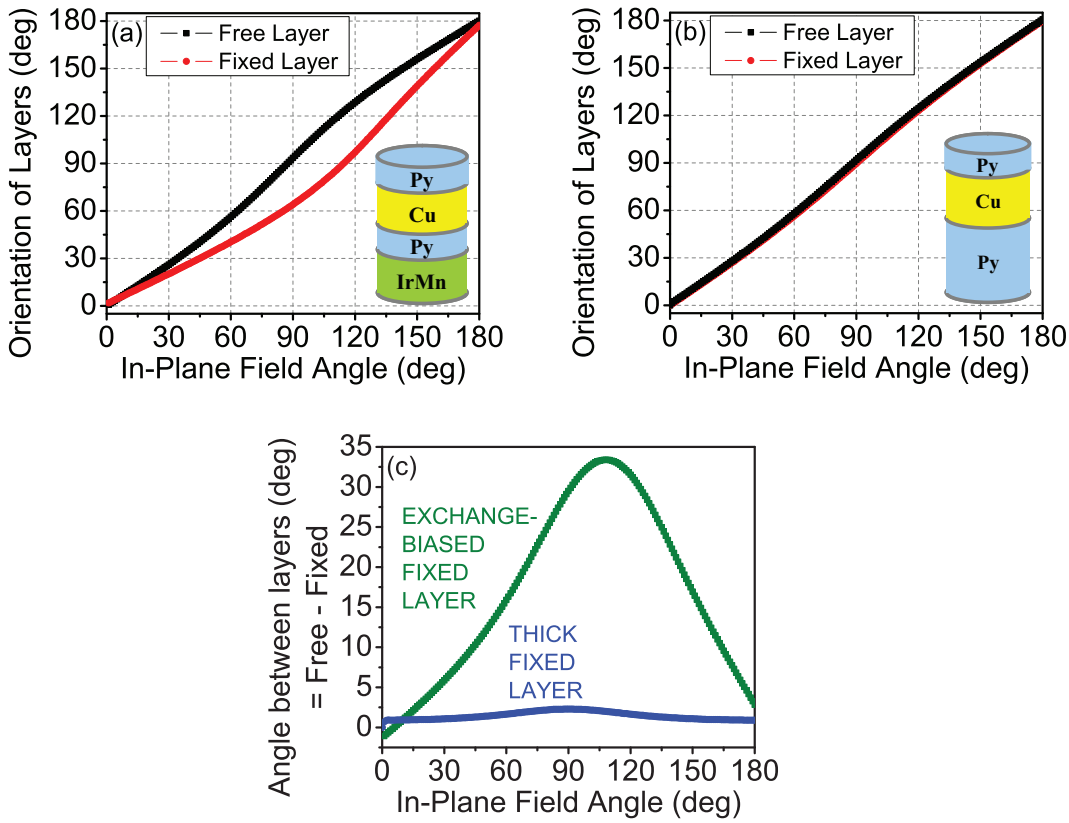


Figure 3.7: Stoner-Wohlfarth macrospin calculations of the orientation of the fixed and free magnetic layers and the relative angle between them as a function of the in-plane magnetic field angle, θ_H. (a) Calculated orientation of the fixed and free layers for an exchange-biased-fixed-layer device at H = 1000 Oe using the following parameters: H_{an} = 200 Oe, H_{dipole} = 100 Oe and H_{eb} = 360 Oe at 5° relative to the easy axis. (b) a thick-fixed-layer device at H = 800 Oe using the following parameters: H_{an} = 100 Oe, H_{dipole} = 400 Oe. (c) Calculated relative angle between the magnetic layers for the two kinds of devices.

creased from 0° to 90°, while for the thick-fixed-layer devices without exchange bias the offset angle is always < 5° (Figure 3.7).

Figures 3.8(a) and 3.8(b) show DC-driven spectra for the exchange-biased device at 1000 Oe and the thick-fixed-layer device at 800 Oe, at selected values of θ_H. The current bias is 5 mA, significantly larger than the critical current needed to excite magnetization dynamics for any θ_H. In the exchange-biased device, when H is applied along the magnetic easy axis in the direction of the exchange

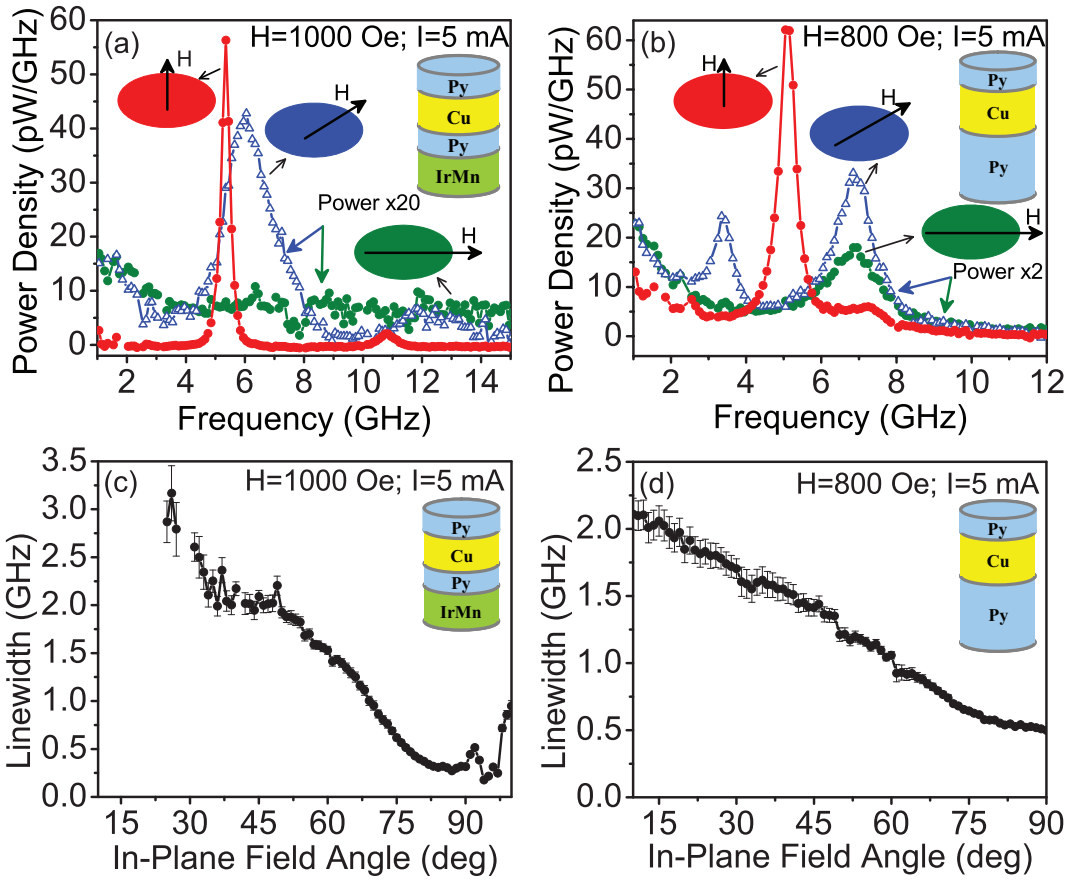


Figure 3.8: Power spectral density of spin-torque-driven oscillations at room temperature, for field angles $\theta_H = 0°, 45°$, and $90°$ (as labeled), for (a) an exchange-biased-fixed-layer sample and (b) a thick-fixed layer sample. Insets: sample structures. (c,d) Variation of the linewidth as a function of θ_H for both types of samples.

bias ($\theta_H = 0°$), there is no visible precessional peak, just a low-frequency tail indicating aperiodic dynamics. A precessional peak is first resolvable for $\theta_H \approx 25°$, and at $\theta_H = 45°$ there is a broad peak near 6 GHz with a linewidth (full width at half maximum, FWHM) of 2 GHz, along with a smaller second harmonic peak. As θ_H is increased further toward 90°, the linewidth decreases dramatically. The minimum linewidth for $I = 5$ mA is 170 MHz at $\theta_H = 95°$, a factor of 20 narrower than at $\theta_H \approx 25°$ (Figure 3.8(c)). If one selects the current and field magnitudes at which the linewidth narrowing is largest, we observe narrowings as a function

of θ_H ranging from a factor of 10 to 50 in all of our exchange-biased samples. We do not show here the devices in which the factor of 50 was observed because the narrowest peaks were limited by the resolution bandwidth chosen for the measurements.

We see a similar, but somewhat less dramatic dependence of linewidth on θ_H for the thick-fixed-layer device (Figure 3.8(b,d)). In this case a broad precessional peak is visible even for $\theta_H = 0°$ at a frequency corresponding to the second harmonic of the precessional frequency. At $\theta_H = 45°$, this second harmonic peak has narrowed by about 30% and a peak at the fundamental precession frequency is also visible. For $\theta_H = 90°$, the second harmonic frequency is again much larger than the fundamental, and the linewidth of the second harmonic reaches a minimum of 450 MHz, a factor of 5 less than the linewidth at $\theta_H = 0°$. We observed linewidth narrowing as a function of θ_H by factors between 2 and 5 in all of our thick-fixed-layer devices.

3.4.4 Analysis as a Function of Magnetic Field Angle

For the analysis, we will focus on the linewidth of the spectral peak at the fundamental precessional frequency for the exchange-biased fixed-layer sample, and the second harmonic of the thick-fixed-layer sample, because these are the largest signals. The reason that the fundamental peak and the second harmonic peak have different relative amplitudes in the two samples can be understood from the magnitude of the offset angle between the fixed and free layer magnetic moments at $I = 0$. For the range of magnetic field strengths that we apply, there is a non-zero offset angle between the magnetic moments in the exchange-

biased fixed-layer sample whenever $\theta_H \neq 0^\circ$ or 180°. Due to the nonzero offset angle, small-angle magnetic precession of the free layer produces a time-varying resistance signal with a fundamental frequency equal to the precession frequency. For the case of the thick-fixed-layer sample, the absence of an exchange bias layer causes the offset angle between the fixed and free layer magnetizations to be much smaller, and to go to zero for $\theta_H = 0^\circ$ and 90°, where the moments of both magnetic layers should be saturated along the field direction. When the precession amplitude is larger than the equilibrium offset angle, one cycle of precession produces two cycles of resistance, so the dominant signal should be at the second harmonic of the precession frequency. It is a coincidence that the first harmonic signal in Figure 3.8(a) and the second harmonic in Figure 3.8(b) both occur near the same frequency when $\theta_H = 90^\circ$. This is the result of the large value of H_{dipole} in the thick-fixed-layer sample, which points opposite to the external field acting on the free layer, so that it reduces the total field and therefore also reduces the precessional frequency of the free layer, compared to the exchanged-biased fixed layer sample.

In order to determine why the linewidths vary so strongly, we have analyzed the linewidth, precession frequency, and power of the precessional signals as a function of field angle and current for the two types of samples. For the exchange-biased-fixed-layer samples (Figure 3.9), as a function of increasing field angle up to $\theta_H \approx 90^\circ$ the signal displays a decreasing frequency and an increasing total power, together with the decreasing linewidth. The increasing power suggests that the precession amplitude grows as a function of θ_H at fixed current, while the frequency shift is consistent with an increasing demagnetization field and an increased precession amplitude. The narrowest linewidths are observed for θ_H between 75° and 95°, and for small currents (2.5 - 4 mA),

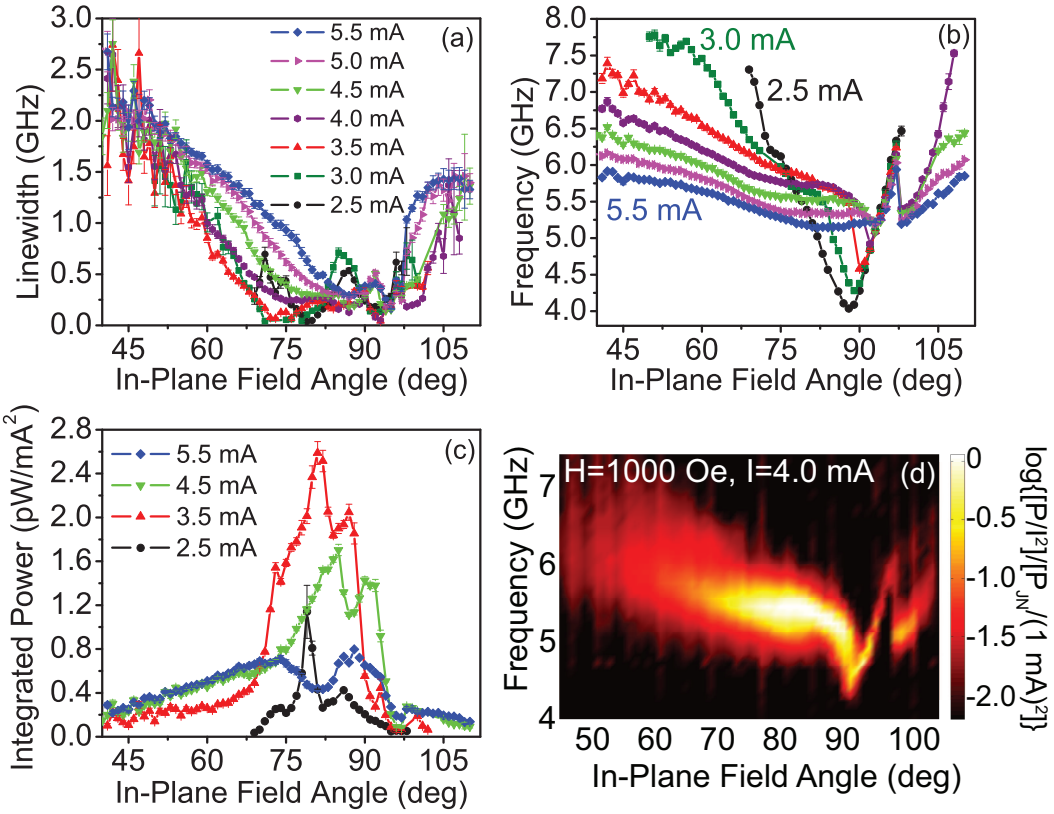


Figure 3.9: Analysis of the spin-torque-driven microwave signals as a function of θ_H for the sample with the exchange-biased fixed layer as a function of current and field angle at room temperature and $H = 1000$ Oe. (a) Linewidth. (b) Peak frequency. (c) Integrated power within the precessional peak divided by I^2. (d) Power spectral density plotted on a logarithmic scale, as a function of θ_H, for $I = 4$ mA.

the minimum linewidths approach 40 MHz, close to the resolution bandwidth employed in the measurements. Beyond $\theta_H \approx 95°$ (the exact value is current dependent), the total power in the precessional signal drops abruptly by a factor of 10 and the frequency undergoes changes in slope and jumps as a function of θ_H. We suspect that these changes may be associated with transitions in the magnetization state of the fixed layer. Between $\theta_H = 97°$ and $\theta_H = 110°$, the frequency becomes more current-dependent, the total power decreases slightly, and the linewidth increases with field angle at all currents. Beyond $\theta_H = 110°$,

there is no visible precessional peak in the spectrum. The dependence of the power spectrum on θ_H (for I = 4 mA) is summarized in a logarithmic-scale plot in Figure 3.9(d). We note that the lack of symmetry about $\theta_H = 90°$ in all of the panels of Figure 3.9 shows that the exchange bias of the fixed layer is still playing a role, even though the magnitude of the applied magnetic field is greater than the exchange-bias field. The dynamics show no dependence on whether θ_H is swept up (0° to 180°) or down (180° to 0°).

For the thick-fixed-layer sample (Figure 3.10), the linewidths generally decrease with θ_H between $\theta_H = 0°$ and 90°, and increase between $\theta_H = 90°$ and 180° at all currents. In the ranges 30° – 75° and 105° – 130° the fits appear to suggest a non-monotonic dependence on θ_H, with peaks and abrupt jumps, but these are likely just artifacts of the fitting procedure, associated with the fact that the spectra at these angles seem to consist of two closely-spaced peaks (see Figure 3.10(d)) that are not well-described by Lorentzian fits. The measured frequencies vary smoothly as a function of θ_H (Figure 3.10(b)), with a form that is approximately symmetric about $\theta_H = 90°$, as expected in the absence of any exchange bias. As noted already in Figure 3.8, the decrease in the linewidth between $\theta_H = 0°$ and 90° for the thick-fixed-layer sample is less dramatic than the factor of 10-50 observed for the exchange-biased fixed layer samples. Figure 3.11(a)-(b) shows spectra at $\theta_H = 45°$ and $\theta_H = 135°$ as an example of the asymmetry about $\theta_H = 90°$ for the exchange-biased-fixed-layer sample and Figure 3.11(c)-(d) shows spectra at $\theta_H = 45°$ and $\theta_H = 135°$ as an example of the symmetry about $\theta_H = 90°$ for the thick-fixed-layer sample.

Since the free magnetic layer is nominally identical in the two kinds of samples (4 nm of Py), based on the large difference in the magnitude by which the

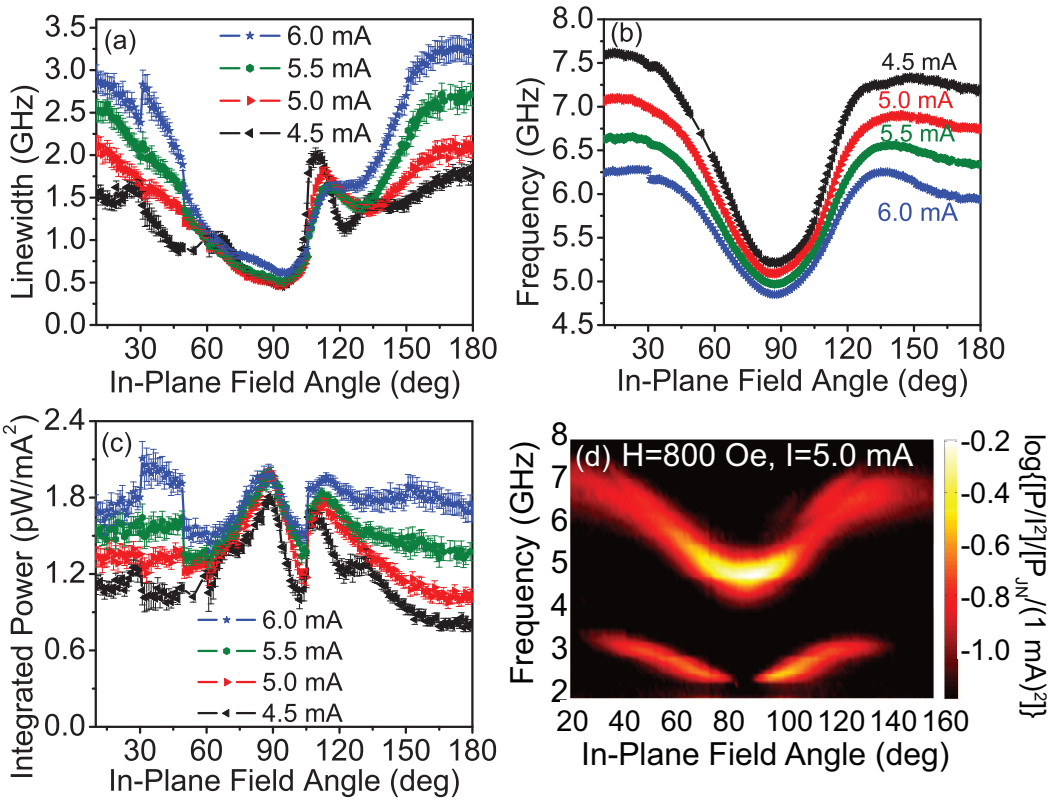


Figure 3.10: Analysis of the spin-torque-driven microwave signals as a function of θ_H for the sample with the thick fixed layer at room temperature and H = 800 Oe. (a) Linewidth. (b) Peak frequency. (c) Integrated power divided by I^2. (d) Power spectral density plotted on a logarithmic scale, as a function of θ_H, for I = 5 mA.

linewidths narrow as well as the differences in symmetry about $\theta_H = 90°$ in the two kinds of samples, we suggest that the orientation of the fixed layer must play an important role in the degree of coherence of the free layer. We have confirmed that the mode which is excited at different θ_H is always a free layer mode in both types of samples. This was determined by conducting spin-transfer-driven ferromagnetic resonance measurements (ST-FMR) [42, 30] on the samples as a function of θ_H; the sign of the ST-FMR signals corresponds to a free layer mode and not the lowest-frequency fixed layer mode [30]. The ST-FMR measurements will be discussed in more detail in Section 3.4.6.

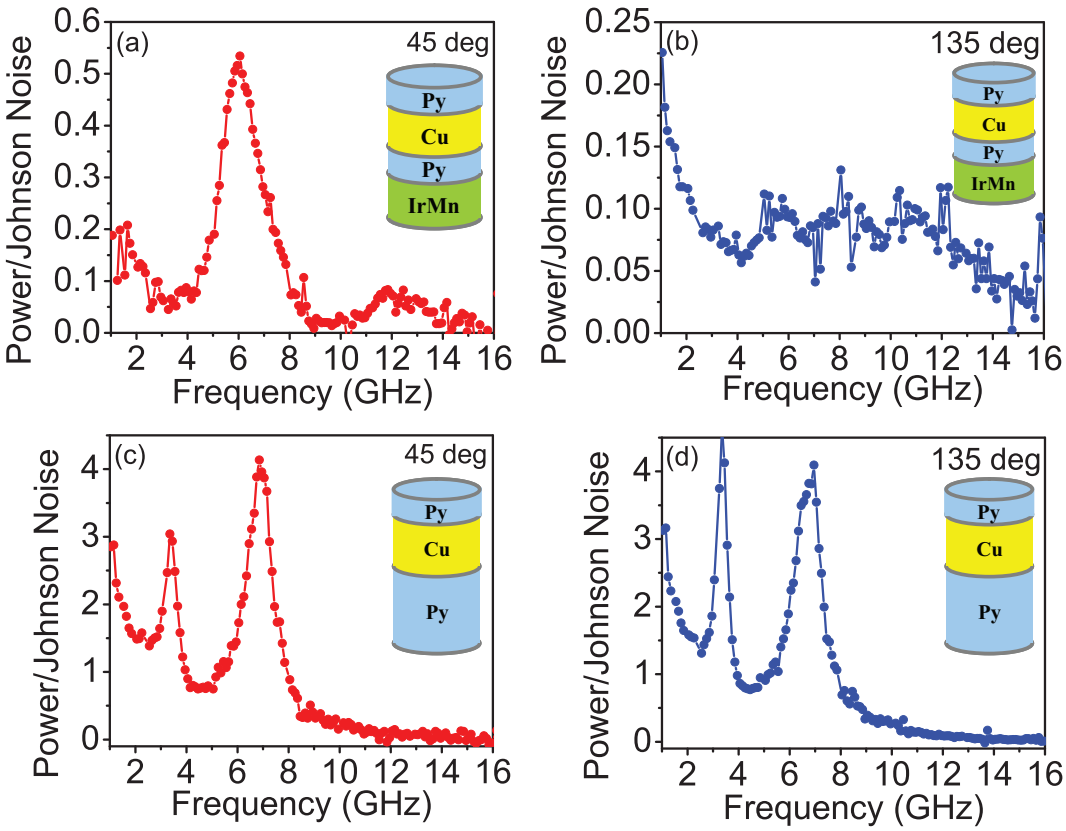


Figure 3.11: Examples of the differences in symmetry about $\theta_H = 90°$ between the two kinds of devices. Power spectral density at $\theta_H = 45°$ and $\theta_H = 135°$ for the (a) exchange-biased-fixed-layer device and the (b) thick-fixed-layer device.

3.4.5 Analysis as a Function of Current: Qualitative Correlation between Linewidth and df/dI

As we discussed in Section 3.3, the linewidths are proportional to the quantity $(df/d\theta_{max})^2$ since they are predicted to increase as a function of the nonlinearity of the oscillator - the degree to which the average precession frequency, f changes with the amplitude θ_{max} of the precession [12, 20]. Since increasing the current should increase the precession angle θ_{max}, regions with small values of df/dI should also have small values of $df/d\theta_{max}$. This motivated us to study whether the regions of narrow linewidths are correlated with regions where the

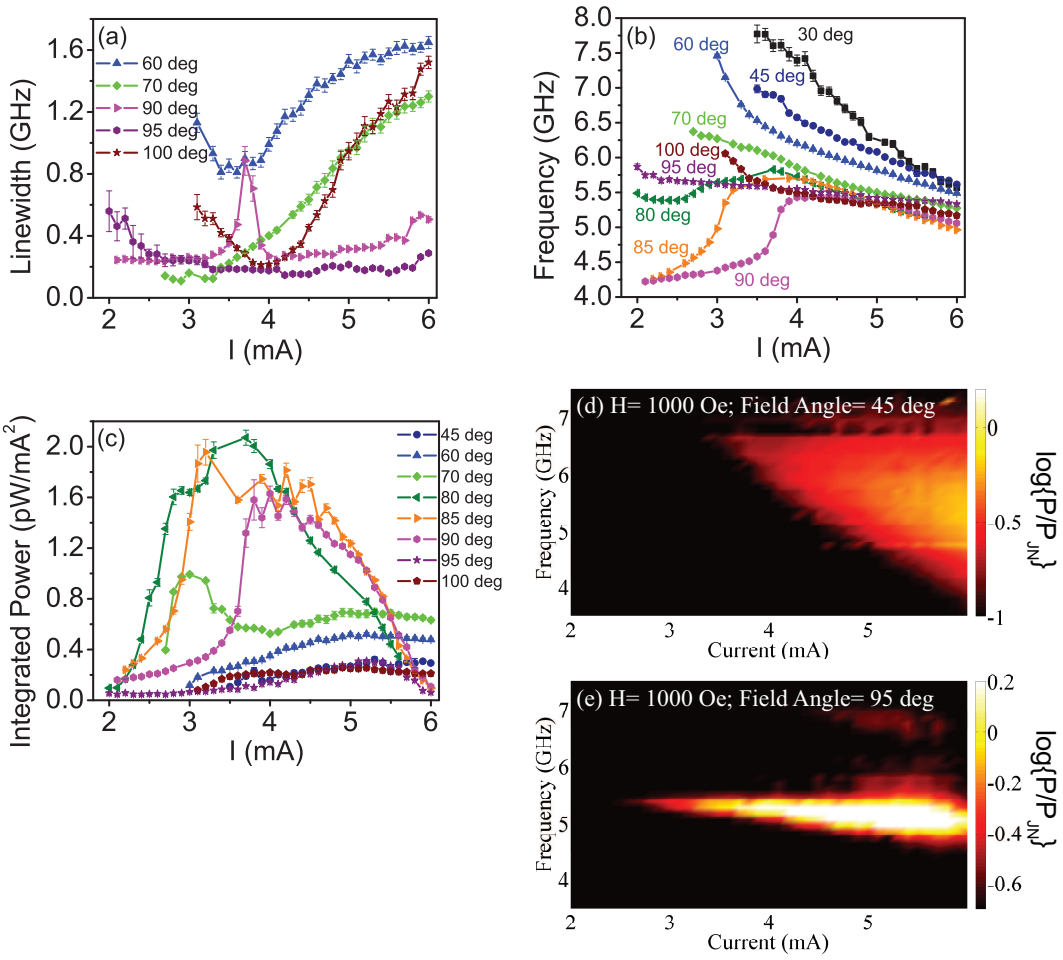


Figure 3.12: Analysis of the spin-torque-driven microwave signals as a function of current for the sample with the exchange-biased fixed layer at room temperature and $H = 1000$ Oe. (a) Linewidth. (b) Peak frequency. (c) Integrated power divided by I^2. (d) Power spectral density plotted on a logarithmic scale, as a function of current, for $\theta_H = 45°$ and (e) $\theta_H = 95°$.

precession frequency is nearly constant as a function of current. In Figures 3.12 and 3.13, we have analyzed the linewidth, frequency and power of the precession signals for the two types of samples as a function of current. For both types of samples, we observe a positive correlation between the observed linewidths and the corresponding df/dI.

In the exchange-biased-fixed-layer sample (Figure 3.12), for $\theta_H < 80°$, as a

function of current, the frequency decreases and the linewidth and power increase. The decrease in frequency and increase in power with current indicate that the oscillations persist in elliptical orbits and their precession amplitude increases with current. We note that at these field angles, the linewidths are broad and the frequency also decreases substantially with current, i.e. df/dI is large. In the range $80^\circ < \theta_H < 90^\circ$, the frequency first increases with current (for instance, till $I < 2.5$mA for $\theta_H = 85^\circ$, and till $I < 3.6$mA for $\theta_H = 90^\circ$), then there is a sudden jump in frequency at those currents, and above those currents, the frequency decreases with current. The jumps in frequency at $I = 2.5$mA for $\theta_H = 85^\circ$ and at $I = 3.6$mA for $\theta_H = 90^\circ$ suggest that there may be a transition between two modes with different frequencies. This is also confirmed by the sudden increase in linewidth and power at those currents. In the range $90^\circ < \theta_H < 97^\circ$, for instance at $\theta_H = 95^\circ$, we observe the narrowest linewidths and we also see that the frequency stays almost constant with current, i.e. df/dI is very small. We also noted the independence of frequency on current in this range of θ_H in Figure 3.9(b). In the range $97^\circ < \theta_H < 110^\circ$, for instance at $\theta_H = 100^\circ$, the linewidths start to broaden again and the frequencies also decrease with current (i.e. df/dI increases). The dependence of the power spectrum on I (for $\theta_H = 45^\circ$ and $\theta_H = 95^\circ$) is summarized in a logarithmic-scale plot in Figure 3.12(d). We can see that at $\theta_H = 45^\circ$, the linewidth is broad and the frequency decrease with current is large (large df/dI). At $\theta_H = 95^\circ$, where we observe the narrowest linewidths, the frequency also doesn't change much with current (small df/dI). We see a similar dependence on current for the thick-fixed-layer sample (Figure 3.13).

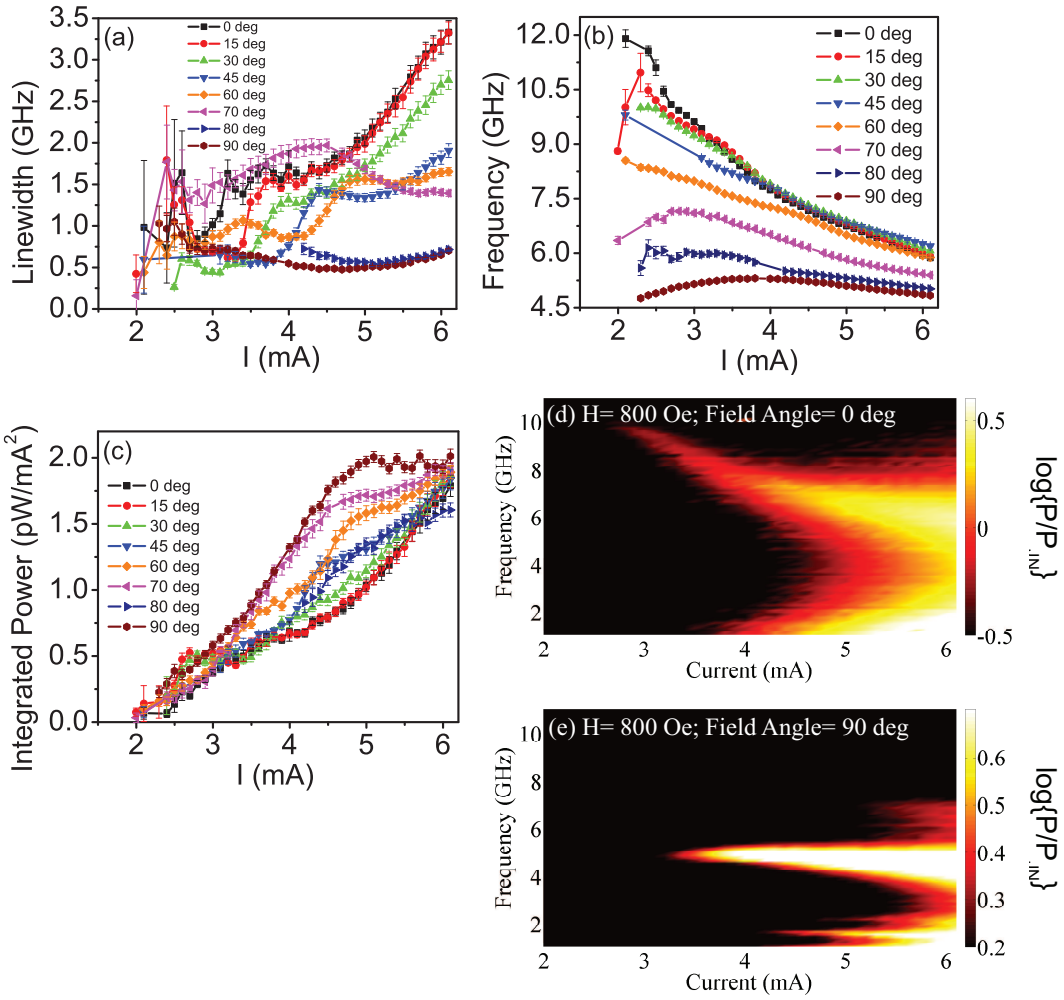


Figure 3.13: Analysis of the spin-torque-driven microwave signals as a function of current for the sample with the thick fixed layer at room temperature and H = 800 Oe. (a) Linewidth. (b) Peak frequency. (c) Integrated power divided by I^2. (d) Power spectral density plotted on a logarithmic scale, as a function of current, for $\theta_H = 0°$ and (e) $\theta_H = 90°$.

3.4.6 Spin-Torque-Driven Ferromagnetic Resonance Measurements (ST-FMR)

In order to determine if the oscillations in the DC-driven experiment discussed in Section 3.4.3 correspond to the normal modes of the free layer or the fixed layer, we conducted spin-torque-driven ferromagnetic resonance (ST-

FMR) measurements [42, 30] on the same devices under exactly the same current and magnetic field conditions. In addition to I_{DC}, we applied a radio-frequency (RF) current, I_{RF} = 0.42 mA and measured the amplitude of the resonant motion by measuring the dc-voltage corresponding to the mixing of I_{RF} and the changing resistance due to spin-torque (as described in Section 2.2.3). We conducted detailed ST-FMR measurements on 4 of the 22 devices measured in the DC-driven experiment and observed similar results in all 4. In this section, we will describe the ST-FMR results for the same 50×150 nm^2 exchange-biased-fixed-layer device that was discussed in previous sections. We applied the same magnetic field, H = 1000 Oe as in the DC-driven experiment (Section 3.4.3) and varied the magnetic field angle, θ_H between 0° and 180°. At each θ_H, we varied the I_{DC} and measured the ST-FMR spectrum at each I_{DC} to compare directly with the spectra in Section 3.4.3.

Figures 3.14(a) and 3.14(b) show the DC-driven spectra and the corresponding ST-FMR spectra at different θ_H at H = 1000 Oe and I_{DC} = 5.0 mA. In Figure 3.14(b), we can only see ST-FMR spectra for $\theta_H > 72°$, because the ST-FMR signal below 72° degrees is very small due to the small misalignment angle between the magnetic layers (the torque is roughly proportional to sin(θ), where θ is the angle between the layers). We would like to make two main points regarding the ST-FMR data. First, we can clearly identify the DC-driven peaks (Figure 3.14(a)) in the ST-FMR spectrum (Figures 3.14(b)). For example, the 90° peak at I_{DC} = 5.0 mA in the DC-driven spectrum, which was also shown in Figure 3.8(a) is visible at almost the same frequency in the ST-FMR spectrum. Figures 3.14(c) and 3.14(d) show the frequencies of the DC-driven spectral peaks and the corresponding frequencies of the ST-FMR spectral peaks, as a function of I_{DC} at different θ_H. We see that the frequencies above I_{DC} = 2.0 mA match very well

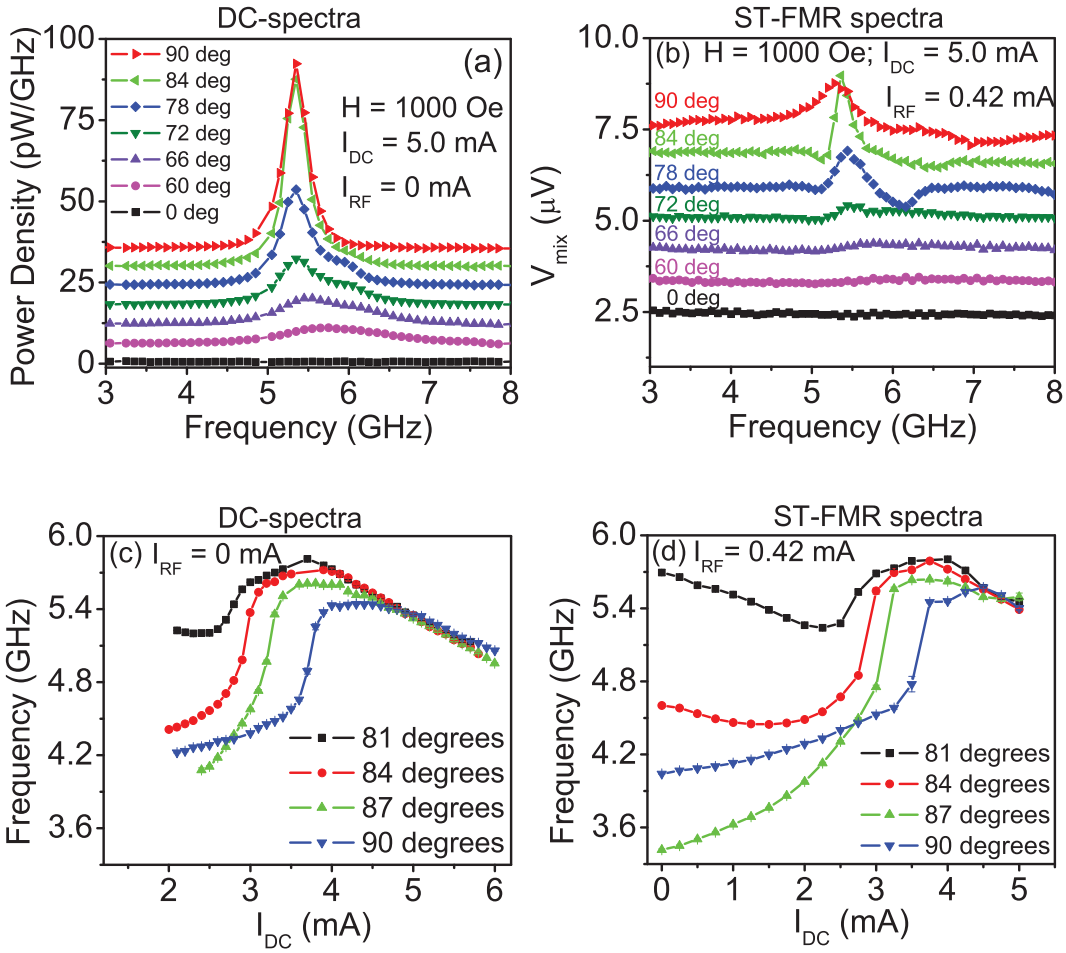


Figure 3.14: Comparison of DC-driven spectra and ST-FMR spectra for the exchange-biased-fixed-layer device at $H = 1000$ Oe. (a) Power spectral density from the DC-driven precessional modes at $H = 1000$ Oe and $I_{DC} = 5.0$ mA at different θ_H. The spectra are offset in increments of 1.5 pW/GHz. (b) ST-FMR spectra at $H = 1000$ Oe, $I_{DC} = 5.0$ mA and $I_{RF} = 0.42$ mA at different θ_H. The spectra are offset in increments of 0.4 μV. (c) Peak frequencies of the DC-spectra as a function of I_{DC} at different θ_H. (d) Peak frequencies of the ST-FMR spectra as a function of I_{DC} at different θ_H.

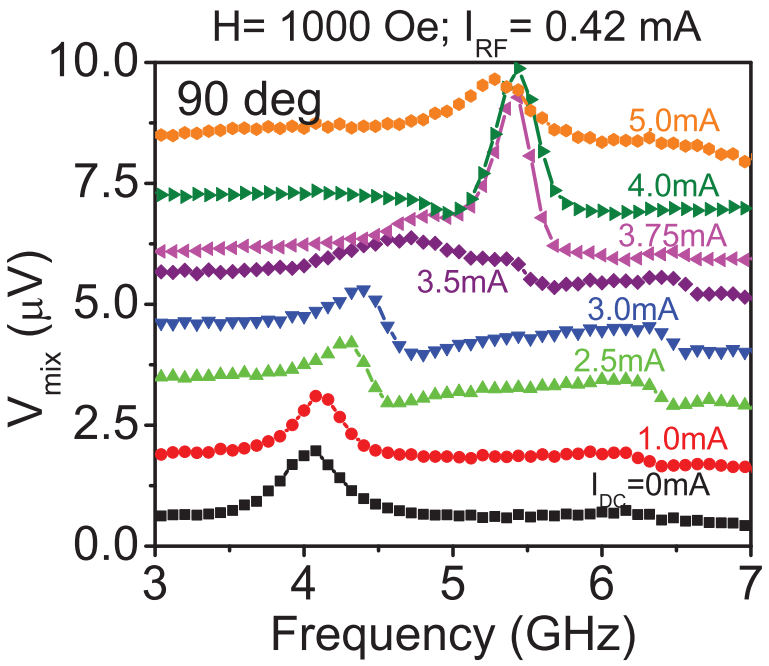


Figure 3.15: ST-FMR spectra at different I_{DC} at $\theta_H = 90°$ and $H = 1000$ Oe for the exchange-biased-fixed-layer device. The spectra are offset in increments of 0.4 μ V.

for both spectra. We would like to point out that in the ST-FMR experiment, we observe excitations even below the critical current, including at $I_{DC} = 0$ mA, because of the I_{RF} resonant drive. An example of the ST-FMR spectra at different I_{DC} is shown for $\theta_H = 90°$ in Figure 3.15. At $I_{DC} = 0$ mA, we are able to see a RF-driven positive peak at the FMR frequency. This zero-bias ST-FMR peak evolves into the DC-driven mode above $I_{DC} = 2.0$ mA, the critical current for DC-driven excitations. We discussed earlier in Section 3.4.5 that at θ_H close to 90°, there is an abrupt jump in frequency at certain I_{DC}. We ascribed this frequency jump to transitions between precession modes with different frequencies. In the ST-FMR spectra also, we see that between $I_{DC} = 3.5$ mA and $I_{DC} = 3.75$ mA, the peak frequency suddenly increases, corresponding to the same range of I_{DC} in which the sudden frequency transition in the DC-spectra occurs.

Second, we see that the ST-FMR peaks are positive at all θ_H. The sign of the torque, for a positive sign of I_{DC} in our measurement, should give a positive peak for a free layer mode and a negative peak for a fixed layer mode in the ST-FMR spectrum. This suggests that the mode which is excited at different θ_H is always a free layer mode. In addition, the zero-bias ST-FMR peak evolves smoothly into the DC-driven peaks at higher I_{DC}, indicating that we are exciting the lowest-frequency, most spatially uniform mode [12, 43]. We would like to point out that the shape of the ST-FMR peaks at large I_{DC} is complicated and not just a simple Lorentzian because of phase-locking between the DC-driven precession and I_{RF} [30].

3.4.7 Macrospin Simulations

We have performed macrospin simulations (as described in Section 2.3.1) in an attempt to understand our results. These were performed by integrating the Landau-Lifshitz-Gilbert equation for both magnetic layers and included a Slonczewski spin-torque term, the magnetic interaction between the layers, and fluctuating Langevin fields to model thermal fluctuations. We explored a range of parameters chosen to approximate the sample characteristics. For the exchange-biased-fixed-layer sample, we used the following parameters: H = 1000 Oe T = 300 K, exchange-bias field, H_{EB} = 360 Oe, 5° relative to the easy axis; H_{dipole} due to the fixed layer on the free layer = 100 Oe, H_{dipole} due to the free layer on the fixed layer = 100 Oe, $H_{anisotropy}$ of fixed and free layers = 200 Oe; thickness of free layer = 4 nm; thickness of fixed layer = 4 nm, area = 50×150 nm^2, free and fixed layer saturation magnetization M_S = 560 emu/cm^3, free layer damping α = 0.01; fixed layer damping = 0.1.

For the thick-fixed-layer sample, we used the following parameters: H = 800 Oe, T = 300 K, exchange-bias field, H_{EB} = 0 Oe, H_{dipole} due to the fixed layer on the free layer = 400 Oe, H_{dipole} due to the free layer on the fixed layer = 0 Oe, $H_{anisotropy}$ of fixed and free layers = 100 Oe, thickness of free layer = 4 nm, thickness of fixed layer = 20 nm, area = 70×130 nm^2, free and fixed layer saturation magnetization M_S = 560 emu/cm^3, free layer damping α = 0.01; fixed layer damping = 0.1.

Each simulation spanned 200 nanoseconds with a time step of 1 picosecond. The simulations were initialized with the two magnetic layers in the anti-parallel state, as is the case in the experiment due to the dipolar coupling between the layers.

Simulated Trajectories as a Function of Current

In Figures 3.16,3.17 and 3.18, we show the simulated trajectories of the oscillations for the thick-fixed-layer sample as the current is increased incrementally at H = 800 Oe and $\theta_H = 10°$. The same qualitative behavior was observed at all field angles studied in the simulations, as well as for the exchange-biased-fixed-layer sample. In Figures 3.16 (b),3.17 (b) and 3.18 (d) and (e), the x-axis is along the easy (major) axis of the elliptical sample, the y-axis is along the in-plane hard (minor) axis and the z-axis is along the hard, out-of-plane axis.

At I = 0 mA (Figure 3.16), when the magnetic layers are subjected only to the external magnetic field H = 800 Oe applied along $\theta_H = 10°$, the free layer is almost parallel to the field direction, the M_X component is close to 1, the M_Z component is close to 0 and the M_Y component oscillates a small amount. The oscillations are not completely periodic because of thermal fluctuations. This

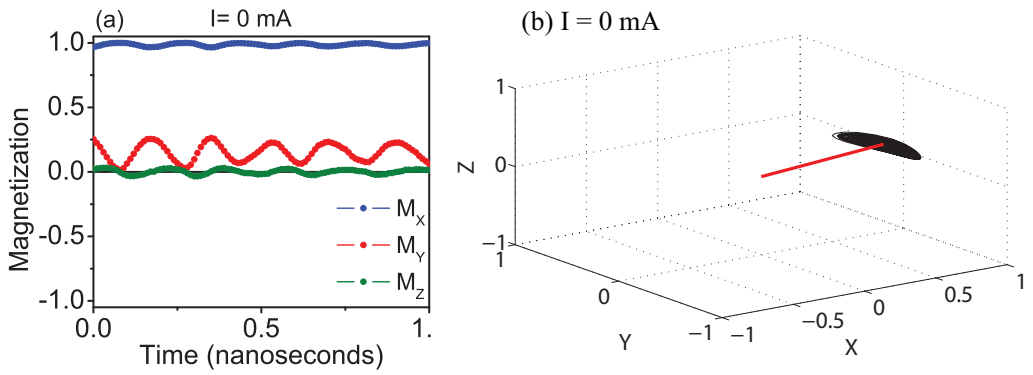


Figure 3.16: Simulated free-layer magnetization response and trajectory at $I = 0$ mA and $H = 800$ Oe, applied along $\theta_H = 10°$. (a) M_X, M_Y and M_Z as a function of time. (b) Magnetization trajectory. The red line indicates the direction of the applied magnetic field, θ_H.

state persists until the critical current (about $I = 1.3$ mA in the simulation). At $I = 1.3$ mA (denoted by $I/I_C = 1$) (Figure 3.17), steady-state oscillations begin and the free-layer magnetization precesses in an elliptical trajectory (the oscillations are elliptical and not circular because of the strong out-of-plane demagnetization field that tries to confine the precession in-plane). As the current is increased further, the amplitude of the oscillations keeps increasing, until the two ends of the elliptical trajectory merge at $I = 1.6$ mA ($I/I_C = 1.2$). Beyond this point, the magnetization telegraphs between two degenerate out-of-plane orbits. This is shown in Figure 3.18. In Figures 3.18 (a) and (d), an example of the telegraphing is shown at $I = 3.0$ mA ($I/I_C = 2.3$). The M_Z component is negative at certain times and positive at other times, as the moment telegraphs between the two out-of-plane orbits. As the current is increased further to $I = 3.5$ mA ($I/I_C = 2.7$) (Figure 3.18 (b)), the magnetization spends more and more time in one of the out-of-plane orbits than the other, but it still telegraphs between the two. Finally, at $I = 3.9$ mA ($I/I_C = 3$) (Figures 3.18 (c) and (e)), the moment settles into one of the out-of-plane orbits and precesses in that orbit forever.

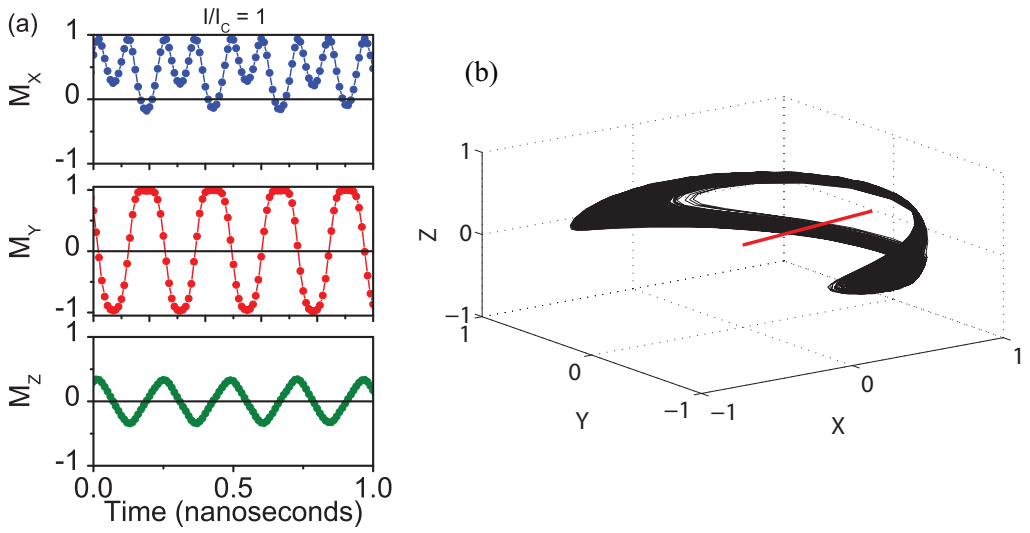


Figure 3.17: Simulated free-layer magnetization response and trajectory at $I/I_C = 1$ and $H = 800$ Oe, applied along $\theta_H = 10°$. (a) M_X, M_Y and M_Z as a function of time. (b) Magnetization trajectory, showing elliptical precession. The red line indicates the direction of the applied magnetic field, θ_H.

Comparison with experiment: The simulations predict that steady-state elliptical precession is stable over a much narrower range of current than we find experimentally. In the experiment, steady-state elliptical precession persists until at least $I/I_C = 3$, as shown in Figures 3.12 and 3.13. In the simulations, it persists until only approximately $I/I_C = 1.2$.

Simulated Linewidths as a Function of the Field Angle

We studied the linewidths calculated directly from the Fourier Transform of the GMR oscillations in the simulation, focusing particularly on the regime of elliptical precession (Figure 3.17). We found that the simulation results of the linewidths as a function of the field angle were extremely sensitive to the choice of parameters. For example, we were not able to observe any substantial narrowing in the linewidths for the parameters used for the exchange-biased-fixed-

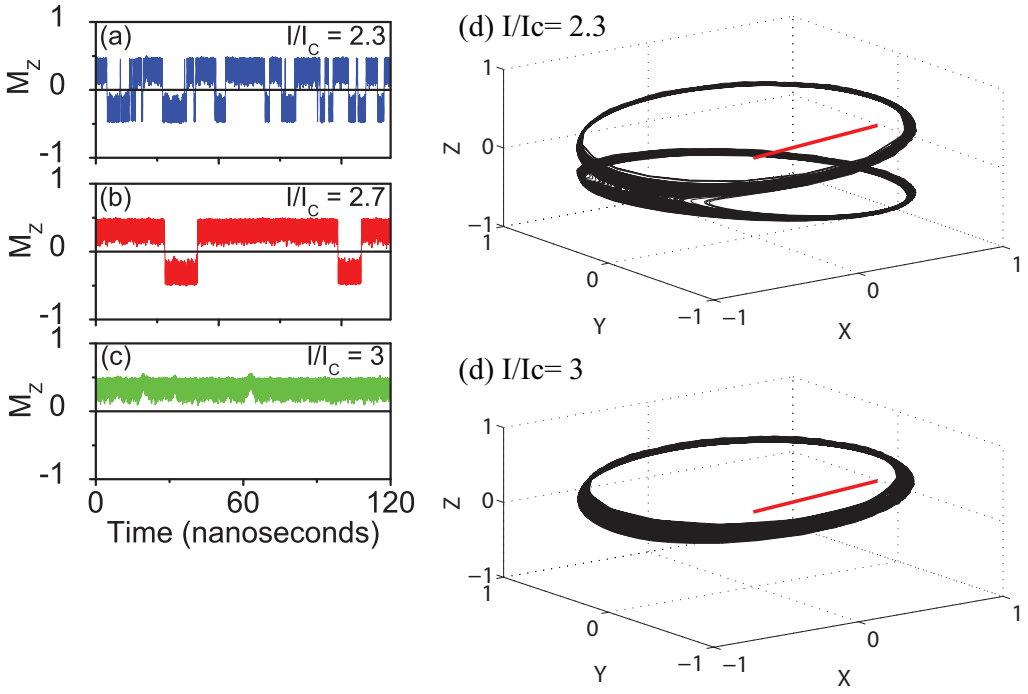


Figure 3.18: Simulated free-layer magnetization response and trajectory at $I/I_C = 2.3$, $I/I_C = 2.7$ and $I/I_C = 3$ at $H = 800$ Oe, applied along $\theta_H = 10°$. Out-of-plane component, M_Z, as a function of time at (a) $I/I_C = 2.3$, (b) $I/I_C = 2.7$ and (c) $I/I_C = 3$. (d) Magnetization trajectory, showing the merging of the two ends of the elliptical clamshell orbit and subsequent telegraphing between two degenerate out-of-plane orbits. (e) Magnetization trajectory, showing the magnetization settling into one of the out-of-plane orbits. The red line indicates the direction of the applied magnetic field, θ_H.

layer sample but we were able to observe some narrowing in the predicted linewidths using the parameters of the thick-fixed-layer sample. As θ_H is increased from 0° to 90° at room temperature, the linewidths narrowed by a factor of 2-3 (Figure 3.19). However, the decrease in the linewidths was not as large as observed experimentally. Whereas our macrospin simulations are unable to explain the large linewidth changes we measure, micromagnetic calculations give better agreement. We will discuss these next in Section 3.4.8.

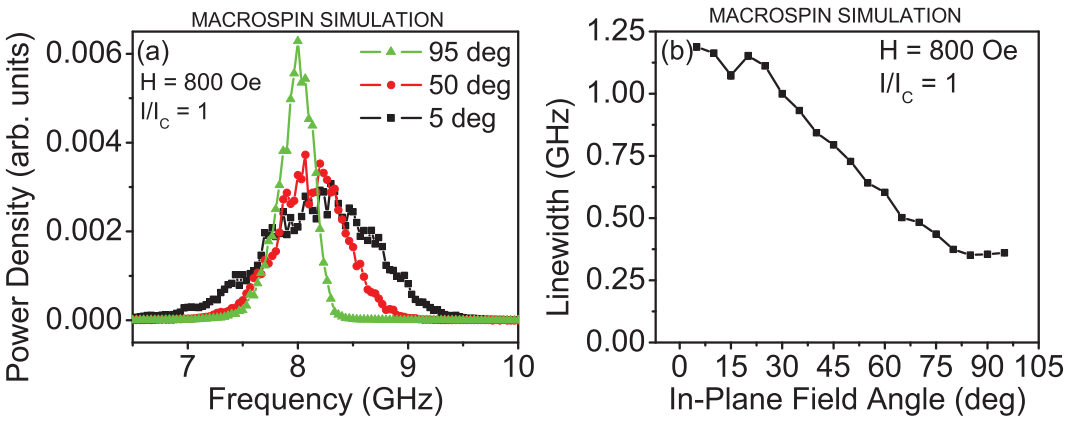


Figure 3.19: Simulated power spectral density and linewidth variations as a function of θ_H at $I/I_C = 1$ and $H = 800$ Oe. (a) Simulated power spectral density at $\theta_H = 5°$, $50°$ and $95°$. (b) Simulated linewidth as a function of θ_H.

Regarding Tiberkevich and Slavin's fits to our data

We would also like to point out that Tiberkevich and Slavin have reported that they are able to fit the large changes in linewidth that we observe using the stochastic nonlinear oscillator equation (Equations 3.8, 3.10) for the dominant spin wave mode [33]. They found that the linewidths in their calculations were closely related to the non-linear frequency shift, N, as a function of the in-plane field angle (Figure 3.20(a)). They found that for small H (case-1 in Figure 3.20(a)), the non-linear frequency shift, N, changes sign at $\theta_H = 80°$; at this angle, $N^2 = 0$ and the linewidth is also minimum. At higher fields (cases-2 and 3), the absolute value of the non-linear frequency shift decreases and hence the linewidth also decreases until N^2 approaches zero near 90°, where the linewidth becomes a minimum. Their theory predicts that the minimum linewidth should be achievable for an in-plane field angle close to 90° and a field close to 4 times the anisotropy field.

In Figure 3.20(b)-(c), we show the results of their calculations and fits to our

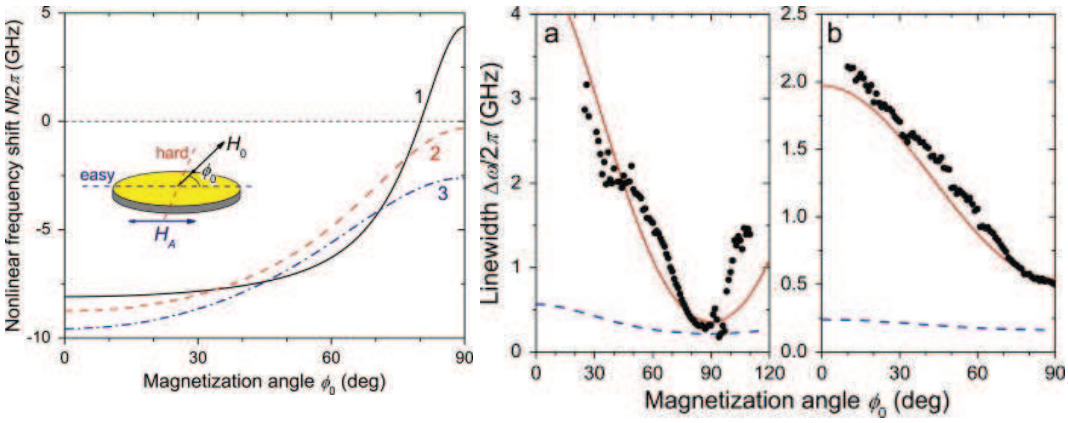


Figure 3.20: Calculations of the (a) non-linear frequency shift as a function of the in-plane field angle using the analytical expression of the generation linewidth for a non-linear oscillator. (b) calculated linewidth from the the non-linear frequency shift and comparison to experimental data of [44]. Figures from [33].

data. The black dots are our experimental data and the red line is their fit to the data. The dotted line is the calculation when the non-linear term is not included. They showed that if they did not take into account the non-linearity, the linewidth decrease was smaller. Their calculations differ from our macrospin simulations in that they assume a non-linear damping coefficient, Q = 3. In our macrospin LLG simulations, we assume Q = 0, i.e. we only assume a constant Gilbert damping and no amplitude-dependent damping. The physical origin of the non-linear damping is not entirely clear, but presumably this can be a consequence of micromagnetic coupling effects (see next section, Section 3.4.8).

3.4.8 Micromagnetic Simulations

Whereas our macrospin simulations with no non-linear damping are unable to explain the large linewidth changes we measure, we find that micromagnetic calculations give better agreement. We performed simulations using the algo-

rithms described in Ref. [45], which integrate the Landau-Lifshitz-Gilbert equation for both magnetic layers and include a Slonczewski spin-torque term [46], the Oersted field from the current, the magnetic interaction between the layers, and fluctuating Langevin fields to model thermal fluctuations. The parameters used in the micromagnetic simulations for the exchange-biased sample are: H = 1000 Oe, exchange-bias field, H_{EB} = 360 Oe, 20° relative to the easy axis; free and fixed layer saturation magnetization M_S = 650 emu/cm^3, free layer damping α = 0.025; fixed layer damping = 0.2; temperature = 300 K, exchange constant = 1.3×10^{-6} erg/cm, GMR asymmetry parameter = 1.5, current polarization = 0.38, and computational cell size = $5 \times 5 \times 4$ nm^3. Each simulation spans 100 ns with a time step of 0.334 ps.

Figure 3.21(a) shows examples of the simulated resistance as a function of time for an exchange-biased sample. The corresponding spectral densities of the resistance oscillations are shown in Figure 3.21(b). We find that, due to thermal fluctuations at room temperature, there is no well-defined precessional peak in the simulated signal between $\theta_H = 0°$ and approximately 30°, consistent with our measurements. At $\theta_H = 30°$, we see only a broad second harmonic peak in the simulated spectrum but no first harmonic, because of the relatively small misalignment angle between the layers. The first harmonic appears in the simulation at $\theta_H = 45°$, and it has a linewidth of about 3.1 GHz. As θ_H is increased to 90°, the linewidth of the first harmonic decreases strongly, eventually reaching a minimum (FWHM) of 350 MHz. The minimum linewidth in the simulation is about twice as large as the minimum linewidth of 170 MHz observed at $\theta_H = 90°$ in the experiment for the same parameters (Figure 3.8(a)). The simulation predicts a factor of about 10 by which the linewidth narrows between the field angle at which a first harmonic peak becomes first resolvable in the simulation, i.e. at

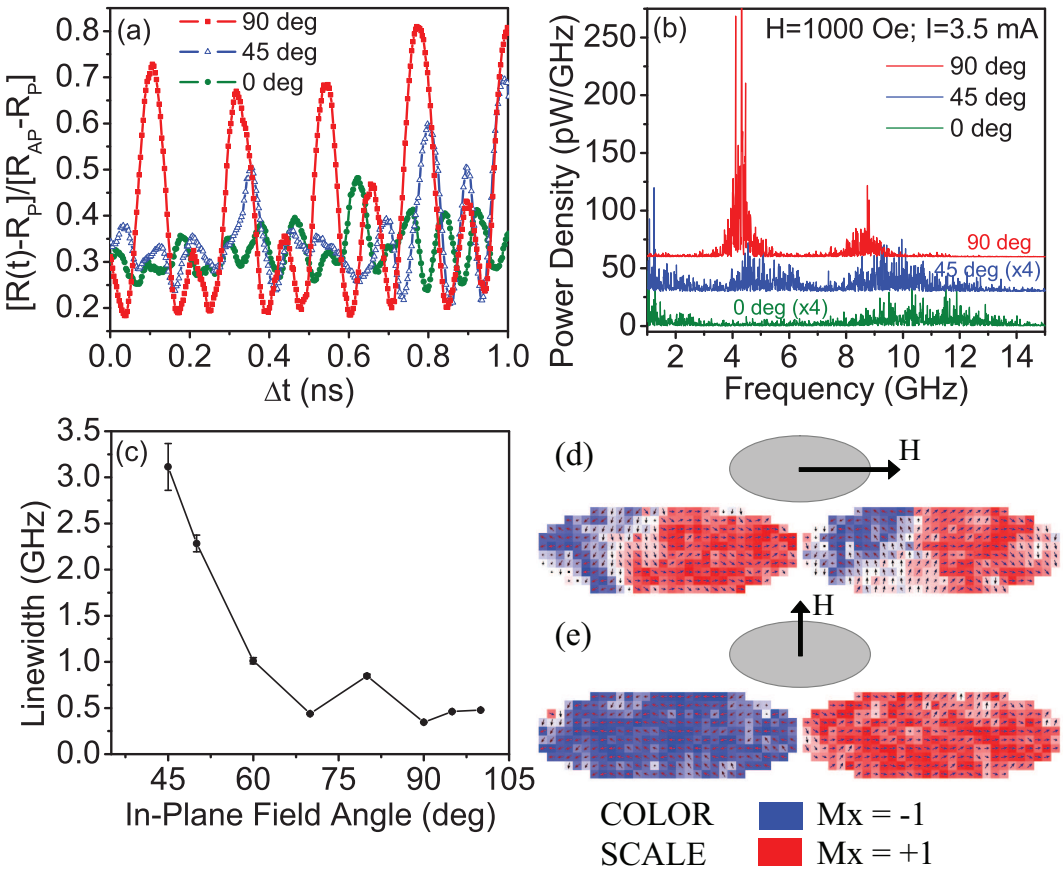


Figure 3.21: Micromagnetic simulations of the exchange-biased sample. (a) Resistance as a function of time. R_P is the resistance for parallel free and fixed magnetic layers, and R_{AP} corresponds to antiparallel layers. (b) Corresponding power spectral densities. The curves for $\theta_H = 45°$ and $90°$ are offset by 30 pW/GHz and 60 pW/GHz. The curves for $\theta_H = 0°$ and $45°$ are scaled by a factor of 4. (c) Calculated linewidth as a function of θ_H for $H = 1000$ Oe and $I = 3.5$ mA. (d,e) Snapshots of the magnetization distribution in the magnetic free layer for (d) $\theta_H = 0°$ and (e) $\theta_H = 90°$, at times corresponding to maxima in the precession cycle.

$\theta_H = 45°$, and $\theta_H = 90°$. This is close to the factor by which this peak narrows between $\theta_H = 45°$ and $90°$ in the experiment, but smaller than the factor of 20 by which it narrows between $\theta_H = 25°$ (the field angle at which the peak first becomes resolvable in the experiment) and $\theta_H = 90°$.

Similar simulations (not shown) for the thick-fixed-layer sample predict that the linewidth decreases from about 2.5 GHz at $\theta_H = 0°$ to about 530 MHz at $\theta_H = 90°$. The minimum linewidth in the simulation is quite close to the minimum linewidth of 450 MHz observed at $\theta_H = 90°$ in the experiment, and the factor of 5 by which the linewidth narrows is also close to the experimental value.

For both kinds of samples, the micromagnetic simulations suggest that the nature of the magnetization dynamics is qualitatively different for θ_H near $0°$ and $90°$. In Figures 3.21(d) and 3.21(e), we show snapshots of the spatial distribution of the magnetization in the free layer at $T = 300$ K for both field angles. The arrows in these plots represent the magnetization in the sample plane and the colors represent the magnetization component parallel to the long axis of the ellipse. For the case of $\theta_H = 0°$ (Figure 3.21(d)), the oscillations are spatially nonuniform and irregular, and the left and right halves of the ellipse can precess in opposite directions. Because different parts of the sample are not precessing together, this spatial incoherence produces temporal incoherence in the resistance signal, broadening the linewidth. In contrast, for the case of $\theta_H = 90°$ (Figure 3.21(e)), the dynamics are nearly spatially uniform, with the whole free layer precessing together in a spatially and temporally coherent manner, to give a precessional trajectory with a very well-defined frequency and a narrow linewidth. For angles near $\theta_H = 45°$ the magnetization undergoes ns-scale jumps between spatially nonuniform states and the state which is more spatially coherent.

Based on the micromagnetic simulations, we can consider the possible mechanisms underlying the crossover from spatially incoherent to coherent dynamics. One factor may be that the misalignment angle (θ_{mis}) between the fixed and free layer moments grows as θ_H is increased in the exchange-biased samples. When θ_{mis} is much larger than the range of angular variations within the micromagnetic configuration of the free layer, the spin torque on each spatial element will be in the same direction, and this may promote spatially-coherent motion [45]. Another important factor may be the amplitude of the precession. In Figure 3.21(a), we see that the amplitude of the oscillations is much smaller at $\theta_H = 0°$ and $\theta_H = 45°$ than at $\theta_H = 90°$. Smaller oscillation amplitudes make the dynamics more sensitive to thermal fluctuations in both amplitude and frequency [12]. A potential mechanism that does not appear to contribute to the crossover between spatially coherent and incoherent dynamics is the Oersted field from the applied current. We performed simulations with the Oersted field both included and absent, and found no significant qualitative differences in the dynamics.

3.5 Linewidths as a Function of Temperature

In order to further investigate the important mechanisms governing the linewidths in our spectra, we also studied the linewidths as a function of temperature at field angles where we observed the narrowest linewidths at room temperature, i.e. close to 90° (as we discussed in the previous sections). We conducted these temperature-dependence measurements in the CNS Janis cryostat as well as the 3-D Vector Magnet system (Section 2.2.5). In this section, we will discuss the measurements from one particular exchange-biased-fixed-layer de-

vice that showed very similar dV/dI and high-frequency characteristics as the device we discussed in the previous sections.

3.5.1 DC-Characterization

In Figure 3.22, we show the differential resistance for this device as a function of the magnetic field and current at room temperature when the field is applied close to 90°. In the magnetic field data (Figure 3.22(a)), the angle between the layers changes smoothly as the magnitude of the applied field is varied along 90 degrees, giving rise to a smooth change in resistance instead of an abrupt switching between parallel and anti-parallel. When the current is swept (Figure 3.22(b)), at low magnetic fields, we observe hysteretic switching between the parallel and anti-parallel states and at high magnetic fields, we observe signatures of dynamics.

3.5.2 Analysis as a Function of Temperature

In Figure 3.23, we show the results of the high-frequency DC-spectra as a function of temperature at H = 1150 Oe. The narrowest linewidths that we were able to observe were about 8.9 MHz at T = 10K and I = 4.0 mA (Figure 3.23(a)). This is compared to 135 MHz at T = 294K and I = 4.0 mA, which is close to the narrowest linewidths we observed for the previously discussed exchange-biased-fixed-layer sample under similar conditions (Figure 3.9(b)). In Figure 3.23(b)-(d), we have analyzed the linewidth, precession frequency and integrated power as a function of temperature at different currents. The linewidths increase with tem-

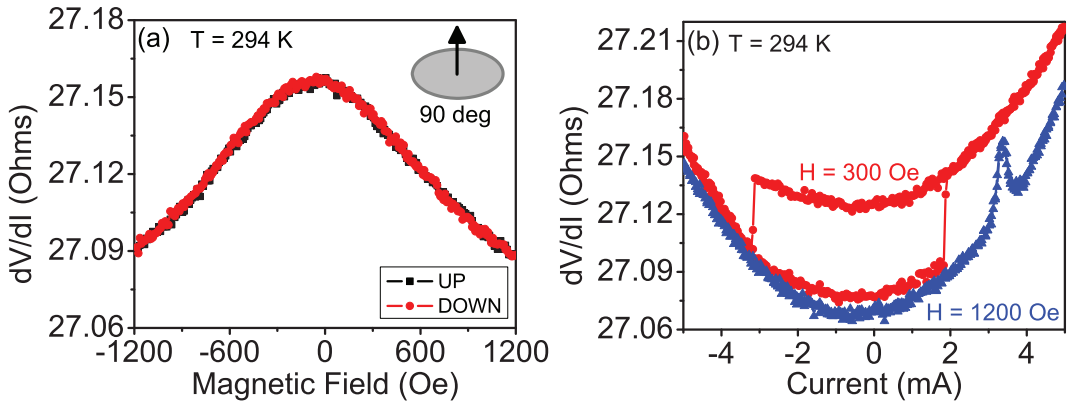


Figure 3.22: Differential resistance as a function of H and I at room temperature for a nanopillar spin valve device with an exchange-biased fixed layer that was cooled down for temperature-dependence measurements. (a) Resistance as a function of magnetic field for field along the in-plane hard axis. (b) Resistance as a function of current at H = 300 Oe and H = 1200 Oe.

perature at all currents, as expected, and these will be our main focus in this section. The precession frequency decreases with temperature at all currents. This is not surprising since the demagnetization field decreases with temperature, leading to a smaller effective field and smaller frequency. The frequencies also decrease with current, indicating that we are in the elliptical precession regime. The integrated power decreases quite dramatically with temperature, by almost a factor of 10. It is not clear why it decreases so rapidly. Micromagnetic effects might be in play, which might lead to the oscillations being even *more* spatially coherent at lower temperatures than at higher temperatures.

3.5.3 Modeling of Linewidths

We will now focus on the important mechanisms governing our linewidths. In order to do this, we fit the experimental linewidths according to the models discussed in Section 3.3. The first model takes into account amplitude and phase

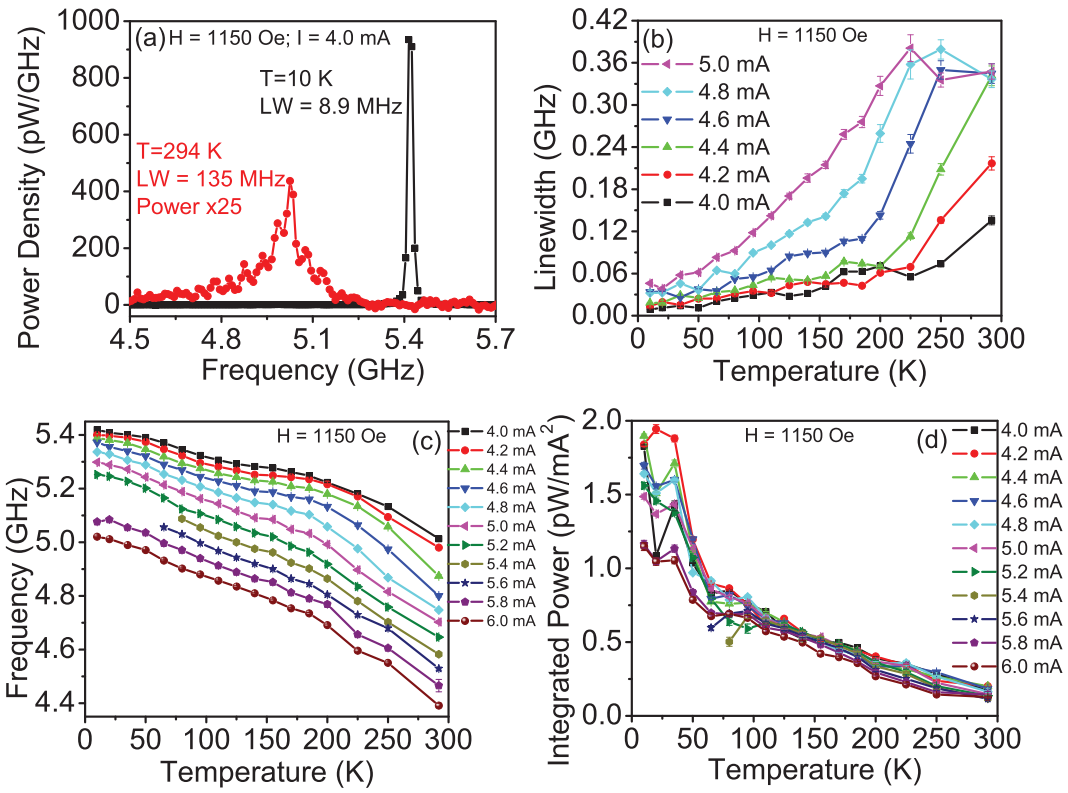


Figure 3.23: Analysis of the spin-torque-driven microwave signals as a function of temperature for an exchange-biased fixed layer sample at H = 1150 Oe and θ_H = 90°. (a) Power spectral density for I = 4.0 mA at T = 10 K and T = 294 K. (b) Linewidth. (c) Peak frequency. (d) Integrated power divided by I^2.

fluctuations (Section 3.3.1) and the second model takes into account thermally-activated hopping between different dynamical modes (Section 3.3.2). For amplitude and phase fluctuations, as we discussed in Section 3.3.1, Tiberkevich and Slavin calculated two different regimes for the temperature dependence of the linewidth. At low temperatures, their calculations predicted a linear temperature (T) dependence of the linewidth (Equation 3.8) and at higher temperatures, a square-root temperature ($\sqrt{T}$) dependence (Equation 3.10). We also discussed in Section 3.3.1 that Sankey et al. [12] found that the linewidths obtained from integrating the LLG equation varied as $\sqrt{T}$.

For our experimental data, we analyzed the linewidths by fitting to both a linear (T) and $\sqrt{T}$ term, and also added the contribution of thermally-activated hopping:

$$\Delta\omega = a\ T^{1/2}\ +\ \frac{f}{\pi} exp\left(\frac{-E_B}{k_B T}\right) = A\frac{df}{d\theta}\ T^{1/2}\ +\ \frac{f}{\pi} exp\left(\frac{-E_B}{k_B T}\right) \tag{3.12}$$

$$\Delta\omega = c\ T\ +\ \frac{f}{\pi} exp\left(\frac{-E_B}{k_B T}\right) \tag{3.13}$$

We fitted by adjusting 2 parameters: (i) a, (ii) $E_B/k_B T$ in Equation 3.12 and (i) c, (ii) $E_B/k_B T$ in Equation 3.13. The parameter "a" in Equation 3.12 is the same as $A df/d\theta$ in Sankey et al. [12].

In Figure 3.24, we show our experimental linewidths as well as a fit to the models discussed above. For a fit to Equation 3.12, we obtain $a = A df/d\theta$ = 2.3 ± 0.6 MHz$K^{-1/2}$ and $E_B/k_B T$ = 445 ± 54 K. These are in very good agreement with the fit parameters obtained in [12]: $A\ df/d\theta$ = 2.3 MHz$K^{-1/2}$ and $E_B/k_B T$ = 400 K, as well as in [35]. For a fit to Equation 3.13, we obtain c= 0.26 ± 0.05 MHz K and $E_B/k_B T$ = 642 ± 148 K. The fits do not appear to be too sensitive to the choice of the exponent (1 or 1/2) of the temperature.

We also tried to analyze the linewidths at lower temperatures and higher temperatures separately to determine which model is more important in each temperature range. In Figure 3.25, we show the experimental linewidths and the fits in the two temperature ranges. At lower temperatures (T < 160 K), we fitted the linewidths to '$a\ T^{1/2}$' and '$c\ T$' and adjusted the parameters "a" and "c", respectively. We obtained $a = A df/d\theta$ = 2.8 ± 0.14 MHz$K^{-1/2}$ and c = 0.27 ± 0.02 MHz K. Our data and fits are unable to distinguish between the T and $\sqrt{T}$ models.

At higher temperatures, we fitted the linewidths to '$f/\pi\ exp(-E_B/k_B T)$' and

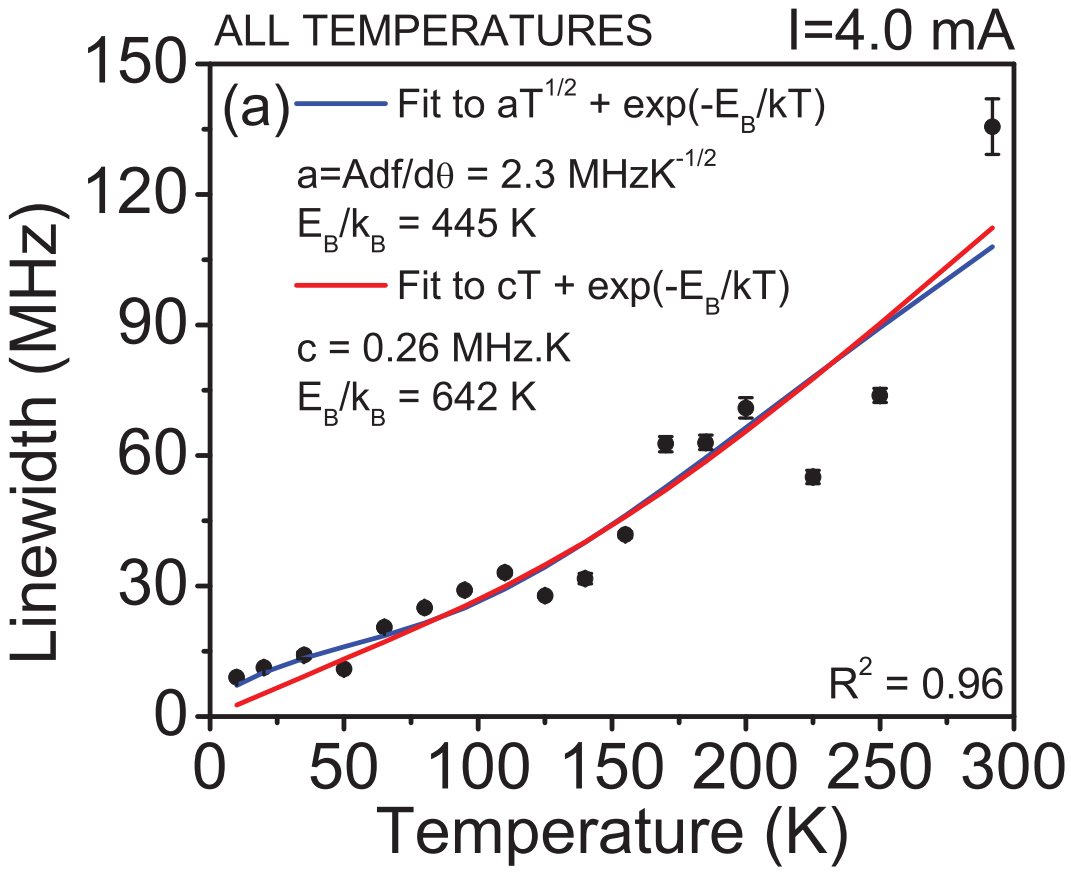


Figure 3.24: Modeling the temperature dependence of the linewidths. The circles are the experimental linewidths at H = 1150 Oe and I = 4.0 mA. The blue solid line is a fit to Equation 3.12 and the red solid line is a fit to Equation 3.13.

adjusted the parameter E_B/k_BT. We obtained E_B/k_BT = 309 ± 15 K. If we add the '$a\ T^{1/2}$' term to the higher temperature fit model (Equation 3.12), we obtain $a = Adf/d\theta$ = 1.9 ± 1.7 MHz$K^{-1/2}$ and E_B/k_BT = 415 ± 128 K. If we add the '$c\ T$' term to the higher temperature fit model (Equation 3.13), we obtain c= 0.24 ± 0.1 MHz K and E_B/k_BT = 574 ± 224 K. By adding the '$a\ T^{1/2}$' and '$c\ T$' terms to the thermally-activated model, we notice that the error bar on the fits becomes very high. If we remove these terms and fit the high-temperature data to just the thermally-activated term, the fit is better and the error bar is small (E_B/k_BT = 309 ± 15 K). This suggests that the thermally-activated model is sufficient to

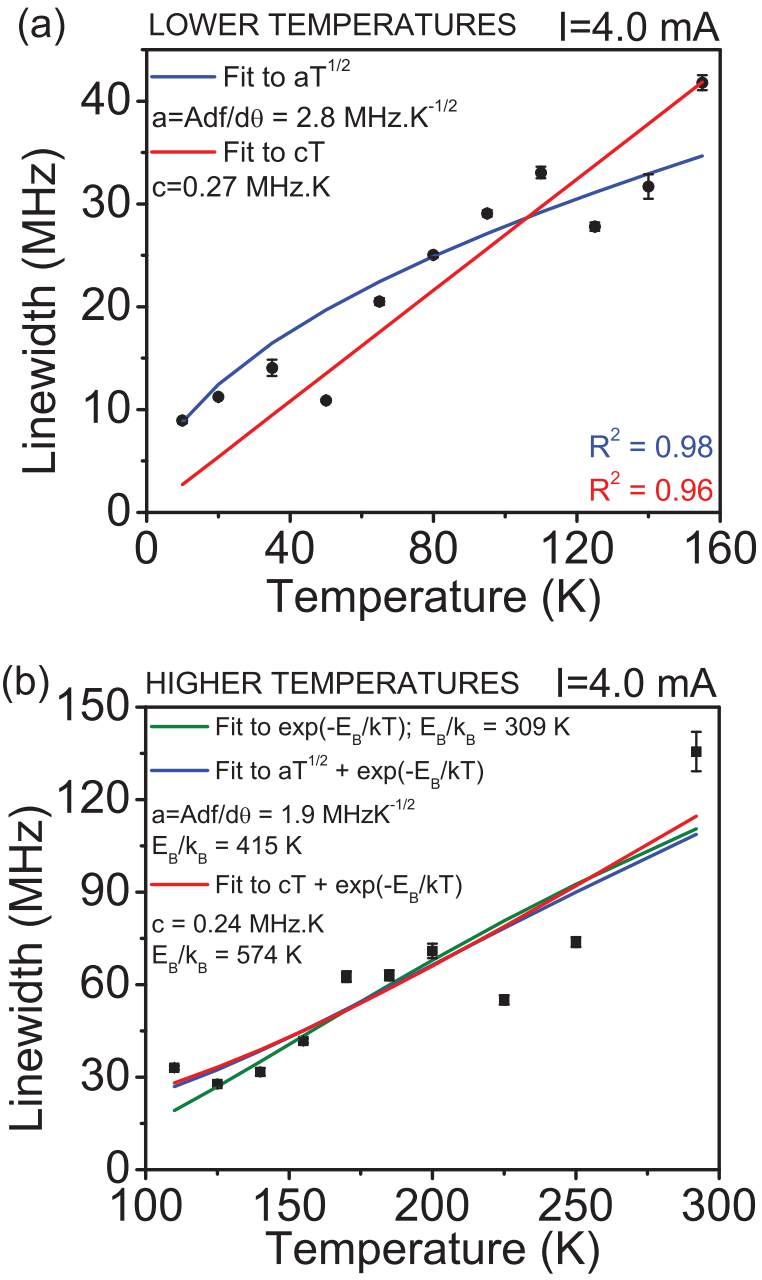


Figure 3.25: Analyzing the temperature dependence of the linewidths in the (a) lower temperature range (< 160 K) and (b) higher temperature range. The circles are the experimental linewidths at H = 1150 Oe and I = 4.0 mA. The olive solid line is a fit to Equation 3.11, the blue solid line is a fit to Equation 3.12, and the red solid line is a fit to Equation 3.13.

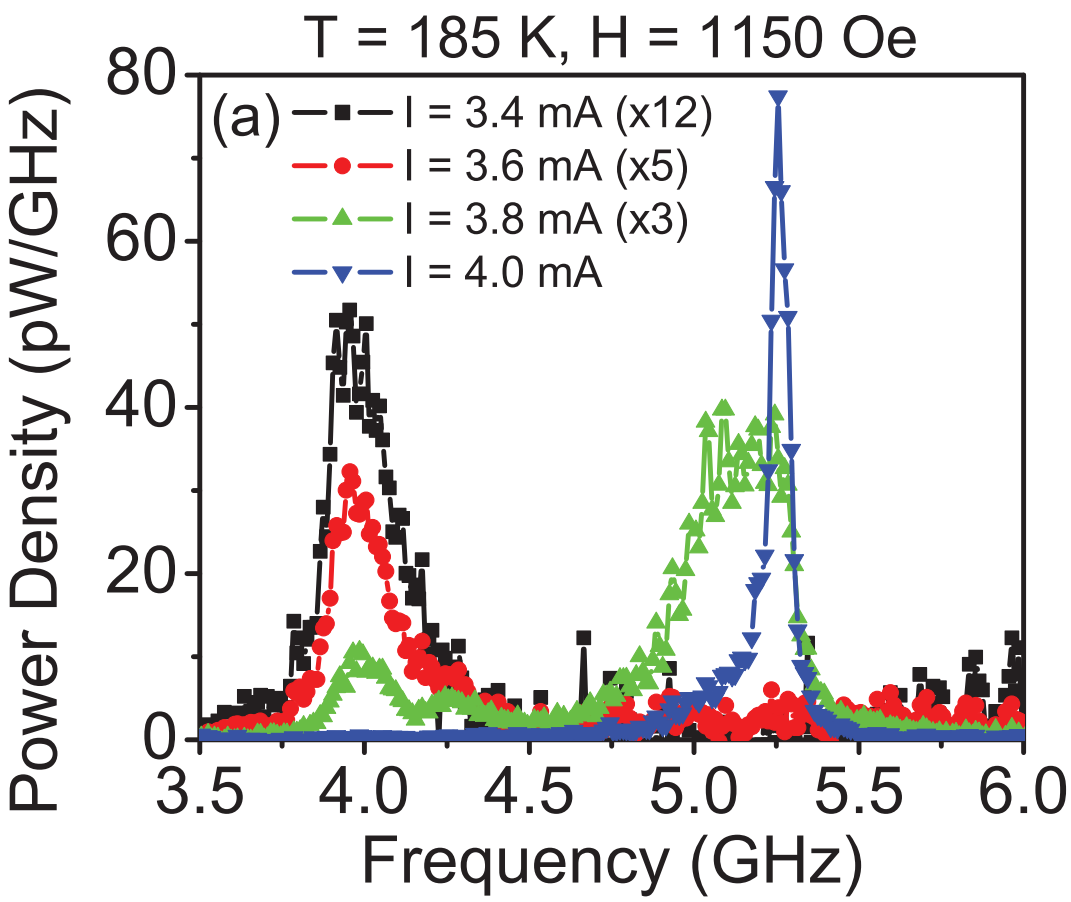


Figure 3.26: Example of power spectral density indicating hopping between different dynamical modes at T = 185 K and H = 1150 Oe.

explain the large linewidths at higher temperatures.

It should be pointed out that the effective barriers we obtain from the fits ($E_B/k_BT \approx$ 300 - 450K) are smaller than the effective barriers for static switching ($E_B/k_BT \approx 10^4 - 10^5$ K). This is not surprising, because in thermally-activated hopping between different dynamical modes, the precession states have different frequencies and different energies, but the difference between the energies of two dynamical states is not as large as the energy difference between static parallel and anti-parallel states. In Figure 3.26, we show an example of hopping between dynamical modes at T = 185 K. At I = 3.4 mA and I = 3.6 mA, there is a

precession mode at about 4 GHz. As we increase the current to I = 3.8 mA, we see two precession frequencies at about 4 GHz and 5 GHz. These correspond to two precession states very close in frequency. At I = 4.0 mA, the lower frequency peak disappears and the higher-frequency peak evolves into a very sharp peak at about 5.2 GHz.

Effect of heating

We also tried to take into account the effect of Joule heating due to the currents that we apply across the sample. We calculated the effective temperature as a function of the bath temperature at different currents in Figure 3.27(a), by using the equation in [47]:

$$T_{eff} = \sqrt{T^2 + \frac{3}{4}\left(\frac{e\,I\,R}{\pi\,k_B}\right)^2}, \tag{3.14}$$

where T_{eff} is the effective temperature, T is the bath temperature, I is the current and R is the resistance. We find that the lowest effective temperature, even at a bath temperature of 10 K, is probably not much less than 100 K. We plot the linewidths as a function of the effective temperature in Figure 3.27(b).

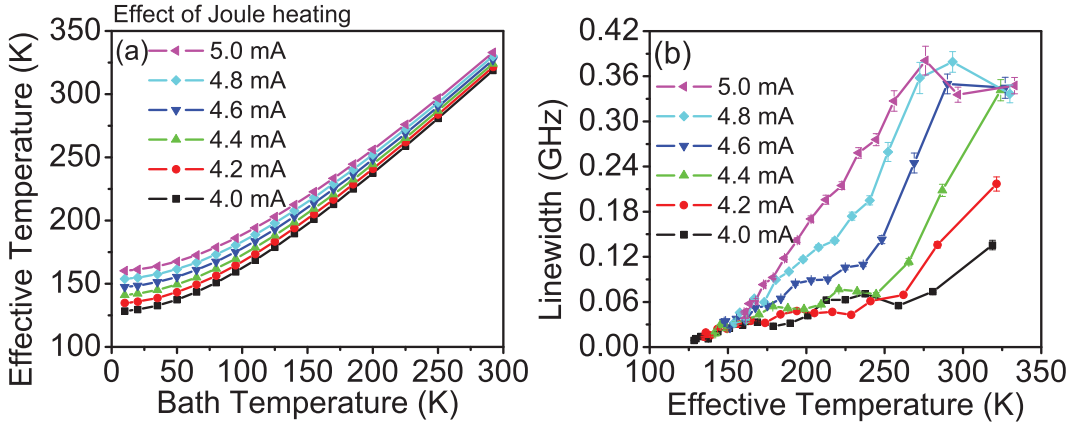


Figure 3.27: Calculation of effective temperature due to Joule heating. (a) Calculated effective temperature as a function of bath temperature for different I. (b) Linewidths as a function of the effective temperature at different I and H = 1150 Oe.

3.5.4 Macrospin Simulations as a Function of Temperature

We conducted macrospin simulations as a function of temperature at two different field angles, $\theta_H = 10^\circ$ and $\theta_H = 80^\circ$ (we did not perform simulations at $\theta_H = 0^\circ$ and $\theta_H = 90^\circ$ in order to avoid singularities during the integration of the LLG equation). These were performed by integrating the Landau-Lifshitz-Gilbert equation for both magnetic layers and included a Slonczewski spin-torque term, the magnetic interaction between the layers, and fluctuating Langevin fields to model thermal fluctuations (Section 2.3.1). The parameters used in the macrospin simulations for the exchange-biased sample were: H = 1000 Oe, exchange-bias field, H_{EB} = 360 Oe, 1° relative to the easy axis; H_{dipole} due to the fixed layer on the free layer = 100 Oe, H_{dipole} due to the free layer on the fixed layer = 100 Oe, $H_{anisotropy}$ of fixed and free layers = 200 Oe; thickness of free layer = 4 nm; thickness of fixed layer = 4 nm; area = 50×150 nm^2; free and fixed layer saturation magnetization M_S = 560 emu/cm^3, free layer damping α = 0.01 (we did not take into account any non-linear damping); fixed layer damping = 0.1. Each simulation spanned 200 ns with a time step of 1 ps.

Figures 3.28(a) and (c) show the spectra at T = 10 K and T = 250 K for field angles along $\theta_H = 10^\circ$ and $\theta_H = 80^\circ$, and Figures 3.28(b) and (d) show the corresponding linewidths calculated directly from the Fourier Transform of the oscillating GMR at the two field angles. We can see that at $\theta_H = 10^\circ$ (Figure 3.28(a)), the simulation correctly predicts a large second harmonic and a very small first harmonic, because of the small misalignment angle between the magnetic layers. At $\theta_H = 80^\circ$ (Figure 3.28(c)), the simulation shows a large first harmonic and second harmonic due to the large misalignment angle between the magnetic layers. In Figures 3.28(b) and (d), we see that the simulated linewidths increase

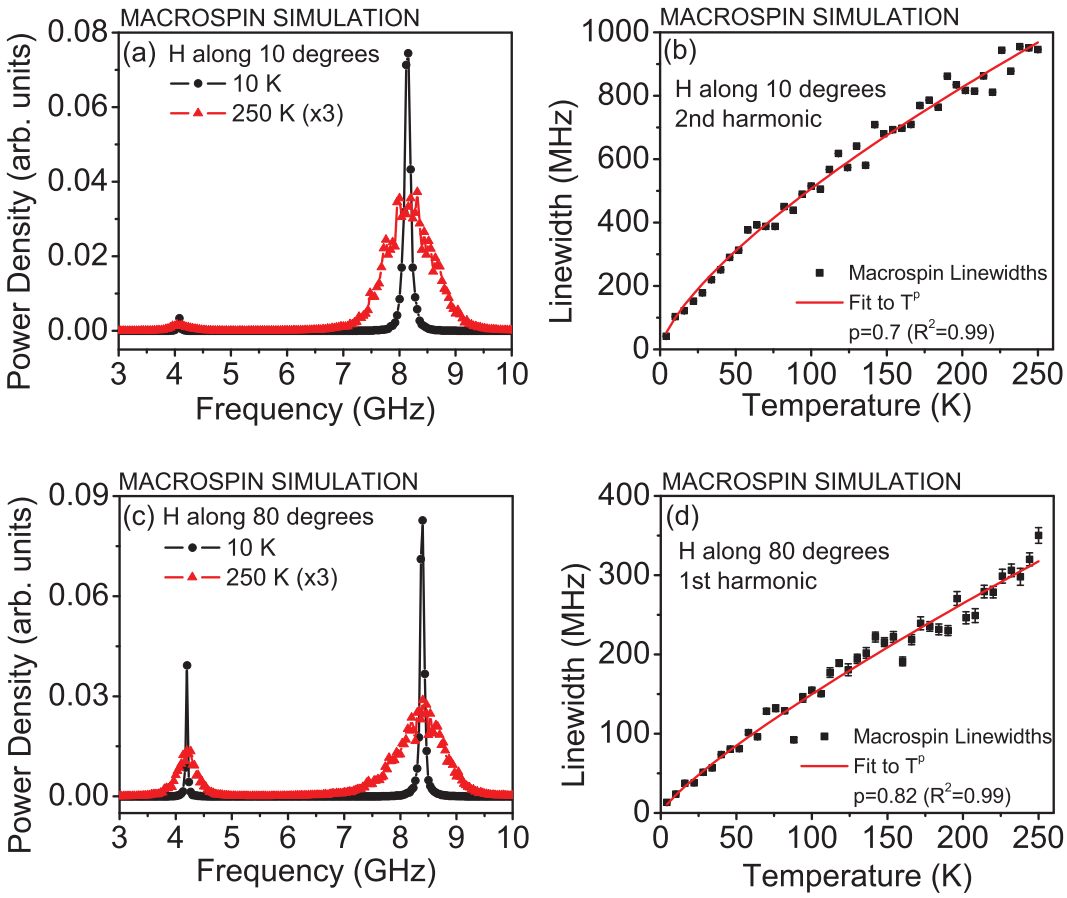


Figure 3.28: Simulated power spectral density and linewidths as a function of temperature for $\theta_H = 10°$ and $\theta_H = 80°$. (a) Simulated power spectral density for $H = 1000$ Oe and $\theta_H = 10°$ at $T = 10$K and $T = 250$K. (b) Simulated linewidths of the second harmonic as a function of temperature at $H = 1000$ Oe and $\theta_H = 10°$ (c) Simulated power spectral density for $H = 1000$ Oe and $\theta_H = 80°$ at $T = 10$K and $T = 250$K. (d) Simulated linewidths of the first harmonic as a function of temperature at $H = 1000$ Oe and $\theta_H = 80°$.

with temperature. We fit the linewidths to a T^p model by adjusting the exponent, "p" of the temperature. We obtained $p = 0.7$ for the linewidths at $\theta_H = 10°$ and $p = 0.82$ for the linewidths at $\theta_H = 80°$. The value of "p" in both cases is close to 0.5 obtained by Sankey et al. [12]. We suggest that the discrepancy between our exponent and Sankey et al. might be due to the fact that we did not attempt to adjust the current at different temperatures to keep the amplitude

always constant.

3.5.5 Conclusions for Temperature Dependence of Linewidths

In conclusion, the temperature dependence of our experimental linewidths can be explained by a combination of amplitude and phase fluctuations and thermally-activated hopping. At lower temperatures, the linewidths are affected more strongly by amplitude and phase fluctuations. Our fits are unable to distinguish between the linear T and $\sqrt{T}$ dependence. At higher temperatures, the linewidths increase more rapidly due to thermally-activated hopping between different dynamical modes.

3.6 Comparing Our Minimum Linewidths to Previous Spin Torque Oscillator Studies

The minimum linewidths achieved by us at room temperature were 40 MHz for fields applied along the in-plane hard axis (at lower temperatures, T = 10 K, we obtained linewidths of 8.9 MHz). This is among the narrowest room-temperature linewidths observed for nanopillar devices in which the free layer moves approximately as a single magnetic domain. We are aware of only one report of a narrower linewidth in this category - a 21 MHz linewidth in a MgO tunnel-junction device [Nazarov et al [48]]. Narrower lines (down to 7 MHz) have been seen at higher currents in all-metal nanopillars, but these signals have been identified with fixed-layer excitations or coupled motion of free and fixed layers [9]. In other experiments on free-layer oscillations in metallic nanopillars,

Sankey et al [12] reported a minimum room-temperature linewidth of 250 MHz, Mistral et al [14] observed linewidths below 10 MHz at 225 K, but did not report room-temperature results, and Houssameddine et al [16] reported 50 MHz lines in nanopillars with perpendicularly-polarized fixed layers, but this paper never stated whether the measurements were done at low temperature or room temperature.

In point-contact devices, linewidths of approximately 2 MHz have been obtained [Rippard et al [7], [15]]. Nanopillar samples in which spin torque drives gyromagnetic oscillations of a magnetic vortex have achieved very narrow linewidths of approximately 300 kHz [Pribiag et al [17]]. Vortex oscillations in point-contact devices have been measured with a linewidth of 576 kHz [Pufall et al [49]].

3.7 Conclusions

We observe that applying a magnetic field along the hard in-plane axis of a magnetic nanopillar device, so as to offset the precession axis of the free layer away from the orientation of the exchange-biased fixed layer, can produce a dramatic reduction in the linewidth of the spin-torque-driven dynamics excited by a DC current. Based on micromagnetic simulations, we associate this reduction with a crossover from spatially nonuniform magnetization dynamics to spatially coherent precession. This ability to control the spatial uniformity of the magnetization dynamics should help in the development of spin-torque nano-oscillators for use as microwave sources. Our results also suggest that large device-to-device variations in linewidths measured previously [3, 8, 9, 12]

may be associated with variations in the angle of the exchange bias relative to the field direction.

The temperature dependence of our experimental linewidths can be explained by a combination of amplitude and phase fluctuations and thermally-activated hopping. At lower temperatures, the linewidths are affected more strongly by amplitude and phase fluctuations. Our fits are unable to distinguish between the linear T and $\sqrt{T}$ dependence. At higher temperatures, the linewidths increase more rapidly due to thermally-activated hopping between different dynamical modes.

REFERENCES

[1] Slonczewski J.C., Current-driven excitation of magnetic multilayers, *J. Magn. Magn. Mater.* **159**, L1 (1996).

[2] Berger L., Emission of spin waves by a magnetic multilayer traversed by a current, *Phys. Rev. B* **54**, 9353 LP (1996).

[3] Kiselev S.I., Sankey J.C., Krivorotov I.N., Emley N.C., Schoelkopf R.J., Buhrman R.A., & Ralph D.C., Microwave oscillations of a nanomagnet driven by a spin-polarized current, *Nature* **425**, 380 (2003).

[4] Rippard W.H., Pufall M.R., Kaka S., Russek S.E., & Silva T.J., Direct-current induced dynamics in co[sub 90]fe[sub 10]/ni[sub 80]fe[sub 20] point contacts, *Phys. Rev. Lett.* **92**, 027201 (2004).

[5] Covington M., AlHajDarwish M., Ding Y., Gokemeijer N.J., & Seigler M.A., Current-induced magnetization dynamics in current perpendicular to the plane spin valves, *Phys. Rev. B* **69**, 184406 (2004).

[6] Kiselev S.I., Sankey J.C., Krivorotov I.N., Emley N.C., Rinkoski M., Perez C., Buhrman R.A., & Ralph D.C., Current-induced nanomagnet dynamics for magnetic fields perpendicular to the sample plane, *Phys. Rev. Lett.* **93**, 036601 (2004).

[7] Rippard W.H., Pufall M.R., Kaka S., Silva T.J., & Russek S.E., Current-driven microwave dynamics in magnetic point contacts as a function of applied field angle, *Phys. Rev. B* **70**, 100406 (2004).

[8] Krivorotov I.N., Emley N.C., Sankey J.C., Kiselev S.I., Ralph D.C., & Buhrman R.A., Time-domain measurements of nanomagnet dynamics driven by spin-transfer torques 10.1126/science.1105722, *Science* **307**, 228 (2005).

[9] Kiselev S.I., Sankey J.C., Krivorotov I.N., Emley N.C., Garcia A.G.F., Buhrman R.A., & Ralph D.C., Spin-transfer excitations of permalloy nanopillars for large applied currents, *Phys. Rev. B* **72**, 064430 (2005).

[10] Kaka S., Pufall M.R., Rippard W.H., Silva T.J., Russek S.E., & Katine J.A., Mutual phase-locking of microwave spin torque nano-oscillators, *Nature* **437**, 389 (2005).

[11] Mancoff F.B., Rizzo N.D., Engel B.N., & Tehrani S., Phase-locking in double-point-contact spin-transfer devices, *Nature* **437**, 393 (2005).

[12] Sankey J.C., Krivorotov I.N., Kiselev S.I., Braganca P.M., Emley N.C., Buhrman R.A., & Ralph D.C., Mechanisms limiting the coherence time of spontaneous magnetic oscillations driven by dc spin-polarized currents, *Phys. Rev. B* **72**, 224427 (2005).

[13] Nazarov A.V., Olson H.M., Cho H., Nikolaev K., Gao Z., Stokes S., & Pant B.B., Spin transfer stimulated microwave emission in mgo magnetic tunnel junctions, *Appl. Phys. Lett.* **88**, 162504 (2006).

[14] Mistral Q., Kim J.V., Devolder T., Crozat P., Chappert C., Katine J.A., Carey M.J., & Ito K., Current-driven microwave oscillations in current perpendicular-to-plane spin-valve nanopillars, *Appl. Phys. Lett.* **88**, 192507 (2006).

[15] Rippard W.H., Pufall M.R., & Russek S.E., Comparison of frequency, linewidth, and output power in measurements of spin-transfer nanocontact oscillators, *Phys. Rev. B* **74**, 224409 (2006).

[16] Houssameddine D., Ebels U., Delaet B., Rodmacq B., Firastrau I., Ponthenier F., Brunet M., Thirion C., Michel J.P., Prejbeanu-Buda L., Cyrille M.C., Redon O., & Dieny B., Spin-torque oscillator using a perpendicular polarizer and a planar free layer, *Nature Materials* **6**, 447 (2007).

[17] Pribiag V.S., Krivorotov I.N., Fuchs G.D., Braganca P.M., Ozatay O., Sankey J.C., Ralph D.C., & Buhrman R.A., Magnetic vortex oscillator driven by d.c. spin-polarized current, *Nature Physics* **3**, 498 (2007).

[18] Russek S.E., Kaka S., Rippard W.H., Pufall M.R., & Silva T.J., Finite-temperature modeling of nanoscale spin-transfer oscillators, *Phys. Rev. B* **71**, 104425 (2005).

[19] Kim J.V., Stochastic theory of spin-transfer oscillator linewidths, *Phys. Rev. B* **73**, 174412 (2006).

[20] Kim J.V., Tiberkevich V., & Slavin A.N., Generation linewidth of an auto-oscillator with a nonlinear frequency shift: Spin-torque nano-oscillator, *Phys. Rev. Lett.* **100**, 017207 (2008).

[21] Serpico C., Bertotti G., Bonin R., d'Aquino M., & Mayergoyz I.D., Power

spectrum of current-induced magnetization dynamics in uniaxial nanomagnets, *J. Appl. Phys.* **101**, 09A507 (2007).

[22] Mizushima K., Kudo K., & Sato R., Phase and amplitude noise spectra in spin-transfer nano-oscillators, *J. Appl. Phys.* **101**, 113903 (2007).

[23] Mizushima K., Nagasawa T., Kudo K., Saito Y., & Sato R., Decrease of nonlinearity and linewidth narrowing in spin-transfer oscillators under the external field applied near the hard axis, *Appl. Phys. Lett.* **94**, 152501 (2009).

[24] Sato R., Saito Y., & Mizushima K., Current-dependent linewidth of a spin-transfer nano-oscillator, *J. Magn. Magn. Mater.* **321**, 990 (2009).

[25] Boone C., Katine J.A., Childress J.R., Zhu J., Cheng X., & Krivorotov I.N., Experimental test of an analytical theory of spin-torque-oscillator dynamics, *Phys. Rev. B* **79**, 140404 (2009).

[26] Keller M.W., Kos A.B., Silva T.J., Rippard W.H., & Pufall M.R., Time domain measurement of phase noise in a spin torque oscillator, *Appl. Phys. Lett.* **94**, 193105 (2009).

[27] Kudo K., Nagasawa T., Sato R., & Mizushima K., Measurement of nonlinear frequency shift coefficient in spin-torque oscillators based on mgo tunnel junctions, *Appl. Phys. Lett.* **95**, 022507 (2009).

[28] Georges B., Grollier J., Cros V., Fert A., Fukushima A., Kubota H., Yakushijin K., Yuasa S., & Ando K., Origin of the spectral linewidth in non linear oscillators based on mgo tunnel junctions, *arXiv:0904.0880v1* (2009).

[29] Houssameddine D., Ebels U., Dieny B., Garello K., Michel J.P., Delaet B., Viala B., Cyrille M.C., Katine J.A., & Mauri D., Temporal coherence of mgo based magnetic tunnel junction spin torque oscillators, *Phys. Rev. Lett.* **102**, 257202 (2009).

[30] Sankey J.C., Braganca P.M., Garcia A.G.F., Krivorotov I.N., Buhrman R.A., & Ralph D.C., Spin-transfer-driven ferromagnetic resonance of individual nanomagnets, *Phys. Rev. Lett.* **96**, 227601 (2006).

[31] Ham D., Andress W., & Ricketts D., Phase noise in oscillators (invited paper), in *International Workshop on SiP/SoC Integration of MEMS and Passive Components with RF-ICs* (2004).

[32] Tiberkevich V.S., Slavin A.N., & Kim J.V., Temperature dependence of nonlinear auto-oscillator linewidths: Application to spin-torque nano-oscillators, *Phys. Rev. B* **78**, 092401 (2008).

[33] Tiberkevich V., Krivorotov I., Gerhart G., & Slavin A., Compensation of nonlinear phase noise in an in-plane-magnetized anisotropic spin-torque oscillator, *J. Magn. Magn. Mater.* **321**, L53 (2009).

[34] Slavin A. & Tiberkevich V., Nonlinear auto-oscillator theory of microwave generation by spin-polarized current, *IEEE Trans. Magnetics* **45**, 1875 (2009).

[35] Pufall M.R., Rippard W.H., Kaka S., Russek S.E., Silva T.J., Katine J., & Carey M., Large-angle, gigahertz-rate random telegraph switching induced by spin-momentum transfer, *Phys. Rev. B* **69**, 214409 (2004).

[36] Krivorotov I.N., Emley N.C., Buhrman R.A., & Ralph D.C., Time-domain studies of very-large-angle magnetization dynamics excited by spin transfer torques, *Phys. Rev. B* **77**, 054440 (2008).

[37] Fabian A., Terrier C., Guisan S.S., Hoffer X., Dubey M., Gravier L., Ansermet J.P., & Wegrowe J.E., Current-induced two-level fluctuations in pseudo-spin-valve (co/cu/co) nanostructures, *Phys. Rev. Lett.* **91**, 257209 (2003).

[38] Machlup S., Noise in semiconductors: Spectrum of a two-parameter random signal, *J. Appl. Phys.* **25**, 341 (1954).

[39] Emley N.C., *Magnetic Multilayer Nanopillars for the Study of Current-Induced Reversal of a Thin Magnetic Layer*, Ph.d., Cornell University (2005).

[40] Albert F., *The fabrication and measurement of current perpendicular to the plane magnetic nanostructures for the study of the spin-transfer effect*, Ph.d., Cornell University (2003).

[41] http://www.gmw.com/electromagnets/Miniature/5201/5201.html.

[42] Tulapurkar A.A., Suzuki Y., Fukushima A., Kubota H., Maehara H., Tsunekawa K., Djayaprawira D.D., Watanabe N., & Yuasa S., Spin-torque diode effect in magnetic tunnel junctions, *Nature* **438**, 339 (2005).

[43] McMichael R.D. & Stiles M.D., Magnetic normal modes of nanoelements, *J. Appl. Phys.* **97**, 10J901 (2005).

[44] Thadani K.V., Finocchio G., Li Z.P., Ozatay O., Sankey J.C., Krivorotov I.N., Cui Y.T., Buhrman R.A., & Ralph D.C., Strong linewidth variation for spin-torque nano-oscillators as a function of in-plane magnetic field angle, *Phys. Rev. B* **78**, 024409 (2008).

[45] Finocchio G., Krivorotov I.N., Torres L., Buhrman R.A., Ralph D.C., & Azzerboni B., Magnetization reversal driven by spin-polarized current in exchange-biased nanoscale spin valves, *Phys. Rev. B* **76**, 174408 (2007).

[46] Slonczewski J.C., Currents and torques in metallic magnetic multilayers, *J. Magn. Magn. Mater.* **247**, 324 (2002).

[47] Krivorotov I.N., Emley N.C., Garcia A.G.F., Sankey J.C., Kiselev S.I., Ralph D.C., & Buhrman R.A., Temperature dependence of spin-transfer-induced switching of nanomagnets, *Phys. Rev. Lett.* **93**, 166603 (2004).

[48] Nazarov A.V., Nikolaev K., Gao Z., Cho H., & Song D., Microwave generation in mgo magnetic tunnel junctions due to spin transfer effects (invited), *J. Appl. Phys.* **103**, 07A503 (2008).

[49] Pufall M.R., Rippard W.H., Schneider M.L., & Russek S.E., Low-field current-hysteretic oscillations in spin-transfer nanocontacts, *Phys. Rev. B* **75**, 140404 (2007).

CHAPTER 4

SPIN-TORQUE EFFECTS ON THE EXCHANGE-BIAS OF ANTIFERROMAGNET/FERROMAGNET BILAYERS

4.1 Review of Antiferromagnets & Exchange-Bias

Antiferromagnets (AFM's) are commonly used in magnetic sensors to pin the magnetization of a ferromagnet (FM) in a particular direction by interfacial exchange coupling. This "exchange-bias" phenomenon leads to a unidirectional anisotropy and enhanced coercivity in the ferromagnet. Different models have been proposed to try and explain the origin of this exchange-coupling [1, 2, 3, 4, 5, 6] and the predictions of these models depend on whether the net spin moment at the antiferromagnet / ferromagnet interface is *compensated* or *uncompensated* (Figure 4.1). The net moment of the entire bulk of an antiferromagnet is zero; the compensation of spins just refers to the relative orientation of the spins in the interfacial layer of the antiferromagnet. If all the spins in one particular layer of the antiferromagnet are in the same orientation relative to each other but are in the opposite orientation with respect to all other spins in the subsequent layer, then the antiferromagnet interface is said to be *uncompensated*, since the layer right next to the interface has a net moment even though the bulk net moment of the antiferromagnet is zero (Figure 4.1(a)). On the other hand, if the spins in one particular layer of the antiferromagnet are all alternatively in the opposite orientation, then the antiferromagnet interface is said to be *compensated*, since the layer right next to the interface has no net moment (Figure 4.1(b)).

In reality, perfectly uncompensated antiferromagnet/ferromagnet interfaces

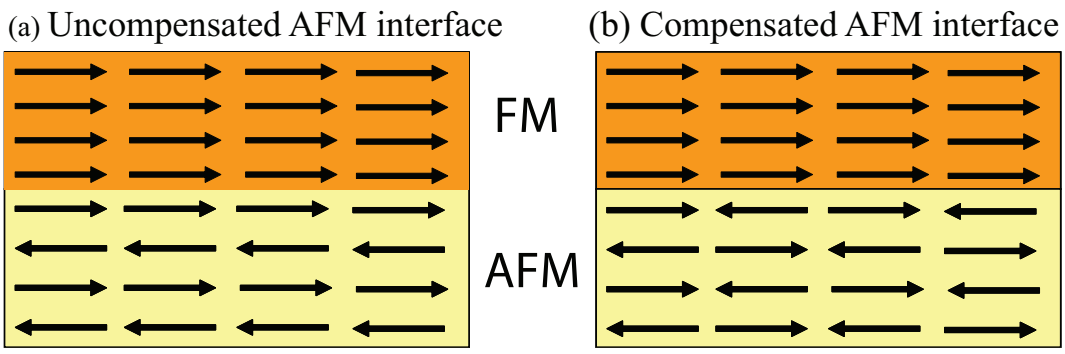


Figure 4.1: Cartoon of uncompensated and compensated antiferromagnet / ferromagnet interfaces.

require atomically flat antiferromagnets and are hard to realize experimentally. Most ferromagnet / antiferromagnet interfaces are rough and are either partially uncompensated or fully compensated. Fully compensated antiferromagnet interfaces have exchange-bias because of roughness-induced randomness in the number of spins of each sub-lattice at the antiferromagnet / ferromagnet interface. Consequently, different local regions of the interface have more spins of one sub-lattice than the other, leading to the formation of antiferromagnetic domains perpendicular to the ferromagnet / antiferromagnet interface that can lead to some uncompensated spins at the interface even if the interface is mostly compensated, thereby creating exchange-bias [3]. This random field model is able to predict the correct order of magnitude of the hysteretic loop shift due to the unidirectional anisotropy.

4.2 Spin-Torque Effects in Antiferromagnets

In order to think of spin-transfer torques in an antiferromagnet, we can intuitively see that there would be fundamental differences from when the spin-

torque acts on a ferromagnet. In the case of a ferromagnet, the spins inside the ferromagnet are locked together and the spin-transfer torque does not change the *relative* orientations of the different spins inside the ferromagnet. In fact, the spin-transfer torque essentially acts on the overall net orientation of all the spins. In the case of an antiferromagnet, however, there are two sub-lattices of opposite spins involved and so a spin-transfer torque on any particular layer of the antiferromagnet could then affect the relative orientation of all subsequent layers in the antiferromagnet because of the strong exchange-energy that warrants the net spin-moment of the antiferromagnet to be zero. Consequently, in the case of an antiferromagnet, it is the *difference* between the sums of the torques over the two opposite sub-lattices that becomes important [7]. This can lead to the two sub-lattices moving relative to each other or the two sub-lattices moving together (but still opposite relative to each other) leading to a rotation of the average direction of the antiferromagnet order parameter. The second effect is the one that becomes important for antiferromagnetic giant magnetoresistance (AGMR), i.e. the analog of GMR that depends on the relative alignment of two antiferromagnets instead of two ferromagnets [8, 9].

4.2.1 Theoretical Predictions of Spin-Torque Effects in Antiferromagnets

Theories have suggested that torque from a spin-polarized current crossing through an antiferromagnet/ferromagnet interface might alter the structure of the antiferromagnet, thereby affecting the exchange-bias field produced by it on the adjacent ferromagnetic layer [8, 10, 11, 12].

In particular, Haney et al. [10] have calculated that the spin-torque on a ferromagnet due to a compensated antiferromagnet with 2-fold symmetry has the form of $\sin 2\theta$ instead of $\sin \theta$ from another ferromagnet (as discussed in earlier chapters). Their calculations indicate that for electrons flowing from an AFM to a FM, the spin-torque tends to align the FM direction parallel with the AFM axis and tends to align the AFM axis perpendicular to the FM direction in the same plane. The reverse is true for electrons flowing from a FM to an AFM: in this case, the spin-torque tends to align the AFM axis parallel to the FM direction and tends to align the FM direction perpendicular to the AFM axis in their common plane. They summarized these results by saying that spin-torque tends to align the orientation of the "downstream" material parallel with the "upstream" material while it tends to align the orientation of the "upstream" material perpendicular to the "downstream" material.

Haney and co-workers then calculated the implications of a $\sin 2\theta$ torque by integrating it into the LLG equation and found an interesting result. Assuming that the AFM axis (along $\widehat{z}$) is in the same direction and the same easy plane ($\widehat{y} - \widehat{z}$ plane) as the ferromagnet (Figure 4.2(a)), a spin-torque for the case of electrons flowing from the FM to the AFM would cause the FM direction to align perpendicular to the AFM axis (along $\widehat{y}$) but still in the common plane (as discussed in the previous paragraph). As the FM precesses, the spin-torque has a component that pushes the FM out-of-plane (i.e. in the $\widehat{x}$ direction); if the torque is large enough, then the stable configuration of the FM is out-of-plane (Figure 4.2(a)). Their results are summarized in the color plot (Figure 4.2(b)). In this Figure, "hc1" is a dimensionless quantity proportional to the spin-transfer torque. $hc1 < 0$ corresponds to electrons flowing from the FM to AFM; we can see that for this configuration that at small magnetic fields ("h"), the spin-torque

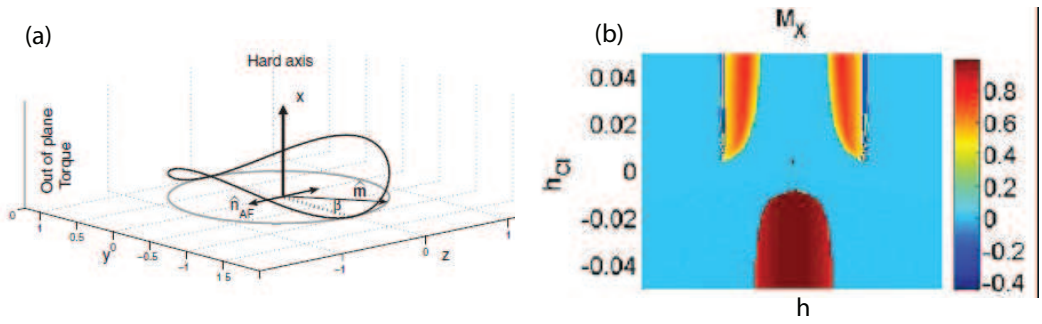


Figure 4.2: Theoretical predictions of the spin-transfer torque in antiferromagnets. Figure from Reference [10]. (a) Trajectory of the free-layer magnetization due to the out-of-plane torque from an antiferromagnet. (b) Color plot of M_X, out-of-plane component of the magnetization, as a function of the current and magnetic field.

pushes the FM out-of-plane as evidenced by the large M_X component.

We would like to point out that the most commonly studied metallic antiferromagnets, such as IrMn and FeMn, do not have the 2-fold symmetry that is assumed in the theoretical models described above. Instead these antiferromagnets have an average tetrahedral symmetry.

4.2.2 Previous Experiments of Spin-Torque Effects in Antiferromagnets

Some recent experiments have claimed to observe an effect on magnetic switching in antiferromagnet / ferromagnet bilayers [13, 14, 15, 16, 17]. The device geometries and results for each are summarized below (all thicknesses in nm):

In [13] and [17], Wei et al studied FeMn / CoFe bilayers and IrMn / CoFe bilayers, respectively, in a point-contact geometry. In their device geometries,

the CoFe layer (3 nm) was pinned by an antiferromagnet (FeMn or IrMn, 3 nm and 8 nm) and a second CoFe layer (10 nm or 3 nm) was unpinned and separated by a 10 nm copper spacer. They applied very large current densities (10^8 A/cm^2) perpendicular to the plane of the samples (CPP) by employing a point-contact geometry. They measured GMR versus field scans for their devices at different currents between -35 mA to +35 mA. They found that the offset and width of the hysteresis resistance loop corresponding to the pinned magnetic layer switching changed with current (Figure 4.3(a)). Since the offset of the hysteresis loop corresponds to the magnitude of the exchange-bias, they concluded that the exchange-bias changes with current. In particular, for their devices, negative currents (electrons from FM to AFM) increased the exchange-bias and positive currents (electrons from AFM to FM) decreased the exchange-bias (Figure 4.3(b)).

In [14], Urazhdin et al. studied FeMn / Py bilayers in a nanopillar geometry. In their device geometry, the Py layer (5 nm) was pinned by FeMn (1.5 - 4 nm) and a second Py layer (30 nm) was unpinned and separated by a 10 nm copper spacer. They applied current pulses upto ±20 mA perpendicular to the plane (CPP) of the nanopillar devices at large fields (H = +3000 or -3000 Oe) and then measured the exchange-bias from the hysteresis loop at small currents. Their results are summarized in Figure 4.3(c). They found that when the magnetic field was initialized to negative field, H = -3000 Oe, the exchange-bias increased at negative currents (electrons from FM to AFM) and then saturated. At positive currents (electrons from AFM to FM)), they found no systematic dependence of the exchange-bias on current. When the magnetic field was initialized to positive field, H = +3000 Oe, there was no sizable variation of the exchange-bias with current.

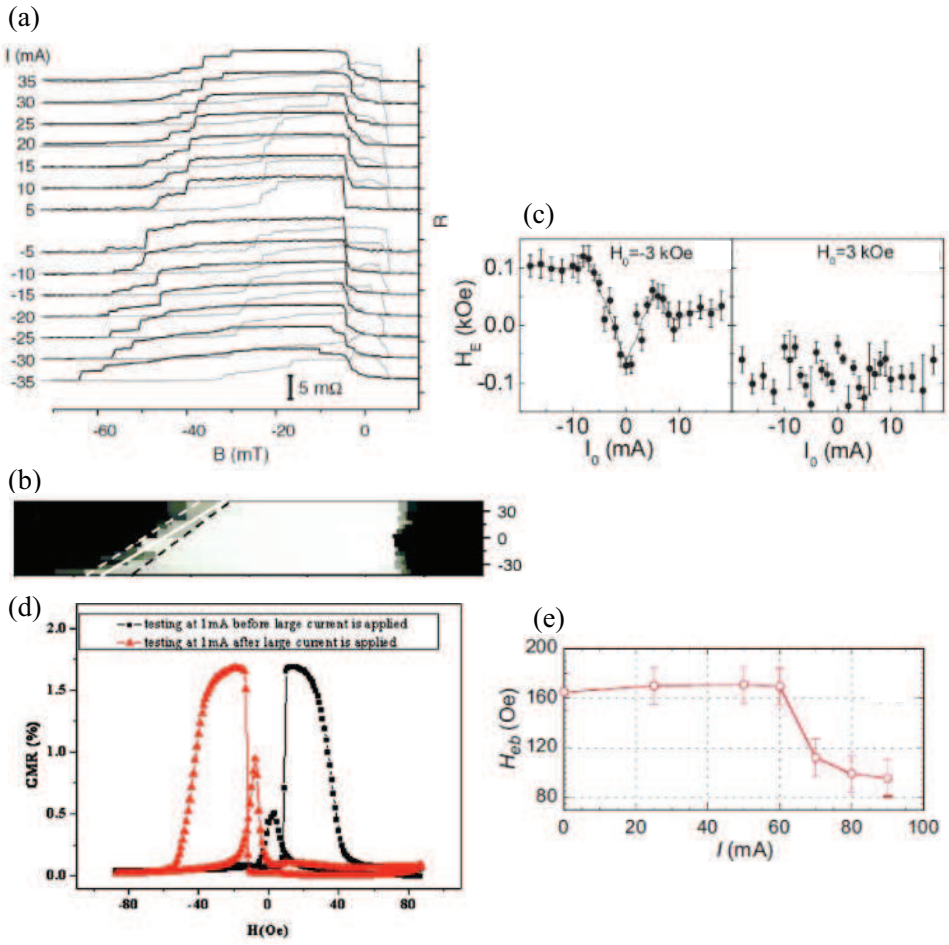


Figure 4.3: Summary of previous experiments to probe spin-torque effects in antiferromagnets. (a) Resistance as a function of magnetic field at different currents, for FeMn/CoFe bilayers in a point-contact geometry (Figure from Reference [13]). (b) Grey scale plot of the data in (a) (Figure from Reference [13]). (c) Exchange-bias as a function of current for two different initialized field values, for FeMn/Py bilayers in a nanopillar geometry (Figure from Reference [14]. (d) GMR versus field scan before and after a current is applied for FeMn/Py multilayers (Figure from Reference [15]). (e) H_{EB} as a function of current for NiCo0/CoFe multilayers (Figure from Reference [16]).

In [16], Dai et al. studied NiCoO / CoFe bilayers. In their device geometry, the CoFe layer (3 nm) was pinned by NiCoO (40 nm) and a second CoFe layer (4.5 nm) was unpinned and separated by a 3.8 nm copper spacer. They studied mm^2 multilayers and applied AC-currents in the plane (CIP) of the sample. Their results are shown in Figure 4.3(d).

In [15], Tang et al. studied FeMn / Py bilayers. In their device geometry, the Py layer (10 nm) was pinned by FeMn (15 nm) and a second Py layer (10 nm) was unpinned and separated by a 4 nm copper spacer. They studied mm^2 multilayers and applied currents in the plane (CIP) of the sample. Their results are shown in Figure 4.3(e).

4.2.3 Putting Our Experiments in Perspective

All the above experiments to date have studied the current-dependence only in the limit of large magnetic fields, near the *switching* threshold for the ferromagnet. In order to study the current dependence of the exchange-bias more directly, over a wide range of currents and magnetic fields, we have conducted *dynamical* spin-torque-driven ferromagnetic resonance (ST-FMR) measurements on antiferromagnet/ferromagnet bilayers, which allow a direct measurement of the magnitude of the exchange bias and its current dependence. We studied IrMn / Py layers in a naopillar geometry. In our device geometry, the Py layer (6 nm) is pinned by IrMn (6 nm or 9 nm) and a second Py layer (40 nm) is unpinned and separated by a 10 nm copper spacer. We will discuss our device geometry in detail in the next section.

4.3 Design & Structure of Devices

We have designed and fabricated magnetic multilayer devices with a nanopillar geometry, in which the magnetic free layer is 6 nanometers (nm) of Permalloy (Py; $Ni_{81}Fe_{19}$) exchange-biased to an antiferromagnet, IrMn (6 nm or 9 nm) (Figure 4.4). In contrast to previous experiments [18, 19] as well as the devices discussed in Chapter 3, where the *fixed layer* is typically the magnetic layer that is pinned by an antiferromagnet, we pin the *free layer* by an antiferromagnet in order to directly study the dynamics of an exchange-biased nanomagnet. In our devices, the fixed layer is a semi-extended film of Py (40 nm) (Figure 4.4) and it is "fixed" by virtue of its magnetization always being fixed along the direction of an external magnetic field due to its small coercivity. We make the fixed layer extended to reduce dipolar coupling between the magnetic layers and also to minimize any dynamics in the fixed layer. The complete layer structure is (with thicknesses in nm): 4 Py/80 Cu/40 Py/10 Cu/6 Py/(6, 9) IrMn/20 Cu/30 Pt.

We fabricated and measured devices with two different thicknesses of the IrMn antiferromagnet (6 nm and 9 nm) for comparison. We chose the free layer (Py) to be the same thickness of 6 nm for both antiferromagnet thicknesses. We would like to point out that this free layer is a little thicker (6 nm) than the free layer discussed previously (4 nm) in Chapter 3 (Figure 3.5). We chose it to be thicker for this experiment in order to avoid a large surface contribution to the damping from the antiferromagnet. We made the ferromagnet thick enough so that the surface damping would not be so dominant that we couldn't observe any resonance. However, we did not make it too thick in order to avoid precluding any dynamics in this layer.

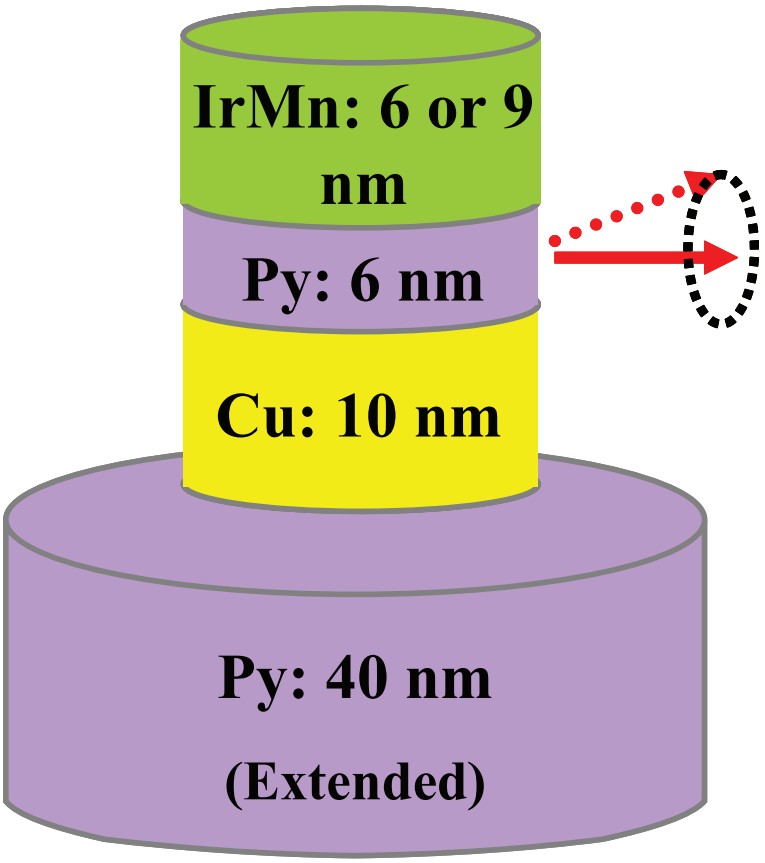


Figure 4.4: Layer structure of the pinned-free-layer nanopillar spin-valve devices that we studied. The free layer, Py (6 nm) is exchange-biased by an antiferromagnet, IrMn (6 or 9 nm), while the fixed layer (Py, 40 nm) is semi-extended.

We chose the thicknesses of the antiferromagnet after conducting SQUID measurements to determine the optimal parameters for exchange-bias. In Figure 4.5, we show SQUID results for a control sample: an unpinned Py film (Figure 4.5(a)) as well as a Py film pinned to 3 different antiferromagnet thicknesses: 3 nm (Figure 4.5(b)), 6 nm (Figure 4.5(c)) and 9 nm (Figure 4.5(d)). For the unpinned Py film (Figure 4.5(a)), the hysteresis loop is centered about zero magnetic field and has no finite width, indicating the lack of exchange-bias and anisotropy, as expected. For the Py film pinned by 3 nm (Figure 4.5(b)), we see that the loop is centered about zero magnetic field, indicating no substantial

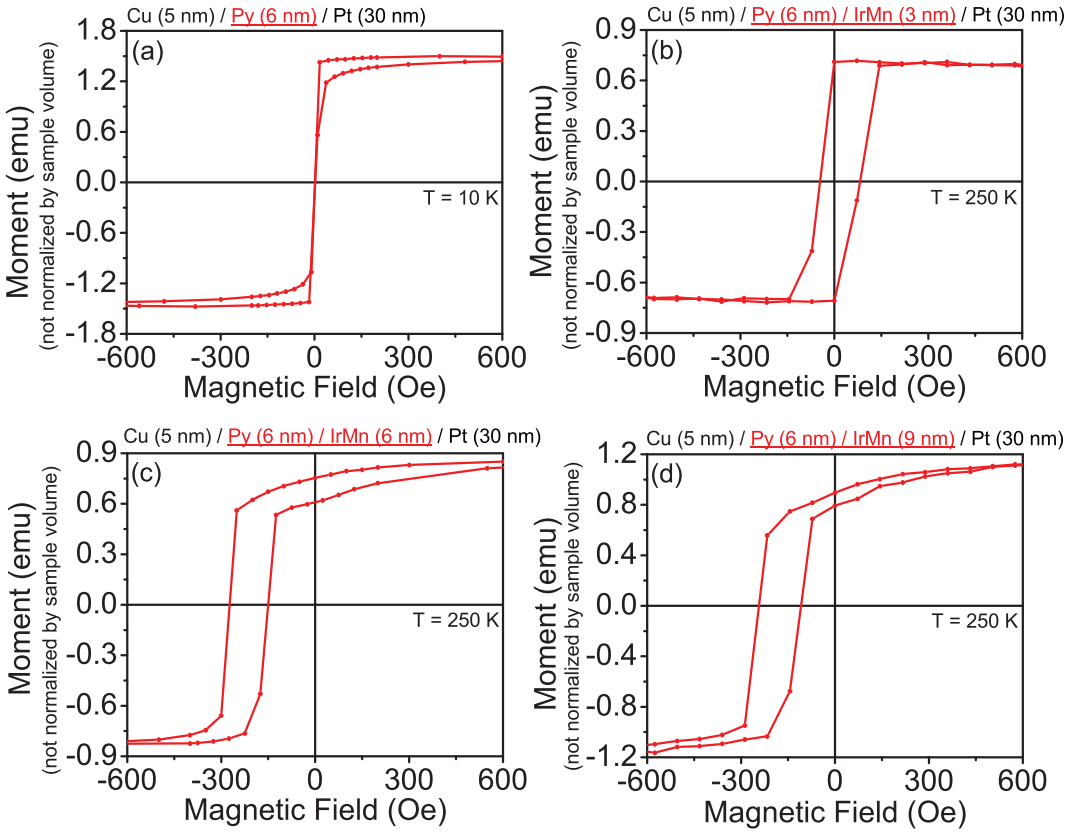


Figure 4.5: SQUID data of the magnetic moment as a function of the applied magnetic field for (a) an unpinned Py layer (6 nm thick)
and a pinned Py layer (6 nm thick) exchange-biased by antiferromagnet (IrMn) of different thicknesses (b) 3 nm, (c) 6 nm and (d) 9 nm.

exchange-bias. However, the loop has a finite width indicating an enhanced coercivity. This is not unexpected, since pinning a ferromagnetic film to an antiferromagnet is known to enhance the ferromagnet coercivity. For the Py films pinned to the 6 nm and 9 nm antiferromagnet (Figures 4.5(c) and (d)), we see that the loops are offset from zero field by about $H \approx 200$ Oe and they also have a finite width, indicating that the Py film is exchange-biased with a $H_{EB} \approx 200$ Oe. We do not see any pronounced difference in the exchange-bias for the two different antiferromagnet thicknesses in Figures 4.5(c) and (d).

4.4 Fabrication of Devices

The devices are fabricated by the procedure described in Section 2.1. The layers are first deposited by sputtering in a magnetic field (300 Oe) and annealed at 220°C for 85 minutes to exchange-bias the free-layer. We use electron-beam lithography and ion-milling to pattern the antiferromagnet, the free magnetic layer and the Cu spacer layer to give a circular or elliptical cross-section. We etch only partially (about 4-5 nm) into the fixed layer to make it mostly extended. In order to minimize any artifact signals arising from magnetic fluctuations in the contacts, we incorporate an additional etch step (not discussed in Section 2.1) to pattern the fixed layer into an 18×18 μm^2 square (Figure 4.6), leaving the contacts free of magnetic material. This patterned area of the fixed layer is still almost 10^4 times larger than the cross-sectional area of the free layer, thereby allowing it to still be semi-extended and unpatterned relative to the free layer. We use photo-lithography to pattern bottom leads and to make top contacts. We have measured 6 devices in detail: 3 devices with a 6 nm IrMn thickness and 3 devices with a 9 nm IrMn thickness. In this chapter, we will discuss data for a 80 nm^2 diameter circular device (Figure 4.7(a), inset) with 9 nm IrMn thickness, for which we observed the most pronounced effects in the ST-FMR measurements.

4.5 DC-Characterization

Figure 4.7(a) shows a typical differential resistance (dV/dI) as a function of the magnetic field at room temperature. As the magnetic field is swept along the direction of the exchange-bias (”0 degrees”), we observe hysteretic switching of the magnetic layers between parallel and anti-parallel alignment with a resis-

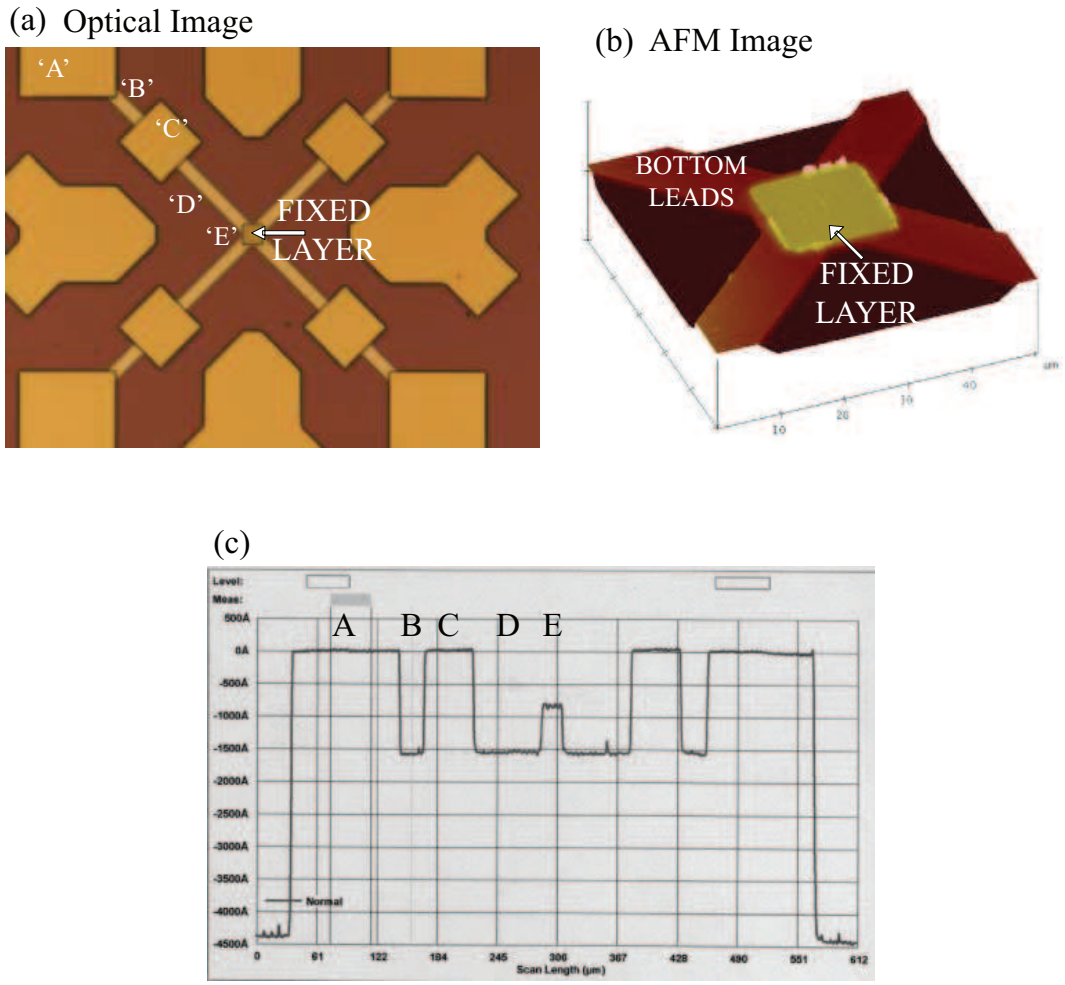


Figure 4.6: Optical and AFM images of the semi-extended fixed layer. (a) Optical image of the bottom leads and the fixed layer after photolithography. We do the etch in two steps: in the first step, we etch till the fixed layer. In the second step, we protect a square of $18\mu m^2$ in the center (″E″) and etch the bottom leads (″B″ and ″D″) all the way to the Cu bottom electrode. (b) AFM image of a surface plot showing the $18\mu m^2$ fixed layer and the deeper bottom leads. (c) Profilometry scan of the fixed layer height relative to the bottom leads. We scan from the top pads (″A″) across the bottom lead (″B″), the bottom pad (″C″), bottom lead (″D″) and the fixed layer (″E″).

tance change, $\Delta R \approx 0.1\Omega$. The loop on the left corresponds to the switching of the exchange-biased free layer: the non-zero offset is due to the exchange-bias field ($H_{EB} \approx 100$ Oe) from the antiferromagnet and the width of the loop is very small due to the negligible shape anisotropy of the circular device. The loop on the right, close to zero field, corresponds to the switching of the semi-extended fixed layer which has a very small coercive field (< 10 Oe) (this small coercive field might be due to non-zero dipole interactions with the pinned free layer).

Note that the H_{EB} of the patterned pinned free layer is smaller than the H_{EB} of the pinned free layer thin film measured in the SQUID (Figure 4.5(d)). This may be because the antiferromagnet pins a smaller surface-area of the ferromagnet in the patterned case than in the thin-film case, leading to a smaller H_{EB}. Also note that the H_{EB} is smaller for these devices than the H_{EB} measured in previous experiments (Figure 3.6(b)), because the antiferromagnet is grown on *top* of the ferromagnet in the current experiment whereas it was grown at the *bottom* of the ferromagnet in previous experiments. Our SQUID measurements for both kinds of samples: FM/AFM and AFM/FM layers are also consistent with this difference in exchange-bias.

Figure 4.7(b) shows the differential resistance (dV/dI) as a function of the applied field angle, θ_H at H = 75 Oe, less than the H_{EB}. When the magnetic field is applied along 0° (i.e. the exchange-bias direction), both magnetic layers are parallel (low resistance). Since the coercivity of the unpatterned fixed layer is very small, as the magnetic field is rotated away from 0°, the magnetization of the fixed layer follows the field direction while the magnetization of the free layer remains pinned approximately along the exchange-bias direction. As a result, the angle between the layers changes gradually from parallel (at θ_H = 0

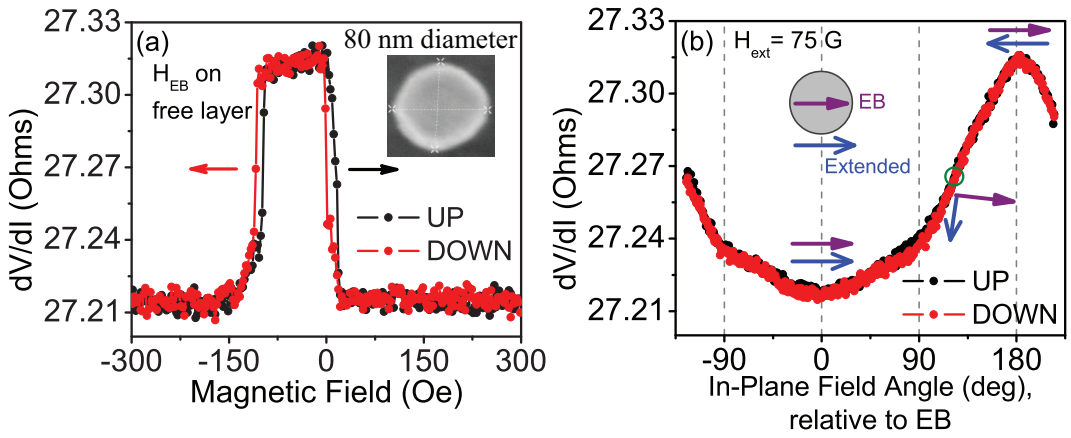


Figure 4.7: (a) Differential resistance as a function of magnetic field applied along the direction of the exchange-bias. Inset: SEM of circular cross-section of 80 nm diameter device. (b) Differential resistance as a function of magnetic field angle. "0 degrees" corresponds to the exchange-bias direction.

degrees) to anti-parallel orientation (at $\theta_H = 180$ degrees) as θ_H is varied. (Note that the slope of the resistance between $\theta_H = 0°$ and $\theta_H = 90°$ is smaller than the slope between $\theta_H = 90°$ and $\theta_H = 180°$. This is due to the fact that the pinned free layer also moves by a few degrees as the external field angle is varied, but it moves by a much lesser amount once the magnetic field crosses 90°. Therefore, the resistance increases much faster between $90 - 180°$ than it does between $0 - 90°$. At much smaller H, the resistance slope is almost always the same between $0 - 90°$ and $90 - 180°$, as we would expect, since the pinned free layer doesn't move at all). The advantage of our device design is that it allows for an easy control of the relative alignment between the layers simply by rotating the magnetic field.

4.6 ST-FMR Measurements

We have conducted ST-FMR measurements (Section 2.2.3) on these devices and these will be our main focus. In the ST-FMR technique [20, 21], a radio-frequency current (I_{RF}) is applied across the device to excite magnetic precession. The precession of the magnetic moments of one or both of the layers causes changes in the resistance of the magnetic multilayer. The amplitude of the resonant motion is detected from the changing resistance of the sample by measuring the dc-voltage corresponding to the mixing of the I_{RF} and the changing resistance (Equation 2.28).

A typical ST-FMR spectrum of the mixing voltage (V_{mix}) as a function of the frequency for our FM/AFM bilayer devices is shown in Figure 4.8(a). The spectrum has a non-zero offset due to the non-linear V-I behavior of the device. We observe a positive peak close to 3 GHz (Peak-1) and a closely spaced negative peak close to 4 GHz (Peak-2). We have confirmed that the positive and negative peaks correspond to two distinct modes since they move independently with field magnitude and field angle (Figure 4.8(b)). Figure 4.8(b) shows the spectra at H =100 Oe at different θ_H. At $\theta_H = 129$ degrees, we observe a spectrum similar to Figure 4.8(a), but as we increase θ_H, the positive and negative peaks distinctly separate. Based on this, we have analyzed all our spectral data by fitting the positive and negative peaks to a sum of two Lorentzian peaks (Equation 4.1) with 7 adjustable parameters: the offset (u) as well as the frequencies (f, g), linewidths (w, z) and amplitude (a, c) of the 2 peaks.

$$V_{mix} = u + \frac{a}{(1 + (x - f)/w)^2} + \frac{c}{(1 + (x - g)/z)^2} \tag{4.1}$$

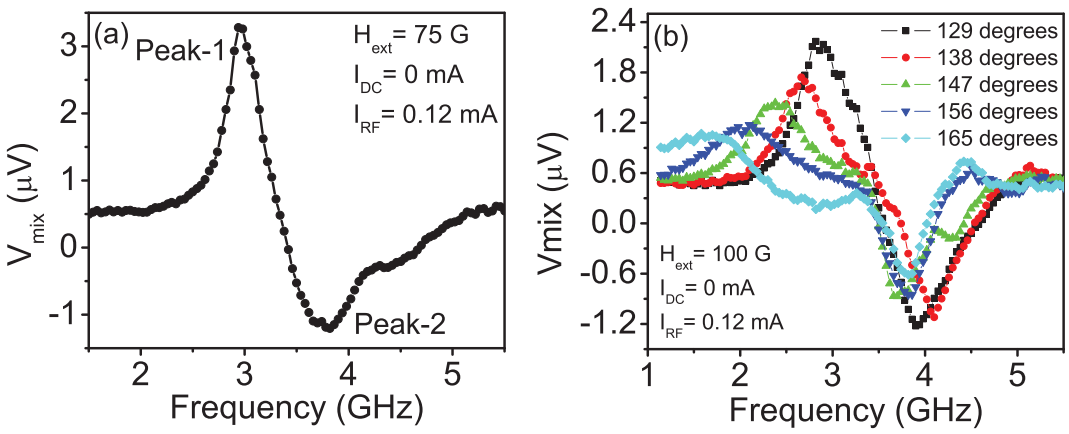


Figure 4.8: (a) Typical ST-FMR spectrum for the FM/AFM bilayer device at H = 75 Oe applied at $\theta_H = 127°$ relative to the exchange-bias (close to where the angle between the layers is close to 90°); I_{DC} = 0 mA; I_{RF} = 0.12 mA. (b) ST-FMR spectra at H = 100 Oe applied at different field angles θ_H, where we can see the two peaks separating.

4.7 Analysis as a Function of Magnetic Field Angle

In order to determine which peak in the spectrum corresponds to the pinned free layer excitation mode, we analyze the frequency of the positive and negative peaks as a function of the applied field angle (Figure 4.9(a)) when only a small RF-current (I_{RF} = 0.12 mA, I_{DC} = 0 mA) is applied. For a mode associated with a free layer excitation, we would expect the frequency to decrease steadily as the applied field angle is increased (cartoon in Figure 4.9(b)). This is for the following reason: at small field angles, the effective field on the free layer ($\vec{H}_{eff}$), due to the sum of the exchange-bias field ($\vec{H}_{EB}$) and the external field ($\vec{H}_{applied}$) is large since both these field vectors point in the same direction. Hence the frequency at small field angles would be high. As we rotate the external field away from the exchange-bias direction, we would expect the effective field on the free layer to decrease steadily since the exchange-bias field and the external field point in opposite directions, leading to a decrease in frequency. On the

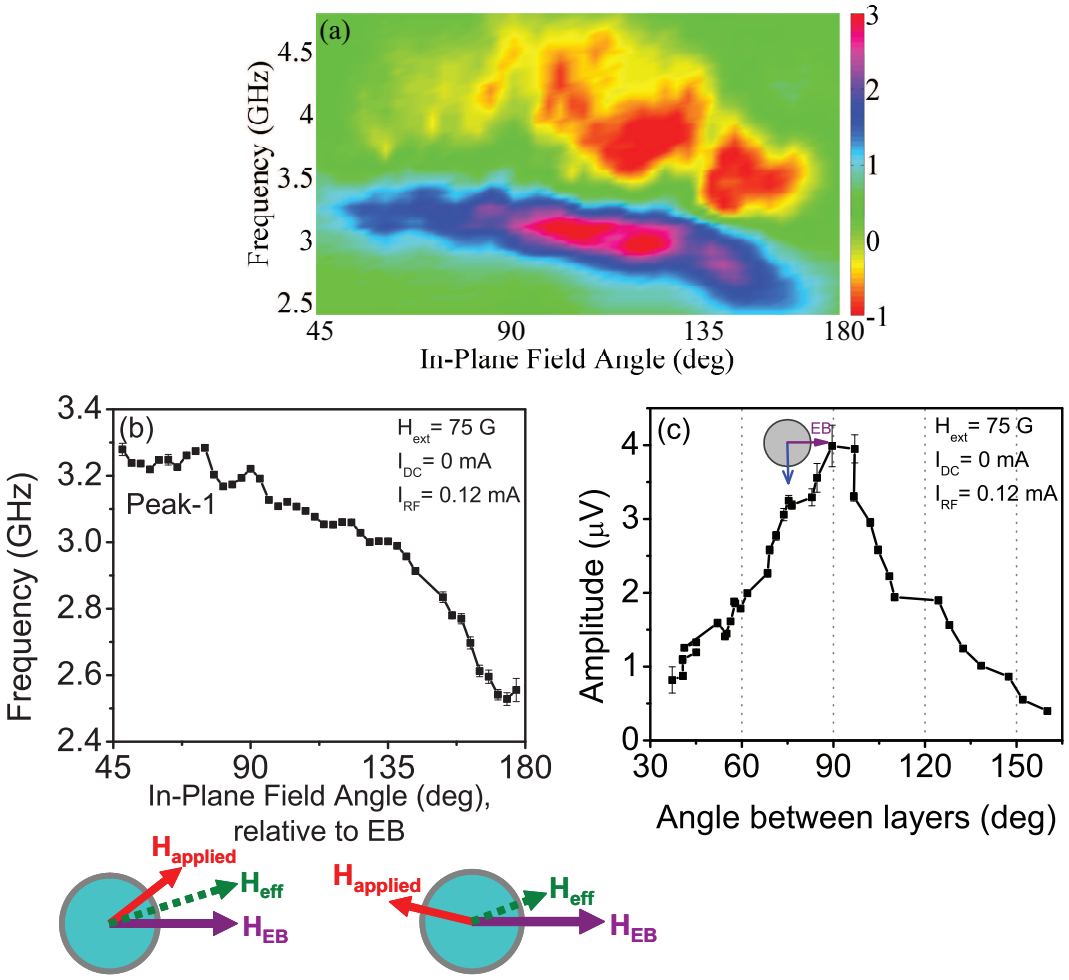


Figure 4.9: Analysis of the ST-FMR spectra for the FM/AFM pinned-free-layer device as a function of θ_H, to identify the pinned-free-layer mode. (a) 3-D color plot of the V_{mix} frequency spectrum as a function of θ_H at H = 75 Oe, I_{DC} = 0 mA and I_{RF} = 0.12 mA. (b) Frequency versus θ_H of peak-1 at H = 75 Oe, I_{DC} = 0 mA and I_{RF} = 0.12 mA. Cartoon below (b) shows the field vector, $\vec{H}_{eff}$, which is the vector sum of $\vec{H}_{external}$ and $\vec{H}_{EB}$. (c) Amplitude of the V_{mix} signal for peak-1 as a function of the angle between the magnetic layers at H = 75 Oe, I_{DC} = 0 mA and I_{RF} = 0.12 mA.

other hand, we would expect to see no dependence on the field angle for an extended fixed layer mode. This is because the extended fixed layer is isotropic and so we would expect it to have the same frequency at all field angles. In Figure 4.9(b), we find that the frequency of the positive peak (Peak-1) decreases steadily as the applied field angle is increased, indicating that this mode corresponds to the pinned free layer excitation. On the other hand, the frequency of the negative peak (Peak-2) does not have a clear dependence on the field angle (Figure 4.9(a)). This might be a mode corresponding to excitations in the extended fixed layer or some form of dynamical coupling between the fixed and free layer oscillations.

We also point out that the amplitude of the peak in the ST-FMR spectrum is proportional to the spin-transfer torque, which is proportional to $\sin\theta$ (θ is the angle between the magnetic layers). So we would expect to see a maximum torque when θ is 90°. In Figure 4.9(c), we observe that the maximum amplitude of the peak indeed occurs at a field angle where the relative angle between the layers is close to 90°.

4.8 Analysis as a Function of I_{DC}

Having identified Peak-1 to correspond to the pinned free layer excitation, we now discuss its current dependence. In order to do so, we rotated the applied field to a few different angles so that we could change the relative alignment between the layers. At each angle, we applied a DC current in addition to the RF-current (I_{RF} = 0.12 mA) and took ST-FMR data at different field magnitudes. In this section, we will focus on the field angle where the angle between the

layers is close to 90° (i.e. when the field angle is 110° relative to the exchange-bias), since we observe the largest amplitude of the ST-FMR signals at this field angle.

Figure 4.10(a) shows a color plot of the mixing voltage as a function of the frequency and I_{DC} and Figure 4.10(b) shows the spectra at a few different currents between $I_{DC} = -3$mA and $I_{DC} = +3$mA. We find that the frequency increases steadily as I_{DC} is swept from negative to positive currents (Figure 4.10(c)) for all applied magnetic fields (H). The frequency of the magnetization precession is proportional to the effective field, H_{eff}, on the ferromagnet. In the case of our circular, exchange-biased free layer sample, the effective field should depend on the applied magnetic field (H), the exchange-bias field (H_{EB}) and the out-of-plane demagnetization field, $4\pi M_{eff}$ (Equation 4.2).

$$\omega^2 = \gamma^2 \left[H\cos(\theta_H - \beta) + H_{EB}\cos\beta\right]\left[H\cos(\theta_H - \beta) + H_{EB}\cos\beta + 4\pi M_{eff}\right] \quad (4.2)$$

In the above equation, the only possible current-dependent parameters are the out-of-plane demagnetization field, $4\pi M_{eff}$ and the exchange-bias field (H_{EB}). The demagnetization field might change with current due to Joule heating of the magnetic layer. For the current range that we have conducted all our measurements in (-3 to +3 mA), we estimate from Equation 3.14 that the effective temperature of the magnetic layer can increase by ~5-10K at room temperature. The higher effective temperature can reduce the demagnetization field and therefore change the frequency. However, our previous temperature-dependence SQUID measurements have shown that the change in demagnetization field with temperature is not large enough to cause the large changes in frequency that we observe as a function of current. Therefore, we conclude that the most likely frequency dependence of the current is due to the current-dependence of the exchange-bias.

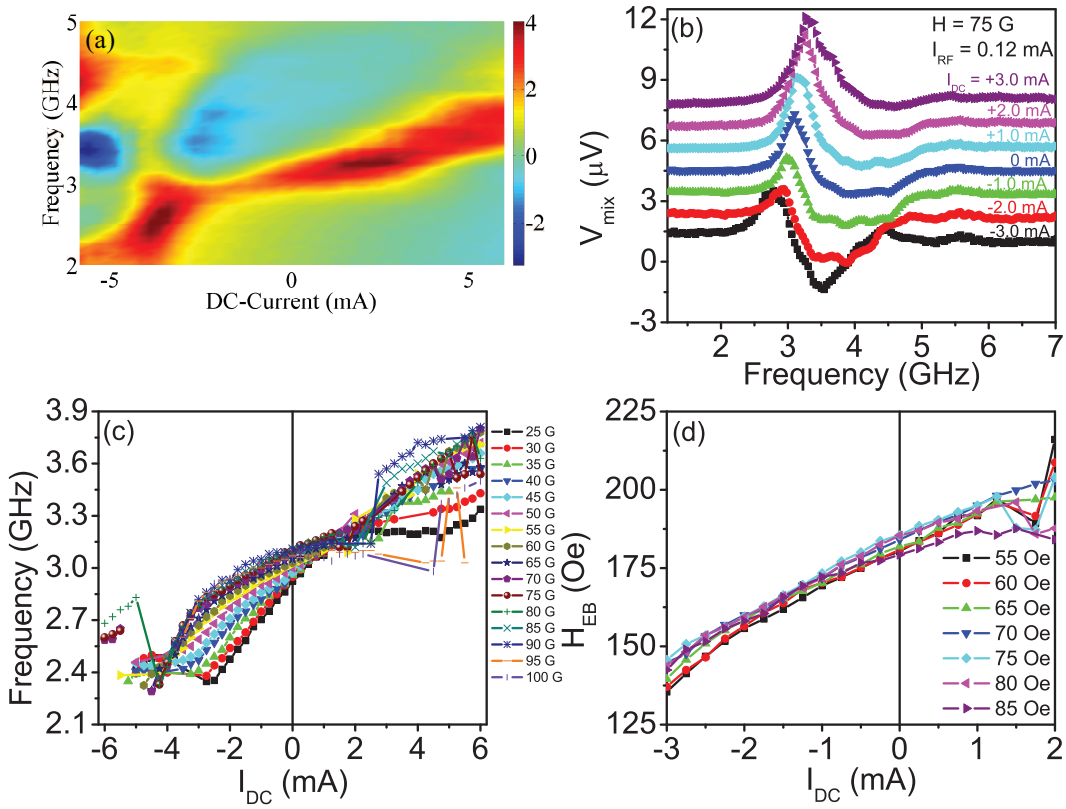


Figure 4.10: Analysis of the ST-FMR spectra for the FM/AFM pinned-free-layer device as a function of I_{DC}. (a) 3-D color plot of the V_{mix} frequency spectrum as a function of I_{DC} at I_{RF} = 0.12mA, H = 75 Oe, applied along θ_H = 110° relative to the exchange-bias (close to where the angle between the layers is 90°). Red is positive mixing voltage, blue is negative mixing voltage. (b) V_{mix} spectra at different I_{DC}. (c) Frequency versus I_{DC} for different field magnitudes (H = 25 – 100 Oe in steps of 5 Oe) applied along θ_H = 110° relative to the exchange-bias (close to where the angle between the layers is 90°). (d) H_{EB} as a function of I_{DC}, calculated from the precession frequency (Equation 4.2).

It should also be pointed out that as discussed in Chapter 3, for I_{DC} above the critical current for exciting dynamics as well as for large-angle dynamics, the amplitude of the precession increases with applied I_{DC}, which can lead to frequency variations with I_{DC}. However, in the present case, we see the large frequency variation with I_{DC} even *below* the critical current and we are also in the small-angle precession regime (precession angle is only few tens of degrees,

as we will discuss later), so that applying higher I_{DC} cannot lead to significantly high enough amplitudes to change the frequency by the large amount that we see in Figure 4.10(c). Consequently, just the variation in precession angle due to I_{DC} cannot independently explain the large variation in frequency and we conclude that the exchange-bias must have some current-dependence. We would also like to point out that the frequency changes with current cannot be explained by Joule heating, since the observed response to positive and negative currents is opposite.

From the frequency variation with current, we have calculated from Equation 4.2 the corresponding exchange-bias (H_{EB}) variation with current (Figure 4.10(d)). We see that the calculated H_{EB} for all magnetic fields changes from ≈140 Oe at $I_{DC} = -3$ mA to ≈200 Oe at $I_{DC} = +2$ mA. This corresponds to a change in H_{EB} per unit current density, $\Delta H_{EB}/\Delta J_{DC} \approx 6 \times 10^4$ Oe.nm^2/mA. We also find that above H =55 Oe, all the curves for the different applied magnetic fields collapse on the same line (Figure 4.10(d)). We would like to note that the calculated H_{EB} from the Kittel frequency at $I_{DC} = 0$ is about 180 Oe, which is a little larger than the H_{EB} measured from the dV/dI (≈100 Oe) in Figure 4.7(a).

In Figures 4.10(b)-(d), we show only the current-range between $I_{DC} = -3$ mA to $I_{DC} = +2$ mA. This is because, at higher I_{DC}, we excite vortices in the circular free layer. This can be seen by the large change in amplitude at high I_{DC} in Figure 4.10(a) and Figures 4.11(a)-(b), as well as from intermediate resistance states in the field sweeps at constant current.

According to our current convention, positive current corresponds to electrons flowing from the free layer to the fixed layer, i.e from the antiferromagnet to the free-layer ferromagnet and negative current corresponds to electrons

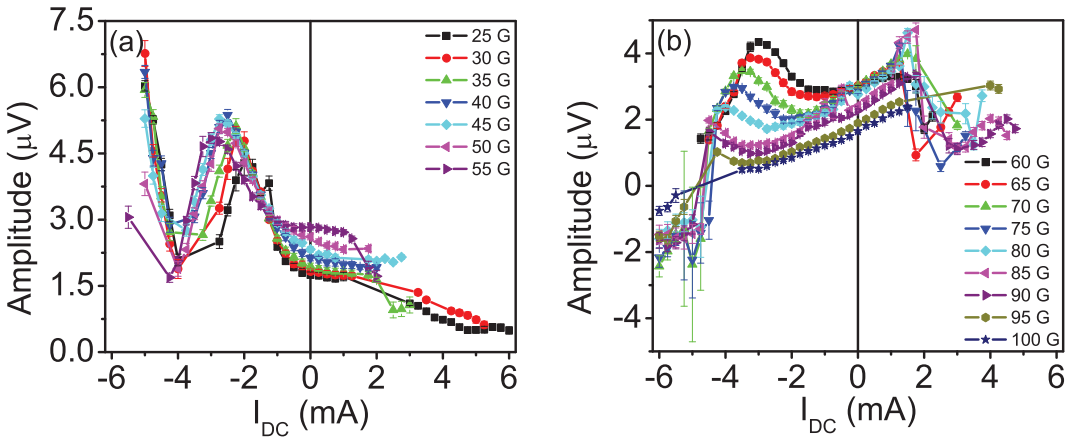


Figure 4.11: Amplitude of the ST-FMR spectral peaks as a function of I_{DC} at (a) small H and (b) large H, applied along $\theta_H = 110°$ relative to the exchange-bias (close to where the angle between the layers is 90°).

from the fixed layer to the free layer, i.e. from the ferromagnet to the antiferromagnet. Based on this, our results suggest that electrons from the antiferromagnet to the ferromagnet (positive current) enhance the exchange-bias and electrons from the ferromagnet to the antiferromagnet (negative current) decrease the exchange-bias.

4.9 Effective Damping

We have also calculated the effective damping, α from the linewidth of the ST-FMR peaks (Figure 4.12). We have found that at $I_{DC} = 0$ mA, the effective damping is about 0.025 for most of the magnetic fields (Figure 4.12). We expect to observe higher effective damping in an exchange-biased nanomagnet due to the "slow relaxer" mechanism due to thermal excitation of antiferromagnetic grains [22]. Fuchs et al. have measured damping values of 0.010 ± 0.002 in an unpinned Py nanomagnet [23]. The damping values for an exchange-biased thin film have

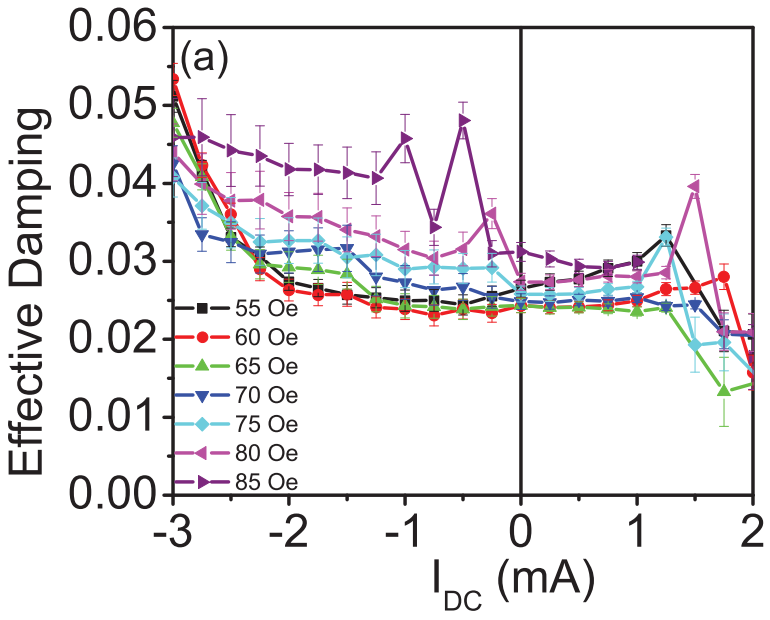


Figure 4.12: Effective damping of the FM/AFM pinned-free-layer device as a function of I_{DC} at fields applied along $\theta_H = 110°$ relative to the exchange-bias (close to where the angle between the layers is 90°).

been reported to be between 0.015 – 0.02 [24, 25, 26, 27]. We observe damping values that are slightly higher than those observed in extended films. This may be because the antiferromagnetic grains in a nanomagnet have greater freedom to undergo irreversible processes since they are not held in place by an extended film.

4.10 Dependence on I_{RF}

We also briefly studied the ST-FMR spectra at different I_{RF}. As expected, the amplitude of precession increases quadratically with I_{RF} (Figure 4.13(a)). We conducted all the above ST-FMR measurements and analysis at $I_{RF} = 0.12$ mA, which is small enough that we are not in the non-linear regime of I_{RF}. In Figure

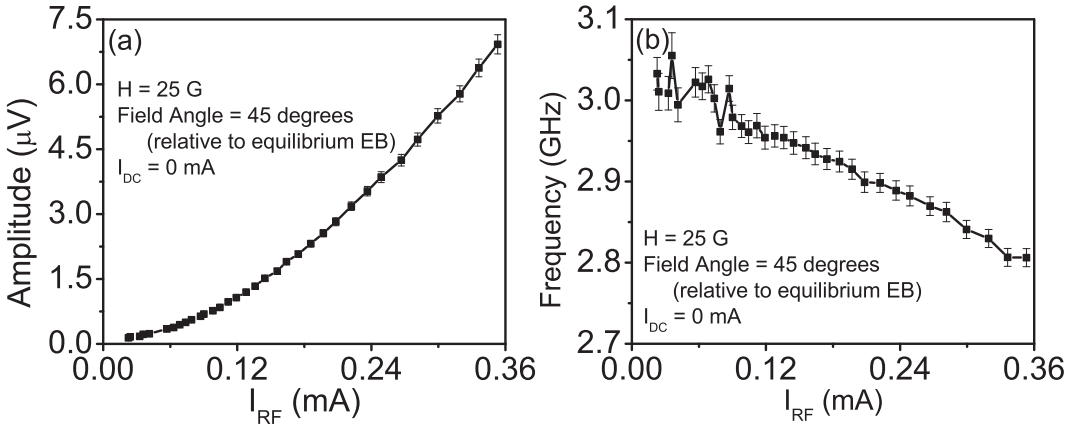


Figure 4.13: Analysis of the ST-FMR (a) amplitude and (b) frequency as a function of I_{RF} at $H = 25$ Oe applied along $\theta_H = 90°$ relative to the exchange-bias direction.

4.13(b), we plot the frequency as a function of different I_{RF} and find that it decreases with increasing I_{RF}. This is not unexpected, since increasing I_{RF} increases the precession amplitude slightly.

We have estimated the precession angle for $I_{RF} = 0.12$ mA from the V_{mix} magnitude. For a complete switching event (precession amplitude = 180°) (ΔR = 0.1Ω) and an $I_{RF} = 0.12$ mA, we would expect the V_{mix} to be about 10 μV. In Figure 4.13(a), V_{mix} is of the order of 1 μV, which amounts to a $\Delta R \approx 0.01\Omega$, which is about 1/10th of the amplitude of a complete switching event, indicating that the precession amplitude < 20°.

4.11 Variations among different samples

Thicker Antiferromagnet Devices (9 nm IrMn): For all the 3 thicker antiferromagnet devices (9 nm) studied in detail, the frequency decreases as the magnetic field is rotated away from the exchange-bias direction, indicating that we

are exciting the pinned free layer mode in all the samples. The peak shape at I_{DC} =0 mA also looks consistently similar across all the devices (Figure 4.8(a)). For all 3 samples, we observe strong variations in the frequency as a function of current: the frequency decreases with negative I_{DC} and increases with positive I_{DC} when the relative angle between the layers is close to 90°, indicating that the exchange-bias is current-dependent.

Thinner Antiferromagnet Devices (6 nm IrMn): In Figure 4.14, we summarize the data for one of the thinner antiferromagnet (6 nm) samples. The differential resistance (dV/dI) as a function of H (Figure 4.14(a)) and θ_H (Figure 4.14(b)) look similar to the one for the thicker antiferromagnet sample in Figure 4.7. The peak shape (Figure 4.14(c)) also looks similar to that for the thicker antiferromagnet sample (Figure 4.8(a)). As a function of the magnetic field angle, the frequency of the positive peak decreases indicating that we are exciting the pinned free layer mode (Figure 4.14(d)). As a function of I_{DC} (Figure 4.14(e)-(f)), there is a variation in the frequency but it is not as strong as for the thicker antiferromagnet sample (Figure 4.10).

We are not sure what the discrepancy in the current-dependence of the frequency between the thicker and thinner antiferromagnet samples might be due to. Theories have predicted that the spin-torque on an antiferromagnet acts on the bulk of the antiferromagnet, as opposed to the surface as in the case of a ferromagnet [8]. Since the spin-torque on the antiferromagnet is predicted to be a bulk effect, it is possible that the spin-torque may act differently on the different thicknesses of antiferromagnet, leading to different consequences for the current-dependence of the exchange-bias.

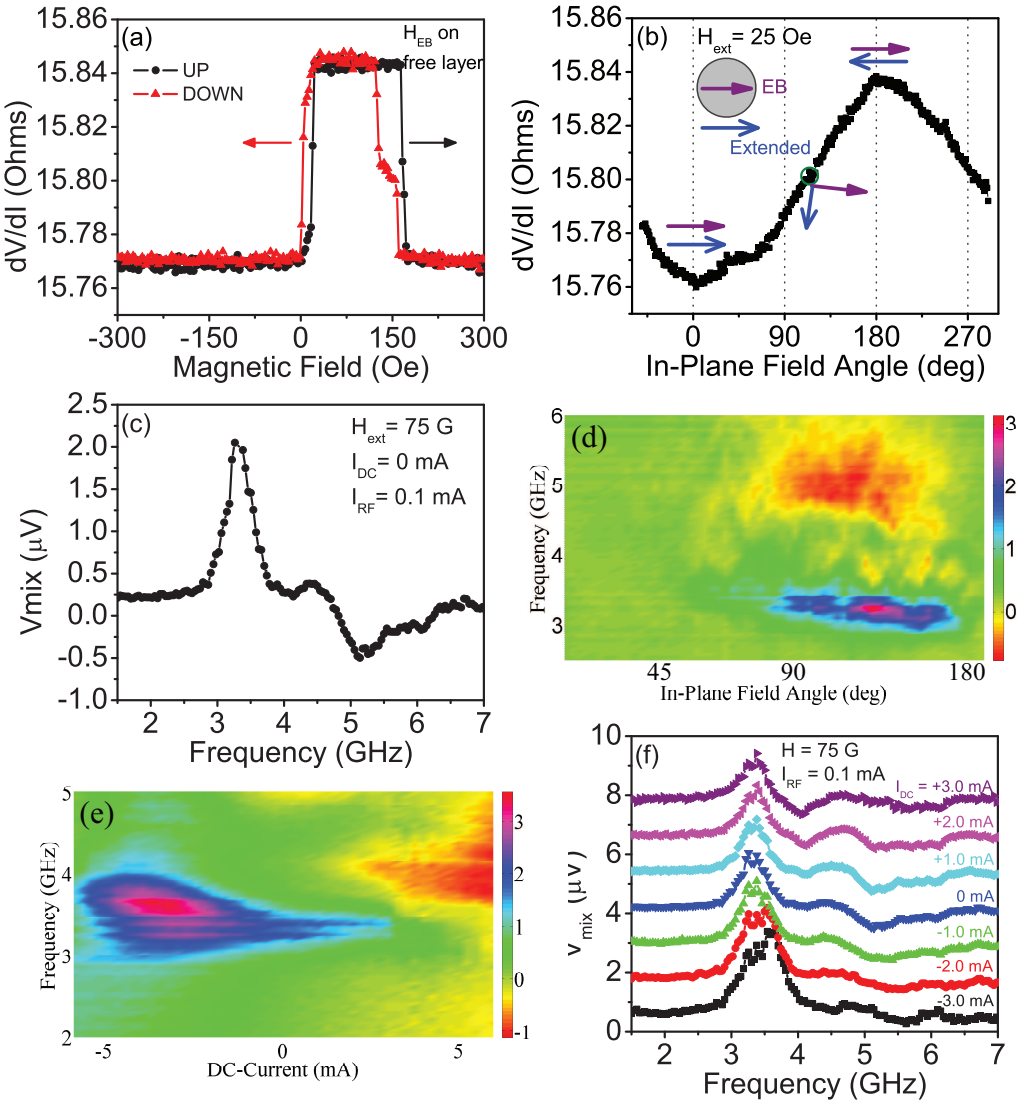


Figure 4.14: Data for a thinner antiferromagnet (6 nm) device. (a) Differential resistance as a function of magnetic field applied along the direction of the exchange-bias. (b) Differential resistance as a function of magnetic field angle. ″0 degrees″ corresponds to the exchange-bias direction. (c) Typical ST-FMR spectrum for the FM/thinner AFM (6 nm) bilayer device at H = 75 Oe applied along θ_H = 110° relative to the exchange-bias (close to where the angle between the layers is about 90°). (d) 3-D color plot of the V_{mix} frequency spectrum as a function of θ_H at H=75 Oe, I_{DC} =0 mA and I_{RF} =0.1 mA. (e) 3-D color plot of the V_{mix} frequency spectrum as a function of I_{DC} at H=75 Oe, I_{RF} = 0.1 mA, applied along θ_H = 110° relative to the exchange-bias (close to where the angle between the layers is about 90°). (f) V_{mix} spectra at different I_{DC}.

4.12 Comparison to Previous Studies of Spin-Torque Effects on Exchange-Bias

We would like to compare the changes in exchange-bias that we observe to previous studies of the current-dependence of the exchange-bias. In particular, we would like to compare our results to Wei et al. [13, 17]. We show their data in Figure 4.15 for FeMn and IrMn exchange-biased samples. In their experiments, they applied very high current densities of the order of 10^8 A/cm^2 across a point-contact geometry. Their current convention is the same as ours: positive current corresponds to electrons from the free layer to the fixed layer. They found that the exchange-bias decreases for positive currents and increases for negative currents and they calculated slopes of about 0.2-0.3 Tesla/Amperes (T/A) for the FeMn samples and about 0.01 T/A for the IrMn samples [13, 17].

Comparing our device structure to their devices: our Cu spacer thickness is the same (10 nm) as theirs; their pinned layer is CoFe (3 nm) whereas our pinned layer is Py (6 nm); their antiferromagnet thicknesses (IrMn and FeMn, 8 nm) are close to the thicknesses we used (IrMn, 6 nm and 9 nm).

As we showed in Figure 4.10(d), for our samples, the exchange-bias increases at positive currents and decreases at negative currents. This is opposite to the trend observed by Wei et al. in [13, 17]. However, we would like to point out that even in [13, 17], there were differences between the current-dependence of the exchange-bias for the IrMn and FeMn antiferromagnet samples. For their samples, the current-dependence on exchange-bias for IrMn samples appears to be much weaker than for the FeMn antiferromagnet samples (Figure 4.15). We suggest that the different current-dependence of the exchange-bias between

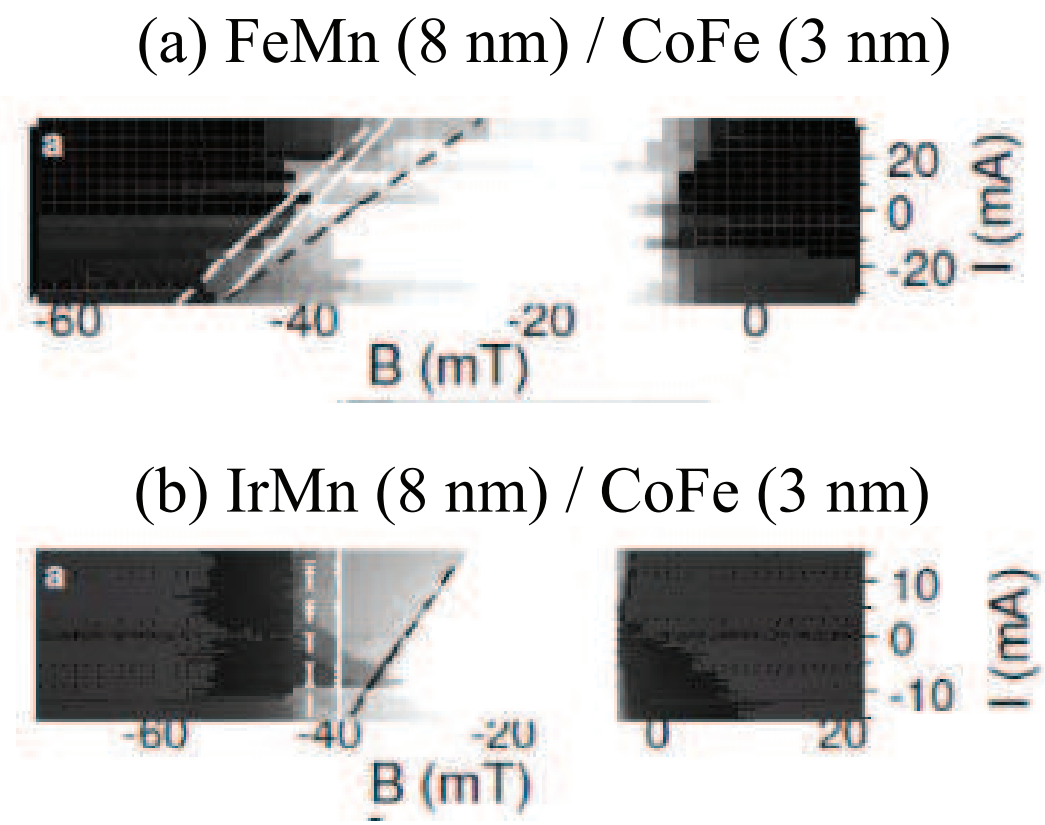


Figure 4.15: Comparison of the current-dependence of the H_{EB} for FeMn/CoFe bilayers and IrMn/CoFe bilayers (Figure from Reference [17]).

our samples and their samples might be due to different interfaces between the antiferromagnet / ferromagnet (IrMn / Py, in our case; IrMn / CoFe, in the case of Wei et al.). We have also learned from private communication with Prof. Jack Bass at Michigan State that they observed some unusual behavior in their IrMn / Py samples; their results have not been published, so we are unable to directly compare our results with theirs for the IrMn / Py bilayers.

We also tried to do some quantitative comparisons between the current-dependence of the exchange-bias for our samples and theirs. First, the current densities that we applied across our samples were of the order of 10^7 A/cm^2, while Wei et al. applied current densities of the order of 10^8 A/cm^2. From Fig-

ure 4.10(d), we estimate the change in exchange-bias per unit current for our sample to be about 1.2 T/A. This is slightly larger than the slope reported by Wei et al. for the FeMn/CoFe samples (0.2 - 0.3 T/A) and much larger than their IrMn/CoFe samples (0.01 T/A). The exchange-bias per unit current density for our sample was about 6000 T.nm^2/A, compared to about 4000 T.nm^2/A for the FeMn samples and 200 T.nm^2/A for the IrMn samples measured by Wei et al.

4.13 Conclusions

We have conducted spin-torque-driven ferromagnetic resonance (ST-FMR) measurements on magnetic nanopillar devices in which the free layer is exchange-biased by an antiferromagnet, with the motivation of exploring spin-torque effects on the exchange-bias in antiferromagnet/ferromagnet bilayers. We have found variations in the precession frequency as a function of current, indicating that the exchange-bias is current-dependent. The current-dependence of the frequency variations is stronger in devices with a thicker antiferromagnet (9 nm) than in the devices with a thinner antiferromagnet (6 nm). We have also verified that the effective damping of an exchange-biased nanomagnet is higher than for an unpinned nanomagnet.

REFERENCES

[1] Meiklejohn W.H. & Bean C.P., New magnetic anisotropy, *Phys. Rev.* **102**, 1413 LP (1956).

[2] Mauri D., Siegmann H.C., Bagus P.S., & Kay E., Simple model for thin ferromagnetic films exchange coupled to an antiferromagnetic substrate, *J. Appl. Phys.* **62**, 3047 (1987).

[3] Malozemoff A.P., Random-field model of exchange anisotropy at rough ferromagnetic-antiferromagnetic interfaces, *Phys. Rev. B* **35**, 3679 LP (1987).

[4] Malozemoff A.P., Heisenberg-to-ising crossover in a random-field model with uniaxial anisotropy, *Phys. Rev. B* **37**, 7673 LP (1988).

[5] Schulthess T.C. & Butler W.H., Consequences of spin-flop coupling in exchange biased films, *Phys. Rev. Lett.* **81**, 4516 LP (1998).

[6] Stiles M.D. & McMichael R.D., Model for exchange bias in polycrystalline ferromagnet-antiferromagnet bilayers, *Phys. Rev. B* **59**, 3722 LP (1999).

[7] Haney P., Duine R., Nez A., & MacDonald A., Current-induced torques in magnetic metals: Beyond spin-transfer, *J. Magn. Magn. Mater.* **320**, 1300 (2008).

[8] Nunez A.S., Duine R.A., Haney P., & MacDonald A.H., Theory of spin torques and giant magnetoresistance in antiferromagnetic metals, *Phys. Rev. B* **73**, 214426 (2006).

[9] Wei Z., Sharma A., Bass J., & Tsoi M., Point-contact search for antiferromagnetic giant magnetoresistance, *J. Appl. Phys.* **105**, 07D113 (2009).

[10] Haney P.M. & MacDonald A.H., Current-induced torques due to compensated antiferromagnets, *Phys. Rev. Lett.* **100**, 196801 (2008).

[11] Xu Y., Wang S., & Xia K., Spin-transfer torques in antiferromagnetic metals from first principles, *Phys. Rev. Lett.* **100**, 226602 (2008).

[12] Gomonai E.V. & Loktev V.M., Distinctive effects of a spin-polarized current on the static and dynamic properties of an antiferromagnetic conductor, *Low Temp. Phys.* **34**, 198 (2008).

[13] Wei Z., Sharma A., Nunez A.S., Haney P.M., Duine R.A., Bass J., MacDonald A.H., & Tsoi M., Changing exchange bias in spin valves with an electric current, *Phys. Rev. Lett.* **98**, 116603 (2007).

[14] Urazhdin S. & Anthony N., Effect of polarized current on the magnetic state of an antiferromagnet, *Phys. Rev. Lett.* **99**, 046602 (2007).

[15] Tang X.L., Zhang H.W., Su H., Zhong Z.Y., & Jing Y.L., Changing and reversing the exchange bias in a current-in-plane spin valve by means of an electric current, *Appl. Phys. Lett.* **91**, 122504 (2007).

[16] Dai N.V., Thuan N.C., Hong L.V., Phuc N.X., Lee Y.P., Wolf S.A., & Nam D.N.H., Impact of in-plane currents on magnetoresistance properties of an exchange-biased spin valve with an insulating antiferromagnetic layer, *Phys. Rev. B* **77**, 132406 (2008).

[17] Wei Z., Basset J., Sharma A., Bass J., & Tsoi M., Spin-transfer interactions in exchange-biased spin valves, *J. Appl. Phys.* **105**, 07D108 (2009).

[18] Krivorotov I.N., Emley N.C., Sankey J.C., Kiselev S.I., Ralph D.C., & Buhrman R.A., Time-domain measurements of nanomagnet dynamics driven by spin-transfer torques 10.1126/science.1105722, *Science* **307**, 228 (2005).

[19] Thadani K.V., Finocchio G., Li Z.P., Ozatay O., Sankey J.C., Krivorotov I.N., Cui Y.T., Buhrman R.A., & Ralph D.C., Strong linewidth variation for spin-torque nano-oscillators as a function of in-plane magnetic field angle, *Phys. Rev. B* **78**, 024409 (2008).

[20] Tulapurkar A.A., Suzuki Y., Fukushima A., Kubota H., Maehara H., Tsunekawa K., Djayaprawira D.D., Watanabe N., & Yuasa S., Spin-torque diode effect in magnetic tunnel junctions, *Nature* **438**, 339 (2005).

[21] Sankey J.C., Braganca P.M., Garcia A.G.F., Krivorotov I.N., Buhrman R.A., & Ralph D.C., Spin-transfer-driven ferromagnetic resonance of individual nanomagnets, *Phys. Rev. Lett.* **96**, 227601 (2006).

[22] McMichael R.D., Lee C.G., Stiles M.D., Serpa F.G., Chen P.J., & W. F. Egelhoff J., Exchange bias relaxation in coo-biased films, *J. Appl. Phys.* **87**, 6406 (2000).

[23] Fuchs G.D., Sankey J.C., Pribiag V.S., Qian L., Braganca P.M., Garcia A.G.F.,

Ryan E.M., Li Z.P., Ozatay O., Ralph D.C., & Buhrman R.A., Spin-torque ferromagnetic resonance measurements of damping in nanomagnets, *Appl. Phys. Lett.* **91**, 062507 (2007).

[24] Lubitz P., Rubinstein M., Krebs J.J., & Cheng S.F., Frequency and temperature dependence of ferromagnetic linewidth in exchange biased permalloy, *J. Appl. Phys.* **89**, 6901 (2001).

[25] Rezende S.M., Lucena M.A., Azevedo A., Aguiar F.M.d., Fermin J.R., & Parkin S.S.P., Exchange anisotropy and spin-wave damping in cofe/irmn bilayers, *J. Appl. Phys.* **93**, 7717 (2003).

[26] Queste S., Dubourg S., Acher O., Barholz K.U., & Mattheis R., Exchange bias anisotropy on the dynamic permeability of thin nife layers, *J. Appl. Phys.* **95**, 6873 (2004).

[27] Weber M.C., Nembach H., Hillebrands B., Carey M.J., & Fassbender J., Real-time evidence of two-magnon scattering in exchange-coupled bilayers, *J. Appl. Phys.* **99**, 08J308 (2006).

CHAPTER 5

CONCLUSIONS

In this dissertation, we have described experiments to study the microwave signals produced by spin-torque-driven magnetization dynamics in magnetic multilayer spin-valve devices with a nanopillar geometry.

Spin-transfer torque from a spin-polarized current can generate steady-state magnetic precession in magnetic multilayers, a phenomenon of technological interest for making tunable nanoscale microwave sources and resonators. For technological applications, it is desirable that the microwave signal has a frequency spectrum with a narrow linewidth at room temperature. The linewidth of DC-driven precession is determined by deviations from perfect periodicity in the precessional trajectories. Some important sources of these deviations might be amplitude and phase fluctuations, thermally-activated hopping between dynamical modes or spatial incoherence.

The motivation of the first part of our work, described in Chapter 3, was to understand the important mechanisms contributing to the linewidths with a view to optimizing the coherence of the oscillations. We studied the frequency linewidths of the precessional oscillations as a function of the in-plane magnetic field angle and temperature. We reported measurements and simulations of DC-driven precession which showed a surprisingly strong dependence on the linewidth on the in-plane angle of the applied field. We found that the most-commonly studied field orientation, in-plane and parallel to the magnetic easy axis, produces the broadest linewidths. As the field angle is rotated toward the in-plane hard axis the linewidths decrease dramatically, by more than a factor of 20 in some devices. Based on micromagnetic simulations, we identified these

variations as due to a transition from spatially incoherent to coherent precession. This work was published in [1].

We also studied the linewidths as a function of temperature at field angles where we observed the narrowest linewidths, i.e. along the in-plane hard axis. We found that our experimental linewidths could be explained by a combination of amplitude and phase fluctuations and thermally-activated hopping between different dynamical modes. At lower temperatures, the linewidths were more strongly affected by amplitude and phase fluctuations. At higher temperatures, the linewidths increased rapidly because of thermally-activated hopping between dynamical modes.

The motivation of the second part of our work, described in Chapter 4, was to investigate spin-torque effects on the exchange-bias of antiferromagnet/ferromagnet bilayers. Antiferromagnets are commonly used in magnetic sensors to pin the magnetization of a ferromagnet in a particular direction by interfacial exchange coupling. This "exchange-bias" phenomenon leads to a unidirectional anisotropy and enhanced coercivity in the ferromagnet. Theories have predicted that an electrical current crossing through an antiferromagnet/ferromagnet interface can alter this exchange-bias, and some experiments have also claimed to observe an effect on magnetic switching. However, all experiments to date have studied the current-dependence only in the limit of large magnetic fields, near the switching threshold for the ferromagnet. In order to study the current dependence of the exchange-bias more directly, over a wide range of currents and magnetic fields, we conducted spin-torque-driven ferromagnetic resonance (ST-FMR) measurements on antiferromagnet/ferromagnet bilayers.

We fabricated magnetic nanopillar devices in which the free magnetic layer is exchange-biased to an antiferromagnet, and which allow a direct measurement of the magnitude of the exchange bias and its current dependence. We observed a strong variation in the precession frequency of the pinned free layer as a function of current. Since the frequency of the magnetization precession is proportional to the effective field on the magnet, which in turn depends on the exchange-bias field, we concluded that the exchange-bias changes with current. We also verified that the effective damping of an exchange-biased nanomagnet is higher than for an unpinned nanomagnet.

REFERENCES

[1] Thadani K.V., Finocchio G., Li Z.P., Ozatay O., Sankey J.C., Krivorotov I.N., Cui Y.T., Buhrman R.A., & Ralph D.C., Strong linewidth variation for spin-torque nano-oscillators as a function of in-plane magnetic field angle, *Phys. Rev. B* **78**, 024409 (2008).